

Available online at [www.sciencedirect.com](http://www.sciencedirect.com)

# Characterization of electrically active dopant profiles with the spreading resistance probe

T. Clarysse<sup>a,\*</sup>, D. Vanhaeren<sup>a</sup>, I. Hoflijk<sup>a</sup>, W. Vandervorst<sup>a,b</sup><sup>a</sup>IMEC, Kapeldreef 75, B-3001 Leuven, Belgium<sup>b</sup>KU Leuven, Electrical Engineering Department, INSYS, Kasteelpark Arenberg 10, B-3001 Leuven, Belgium

Available online 1 February 2005

## Abstract

Since its original conception in the 1960s, the spreading resistance probe (SRP) has evolved into a reliable and quantitative tool for sub-micrometer, electrically active dopant, depth profiling in silicon. Its application limit has in recent years even been pushed down to ultra-shallow (sub-50 nm) structures. In this review, a systematic discussion is presented of all issues of importance for a high quality raw data collection and subsequent high accuracy data analysis. The main focus will be on the new developments over the last two decades. The qualification requirements to be fulfilled for 10% profile accuracy (in the absence of carrier spilling) and some of the main fields for SRP application in today's industry will be covered. Finally, a critical assessment of the technique will be made, and its future roadmap will be discussed.

© 2005 Published by Elsevier B.V.

**Keywords:** Spreading resistance probe; Active dopant distribution; Carrier depth profiling; Sheet resistance

## 1. Introduction

Originally, Mazur and Dickey have introduced the spreading resistance probe (SRP) technique in 1966 [1]. They illustrated that SRP had the intrinsic capability to extract the electrically active dopant depth profile in silicon structures with a large dynamic range ( $10^{11}$ – $10^{21}$  carriers/cm<sup>3</sup>) and a good accuracy on 50 μm deep structures. As the technique has been improved upon in subsequent years, it became widely spread for the measurement of ever-shallower (down to sub-100 nm) carrier depth profiles in silicon material. In support of the growing number of users, an ASTM standard for the technique has been published [2]. Much of the information discussed in this review, however, relates to recent issues not yet covered by this standard.

SRP is basically a comparative technique for the determination of the in-depth resistivity (and active dopant) profile of an unknown silicon structure. As such, it gives direct access to the electrically active portion (mobile electrons and holes) of the dopant profile, opposite to chemical profiling techniques, such as secondary ion mass spectrometry (SIMS), which probe the fixed dopant ions of pre-selected impurity species. In the early days, for thick structures, one could extract the unknown depth profile by direct comparison with a set of calibrated homogeneous samples, covering the resistivity range of interest, with little additional calculations. Today, as we

\* Corresponding author.

E-mail address: [trudo.clarysse@imec.be](mailto:trudo.clarysse@imec.be) (T. Clarysse).

are faced with the measurement of highly doped, shallow (sub-100 nm) and steep (1–2 nm/decade) structures, the data interpretation has become much more elaborate and much of the progress over the last two decades has consequently been achieved in the area of data calibration, interpretation and deconvolution. International projects sponsored by the European Commission, such as the Esprit project [3] on dopant profiling for sub-micrometer structures (period 1985–1990) and the BCR project [4] on the quantitative measurement of electrical junction depths, lateral out-diffusion lengths and carrier concentrations with sub-micrometer resolution (period 1991–1994), have triggered this progress.

As thinner and thinner layers needed to be profiled, also steady progress has been made in improving the experimental sample preparation and probe conditioning techniques [5]. Today, samples can be beveled at angles of a few minutes, resulting in a geometrical depth resolution of a few nanometers. This can be done with a low bevel surface roughness (less than 2 nm rms) while maintaining a sharp bevel edge. Optimally conditioned probes now typically have a contact radius smaller than 1  $\mu\text{m}$ , and consist of a large area of small micro-contacts, each of which penetrates less than 5 nm into the sample.

For any technique, the issues of short-term repeatability and long-term reproducibility are crucial to its widespread industrial application. Given the significant changes, which have taken place over the past decades, both in the data modeling and raw data collection, and the widespread usage of SRP, this has been no small challenge for SRP. A recent international round robin has highlighted this is still an issue which needs further attention [6]. Recently, a verifiably qualification procedure has been put forward to allow laboratories to improve on the present situation [7,8].

Originally SRP has been developed for silicon structures. The strength of SRP today is that it basically can profile any structure from deep epi-layers to ultra-shallow (sub-50 nm) CMOS source/drain extensions. In between these two extremes lies a world of other applications such as well structures, bipolar devices, chemical vapor deposition (CVD) or molecular beam epitaxy (MBE) grown multi-layers, sub-micrometer rapid thermal annealed (RTA) ion implantations, diffusion profiles, solid phase epitaxy (SPE) regrown layers, etc. Very recently, SRP applications have even been reported in new important and challenging areas such as metal film characterization and ion implantation in germanium.

Two of the main limitations of SRP are its probe contact size and probe separation, which are both in the micrometer range. For ultra-shallow layers (sub-100 nm), this leads among others to the need for very large correction factors (Sections 2.1 and 4.2.1) to extract the underlying resistivity information from the measured raw data. Consequently, small errors on the raw data can lead to significant distortions on the final carrier profile. New developments using much smaller (5–10 nm contact size) highly doped diamond tips (with much smaller correction factors) mounted on an AFM system are opening the way to a new generation of spreading resistance-based tools such as the scanning spreading resistance microscopy (SSRM) or NanoProfilier<sup>TM</sup> tool.

In this SRP review, we will go into more detail into all of the above-mentioned issues focusing mainly on the developments within the last two decades. For more details on the earlier SRP work, the reader is referred to the excellent reviews of Ehrstein [9] for the experimental side and Albers [10] for the analysis side. More recent reviews are available from Pawlik [11] and Mazur and Gruber [12]. First, in Section 2, we will briefly cover the basics of the technique for those unfamiliar with SRP. Next, in Section 3, we will discuss in some detail the hardware procedures for sample preparation and probe conditioning. Subsequently, in Section 4, we will systematically discuss the probe–semiconductor contact calibration and data deconvolution and the issue of repeatability and reproducibility leading to the definition of a qualified system. In Section 5, we will illustrate today's capabilities of a qualified SRP system through a variety of applications. Finally, in Section 6, we

will make a critical assessment of the present status of the technique and look forward and see where the future of SRP lies.

## 2. Basics

### 2.1. Theory

When a small bias (5 mV) is applied between a small (few square micrometer), planar, Ohmic, circular, top contact with physical radius  $a$  and a large Ohmic back-contact, on an homogeneously doped silicon sample with resistivity  $\rho$ , the measured resistance will be dominated completely by the constriction or spreading resistance near the small top contact (hence, the name of the technique) and is given by the simple formula [13,14]:

$$R_{\text{homog,spreading}} = \frac{\rho}{4a} \quad (1)$$

In practice, one uses in SRP two small top contacts positioned at a small separation  $S$ . Consequently, the corresponding spreading resistance on homogeneous material will be twice the single contact resistance multiplied by a correction for the influence of the proximity of the other probe. This leads for homogeneous material to the two-contact equation [15]:

$$R_{\text{homog,spreading}} = \frac{\rho}{2a} \left[ 1 - \frac{2}{\pi} \arcsin \left( \frac{a}{S} \right) \right] \quad (2a)$$

For sufficiently large probe separations ( $S \gg a$ , i.e. separation equal to more than 20–30 times the contact radius), the resistances of each probe can simply be superimposed, and the equation simplifies to its commonly used form:

$$R_{\text{homog,spreading}} = \frac{\rho}{2a}, \quad \text{for } S \gg a \quad (2b)$$

Assuming for a moment that one has fixed the radius value by performing a measurement on a certified homogeneous sample with known resistivity, one can then use Eq. (2b) to determine the resistivity of any unknown homogeneous sample. This illustrates the fundamental operation of SRP, i.e. the measured resistance is directly proportional to the underlying resistivity and the used contact needs to be calibrated against certified samples.

Eq. (2) predicts a linear response of the spreading resistance on homogeneous samples with different resistivity. For real life data measured with high-pressure, penetrating, non-ideal Ohmic (more Schottky-like), multiple protrusion contacts, the response curve (or calibration curve) is in general, however, non-linear, as illustrated in Fig. 1.

A widely used heuristic approach is consequently to extend Eq. (2) with a resistivity-dependent (generalized) contact resistance component and furthermore to replace the *physical* radius by an apparent, also resistivity-dependent, *electrical* radius. This leads to the generalized equation:

$$R_{\text{homog}} = R_{\text{barrier}}(\rho) + \frac{\rho}{2a(\rho)} \quad (3)$$

for which the physical background will be discussed into more detail in later sections.

For non-homogeneously doped samples, such as, for example, diffused or annealed ion implantation structures, Eq. (3) needs one more fundamental extension. When the sub-layer

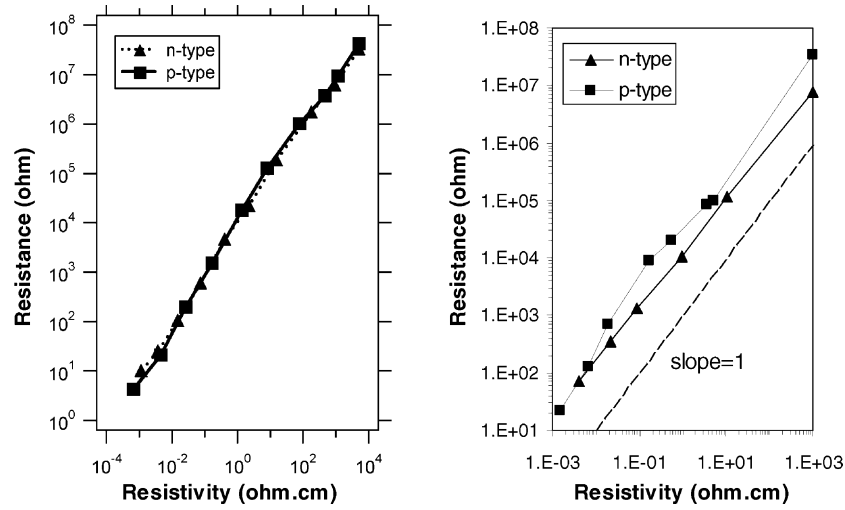


Fig. 1. Calibration (response) curves illustrating the non-linear dependence of the resistance measured on homogeneous samples plotted vs. their certified resistivity [128].

immediately underneath the contacted surface (top) layer has a higher (or lower) resistivity than the top one, the measured resistance will, respectively, be higher (or lower) than expected for a homogeneous sample with the same resistivity as the top sub-layer of the non-homogeneous sample. This is illustrated in Fig. 2. Furthermore, Fig. 3 illustrates on a real depth profile, the significant steeper rise of the resistance when one approaches an underlying junction-isolated layer relative to a single impurity type structure, for the same n-type implantation. In order to be able to extract the same active implantation profile, irrespective of the underlying layer, there is clearly a need for a correction factor CF, which is, in general, dependent on the whole underlying resistivity profile  $\rho(x)$ . The resistance at the surface (depth  $x = 0$ ) is then given by:

$$R_{\text{meas}}(x = 0) = R_{\text{barrier}}(\rho(0)) + \frac{\rho(0)}{2a(\rho(0))} \text{CF}(\rho(x), a(\rho(0)), S) \equiv F(\rho(x)) \quad (4a)$$

and furthermore depends on the (variable) electrical contact radius  $a(\rho)$  and the (fixed) probe separation  $S$ . Further details on the calculation of the correction factor will be discussed later on (Section 4.2.1). Note that this is still assuming a non-penetrating contact.

As it is our intention to determine the entire resistivity depth profile  $\rho(x)$  (at a set of discrete depths  $x_0, x_1, \dots, x_N$  up to the substrate or an insulating boundary), one simple measurement on top of

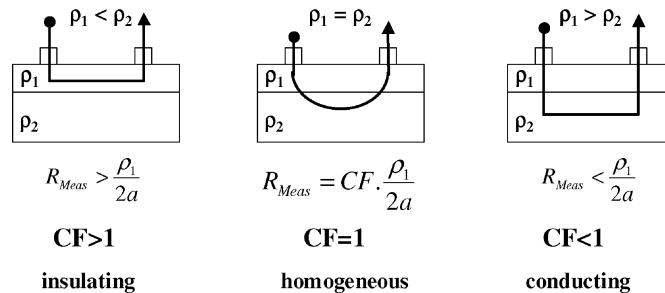


Fig. 2. Need to incorporate a correction factor for non-homogeneously doped structures.

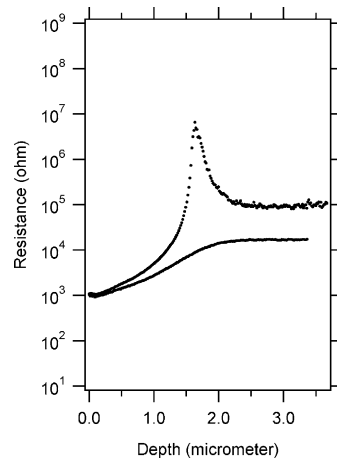


Fig. 3. Raw spreading resistance data for the same n-type implant in p-type (upper curve) and n-type (lower curve) substrate.

the sample is not sufficient to extract a unique solution from Eq. (4a). Hence, in practice, for non-homogeneously doped samples, one needs to gain access to (be able to contact) the in-depth resistivity variations and to determine the corresponding variation in resistance  $R_{\text{meas}}(x)$  over the whole depth scale of interest. This leads to a uniquely solvable non-linear system of equations that can be represented by:

$$R_{\text{meas}}(x = x_j) = R_{\text{barrier}}(\rho(x_j)) + \frac{\rho(x_j)}{2a(\rho(x_j))} \text{CF}(\rho_j(x), a(\rho(x_j)), S) \equiv F_j(\rho(x)) \quad (4b)$$

where  $\rho_j(x)$  and  $F_j(\rho(x))$  contain the contributions from all the underlying layers below depth  $x_j$ .

The inversion problem:

$$\rho(x) = F^{-1}[R_{\text{meas}}(x)] \quad (4c)$$

can consequently be solved by iterating for the single unknown  $\rho(x_j)$  at each depth (triangular matrix) by starting in the substrate where the homogeneous equations can be used to determine the resistivity of the substrate and moving gradually towards the surface until the whole resistivity profile  $\rho(x)$  has been resolved.

Because the size of the SRP probe contacts (few micrometer) is too large to be applied directly on cross-sections, one needs to make a beveled (slanted) surface. By stepping along the beveled surface, one can then collect a resistance versus depth profile from which the in-depth resistivity profile can be extracted through Eq. (4).

To conclude this basic theoretical section, it is important to realize the impact the correction factor has on the dynamic range of the raw data. As illustrated in Fig. 4 for a 10 nm highly doped box profile and the case of a 2  $\mu\text{m}$  radius and 25  $\mu\text{m}$  separation, the dynamic range in the raw data (resistance) is only two decades, while the original dopant profile varies over six orders of magnitude. This reduction in dynamic range is mainly a consequence of the fact that the involved correction factor is as large as 3000, i.e. three decades. The remaining decade is lost in the conversion from dopant density to resistivity (through the non-linear mobility relation). Consequently, when solving Eq. (4c), whereby a signal variation of two decades is expanded to six orders of magnitude, the solution of the inversion problem will act as a strong amplifier and the presence of any noise on the raw data becomes a serious problem. Irrespective of the application of a good smoothing scheme, the best way to alleviate this problem is to keep the correction factor as close to one as possible (see Section 3.2).

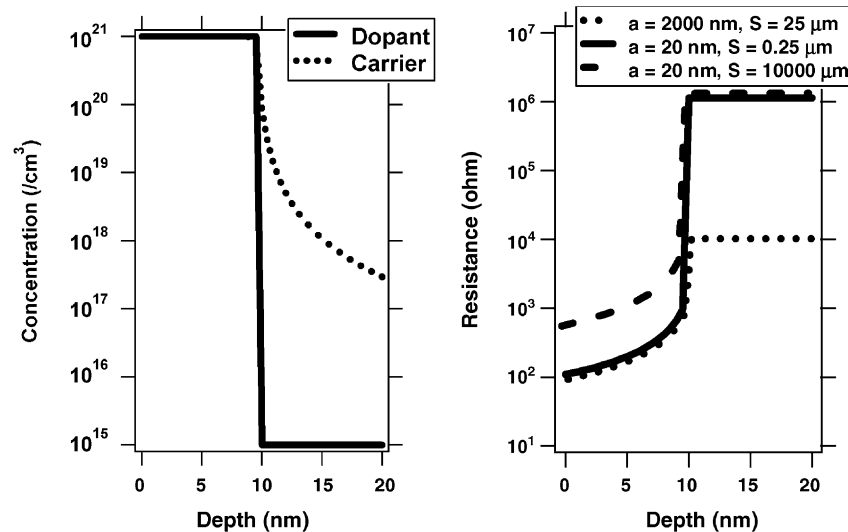


Fig. 4. Dependence of the raw data dynamic range for a given fixed dopant profile for different contact radii and probe separations.

## 2.2. Experimental

The practical implementation of the SRP technique is therefore as follows (see Fig. 5). A small piece of the material (about  $3 \text{ mm} \times 5 \text{ mm}$ ) is mounted on a bevel block with an angle appropriate for the depth scale one is interested in. Next, the bevel block is mounted onto a piston (with a thumbscrew) and placed into a polishing cylinder, within which it can move up- and downward. The latter is then pressed against a rotating frosted glass plate lubricated by a high grade of diamond paste. Typically, a few minutes of polishing are sufficient to obtain the beveled surface needed to get in-depth access to all sub-layers. Subsequently, the bevel block with the sample is mounted on the SRP tool and the two metal measurement probes (typically consisting of a tungsten–osmium alloy) are properly aligned with the bevel edge. Finally, the measurement itself involves stepping both probes along the beveled

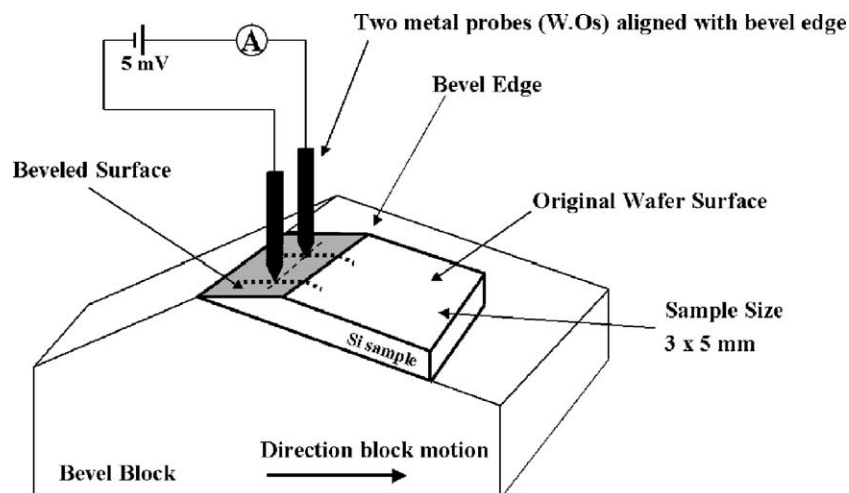


Fig. 5. SRP measurement setup.

surface, starting on the original surface before the bevel, until the substrate depth is reached. At each step, the resistance at low bias (5 mV) is recorded. This procedure results in a one-dimensional raw data profile, which initially consists of the measured resistances versus their respective lateral positions (expressed as measurement point number). Note that the raw data profile thus obtained will only be quantifiable when probes are used with good and reproducible electrical characteristics. The process of preparing such probes is referred to as the probe conditioning procedure (Section 3.2.2).

Given the lateral probe step size set on the tool and after the measurement of the actual bevel angle with a profilometer, it is, in principle, straightforward to convert the lateral position scale into the real depth scale one is interested in (assuming a perfectly flat bevel plane and straight bevel edge). The starting point of the depth profile, i.e. the point with depth zero positioned exactly at the bevel edge, is typically determined with a high-magnification ( $500\times$ ) optical microscope (in the absence of a capping oxide).

The conversion of the measured resistance scale into the underlying resistivity scale, which represents the actual physical variable being sampled by SRP, is, as already indicated, in general governed by Eq. (4). One must, however, realize that the characteristics of the probe–semiconductor contact change continuously. Therefore, each day reference (calibration) measurements need to be made. These measurements generate calibration curves (Fig. 1), relating resistivity to resistance (for homogeneous material) being the fingerprints of the probe characteristics at a given moment in time.

For unknown structures consisting of a single impurity type with very slow in-depth variations ( $5\text{--}10\text{ }\mu\text{m/decade}$ ), i.e. quasi-homogeneous relative to the contact radius of about  $1\text{ }\mu\text{m}$ , these calibration curves can be used directly to convert their resistance scale into resistivity (without the need to use the correction factor, i.e.  $\text{CF} = 1$ ). For silicon-based structures, the obtained resistivity values can then be converted to carrier density values through the known mobility relations for bulk material [16] (assuming that the involved material satisfies the theoretical mobility relations). This results in the final SRP output, i.e. the carrier concentration depth profile.

For any structure that is, however, somewhat more complex, i.e. has steeper depth variations and/or consists out of multiple impurity sub-layers, one needs to take into account an increasing number of physical issues (proportional with its complexity), in order to be able to recover accurately the underlying electrically active portion of the dopant profile. A primary issue is whether the beveling process itself does or does not distort the shape of the carrier profile at the concentration levels one is interested in. For high concentration levels (above  $10^{18}\text{ atoms/cm}^3$ ), which determine the underlying sheet resistance, and not too shallow profiles (deeper than  $100\text{ nm}$ ), this distortion is expected to be limited and a Laplace-based multi-layer analysis (for the calculation of the correction factor in Eq. (4)) can be used provided radius and contact resistance calibration are properly taken into consideration. For lower concentration levels, which determine the apparent on bevel electrical junction depth, and shallower profiles (sub- $100\text{ nm}$ ), the impact of the presence of a bevel is non-negligible, and a Poisson-based analysis is required involving issues such as carrier spilling (redistribution of carriers relative to the fixed ion positions), lateral three-dimensional current flow and surface charge (states) due to surface damage (Sections 4.2 and 4.3).

Once the extracted carrier (resistivity) depth profile is available, it is straightforward to calculate from it the corresponding sheet resistance value for insulating layers. This value may, in certain cases, differ from conventional four-point probe (FPP) measurements, as the latter are typically done with probes at significantly higher loads ( $100\text{ g}$ ) than in SRP ( $5\text{ g}$ ), i.e. may suffer from short circuits (higher penetration) through underlying sub-layers. In case of doubt, one can exclude possible modeling artifacts in the SRP depth profiling extraction, by performing a so-called SRP probe spacing experiment (Section 4.4).



Obtaining the electrically active dopant profile for complex sub-micrometer structures with a qualified SRP tool can be done today in less than 1 h, with a nanometer geometrical depth resolution and an accuracy and reproducibility of 10% (in the absence of carrier spilling effects), as indicated by a recently conducted international round robin. However, the difficulty in achieving this performance lies in the necessity to reach a high level of expertise in all aspects contributing to the final result. It is the aim of this review to help the interested reader in doing so.

### 3. Raw data collection

Any information lost during the raw data collection can never be recovered afterwards, irrespective on how sophisticated the applied correction schemes may be. Issues which are crucial to this respect are achieving flat beveled surfaces with low roughness (low noise level) and a sharp bevel edge (starting point accuracy), the usage of low penetration (dynamic range) probes with small contact sizes (small correction factors), a sufficiently high data density (depth and concentration accuracy), avoiding the presence of photo-electrical currents (darkness), the need for data points far before the bevel edge for shallow structures (pre-bevel resistance increase correction), the usage of a high-magnification microscope linked to appropriate visualization software for the starting point determination (depth scale accuracy) and finally the application of an appropriate smoothing algorithm (for instance, a least squares, constrained cubic spline algorithm) for the removal of the inevitable measurement noise while maintaining the underlying real features of the collected raw data.

#### 3.1. Sample preparation

To achieve flat beveled surfaces, with low roughness and a sharp straight bevel edge, under an appropriate angle one needs to pay attention to the sample mounting (bevel angle), sample polishing (quality polishing plate, grade of diamond paste, procedure itself), the issue of bevel rounding (need for oxide-capping layer) and for patterned structures, the minimum size requirements for reliable measurements.

##### 3.1.1. Sample mounting

The smaller the sample the better the bevel surface roughness will be. Taking into account ease of handling, a typical size of 2–3 mm × 4–5 mm is recommended.

First, a bevel block has to be selected which magnifies the targeted profile depth scale such as to be able to record a sufficient number of data points with the intended on bevel probe step size (see also depth resolution section). The bevel angle  $\alpha$  transforms the real depth scale  $x$  into the magnified lateral, on bevel distance scale  $z$  through the formula:

$$z = \frac{x}{\sin(\alpha)} \quad (5)$$

where  $M(\alpha) = 1/\sin(\alpha)$  is the magnification factor of the applied bevel. Table 1 shows the magnification factors and corresponding depth resolutions for some typical angles as used today.

When beveling, for example, a 50 nm deep profile under a  $0^\circ 04'$  angle, this results in a magnified on bevel region of about 43  $\mu\text{m}$ . With a probe step size of 1  $\mu\text{m}$ , this results in 43 raw data points, or a geometrical depth resolution of approximately 1 nm per point. In most cases, a similar depth resolution can be achieved, either by choosing a larger step size in combination with a smaller



Table 1  
Typical magnifications and corresponding depth resolutions as used today

Bevel angle ( $\alpha$ )	Magnification ( $M(\alpha)$ )	Depth resolution ( $\Delta z$ , nm)	
		For 1 $\mu\text{m}$ step size ( $\Delta x$ )	For 2.5 $\mu\text{m}$ step size ( $\Delta x$ )
0°04'	859	1.16	2.90
0°08'	429	2.33	5.82
0°17'	202	4.95	12.37
0°34'	101	9.90	24.75
1°09'	50	20.00	50.00
2°52'	20	50.00	125.00

angle, or vice versa. In order to avoid overlapping probe imprints, it is recommended to choose the larger probe step size, provided one is able to produce sharp enough (not-rounded) bevel edges at the required bevel angle.

Eq. (5) intrinsically assumes a perfectly flat bevel plane intersecting along a straight line with the original surface. In practice, however, bevel rounding [17] may occur near the bevel edge and can distort the depth scale and subsequent quantification as discussed into more detail in Section 3.1.3.

The (large) horizontal magnification sets immediately a limit to the use of SRP on patterned devices. This is further discussed in Section 3.1.4.

Subsequently, the sample is mounted with wax near the bevel block edge, with its small side parallel to the edge. The temperature of the bevel block (and the sample) during the melting of the wax for the mounting and unmounting of the sample is typically not higher than 80 °C. Hence, there is no danger for any redistribution of the impurities in the sample to be measured.

For achieving the very small angles below 5–6', the inevitable tilt of the sample, due to the non-uniformity of the underlying wax film, may lead to angles very different from the nominal bevel block value. Due to lack of positioning control, more than one attempt may be required to achieve precisely the targeted small angle.

As the actual angle is always different from the one indicated on the bevel block, the former needs to be measured accurately, for example, with a profilometer or an other instrument with a similar capability for angle measurements.

### 3.1.2. Sample polishing

A new glass plate needs to be prepared before it can be used for beveling SRP samples. The recommended procedure for doing so has been discussed in detail by Pawlik [5]. The goal is to achieve an rms surface roughness of ideally 0.13  $\mu\text{m}$  (for the glass plate). The underlying idea is that the size of the used diamond particles in the lubrication suspension (diamond paste) is such that they stick out just a little bit from the scratches in the glass. The typical speed of the rotating glass plate is about 30–60 rpm. It has been reported that not all types of glass are equally well suited to be used for beveling purposes [18].

Ideally, a very high grade (0.05  $\mu\text{m}$ ) of diamond paste in oil suspension is required for high-quality SRP bevels [5]. It should be noted that this grade of diamond paste is only available from very few manufacturers. A slightly worse grade of diamond will result in too many large scratches in the bevel surface and too much noise. The target is to achieve a 2 nm rms bevel surface roughness (or better) [7].

The usage of, for example, water or another lubricant will result in much too rounded bevel edges (see next section) with unwanted complications for the start point determination. Fig. 6 (right) illustrates the sharpness of the bevel edge one should try to achieve.

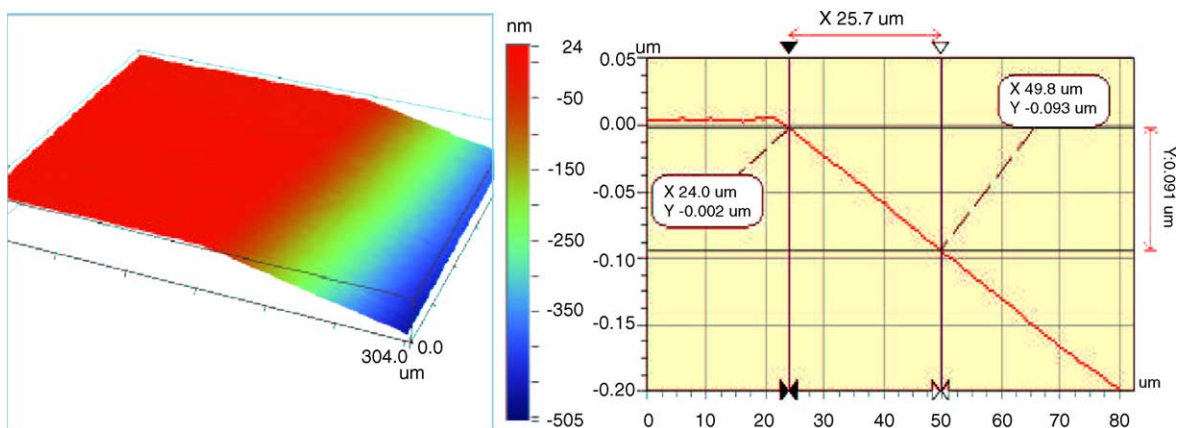


Fig. 6. Example of sharp bevel edge with an angle of  $12'15''$  as measured with a Veeco optical profilometer (WYKO 3300). (Left) 3D image; (right) cross-section; graph dimensions: total height 250 nm, width 80 μm (no oxide cap used).

After the mounting of the bevel block (with the attached sample) into its cylindrical holder, the holder should thus be positioned on the rotating glass plate that the original surface points in the direction of the glass plate rotation. Hence, small particles that are being removed will be swept away from the sample and not clutter up near the bevel edge causing unwanted scratches. Fig. 7 shows a comparison of a poorly and well-beveled surface. Only the latter one can be used for quantitative SRP profiling.

After successful completion of the polishing process and prior to the actual measurement, the sample needs to be cleaned thoroughly (for example, by ultrasonic cleaning). The ultimate surface should be clean, stable in time and reproducible. The latter may be mechanically and electrically strongly dependent on the polishing steps and leave variable amounts of surface charge (cf. the earlier work on Syton and Quso [19]). Deterioration of the surface over longer periods of time (months, years) has been reported [20] (H-diffusion).

### 3.1.3. Oxide-capping layer (bevel rounding)

Dependent on the applied polishing procedure, more or less bevel rounding may occur. Examples for Metadi, Syton and Quso based polishing are to be found in literature [17,21]. Bevel rounding causes a non-linear distortion of the expected depth scale, i.e. the measurement points at constant

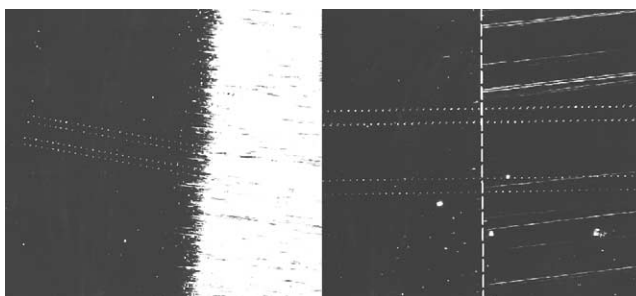


Fig. 7. Comparison of a poor (left) and a good (right) bevel surface. The bevel is each time on the right-hand side. Dark-field image. The parallel, more or less horizontal tracks of small dots are the probe imprints. The vertical white dashed line in the right part is the bevel edge. The other white lines on both images are scratches (not always completely perpendicular to the bevel edge).

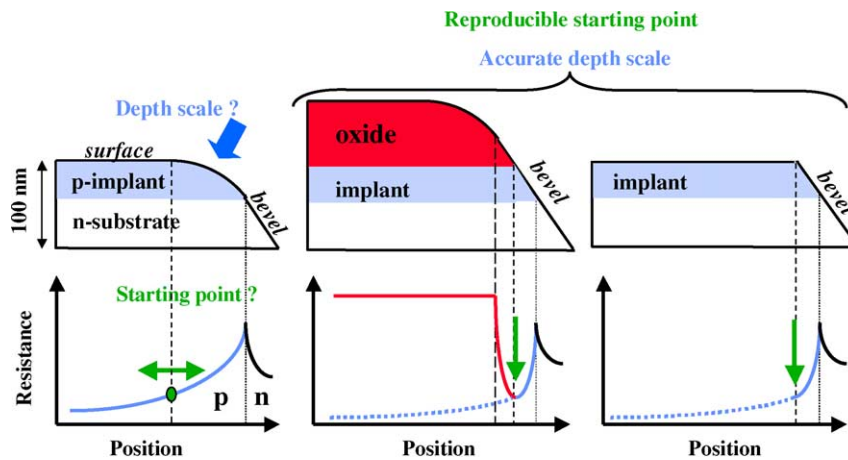


Fig. 8. (Left) Erroneous depth scale due to bevel rounding. (Middle) With capping oxide, the depth scale in the silicon is correct. (Right) After removal of capping oxide, a sharper bevel edge is obtained.

lateral steps along the rounded portion of the bevel have actual depth increments smaller than expected from the overall bevel angle measurement. In-line laser interferometer bevel angle measurements [21] (simultaneous with the resistance measurements) have illustrated that such distortions can cause unreal near surface dips (and distorted sheet resistance values) in the extracted carrier depth profiles. Optimized oil-based polishing procedures as used today, however, can reduce bevel rounding to a minimum, and there is routinely no correction performed for it.

If for some reason, a sufficiently sharp bevel edge cannot be achieved relative to the profile depth one is interested in, one can improve considerably the depth scale accuracy by the deposition of a 100 nm thick, low temperature CVD oxide (200 °C) prior to the beveling process, as illustrated in Fig. 8. This is a procedure that, for example, has proven to be useful in the characterization of ultra-shallow (sub-100 nm) structures.

When beveling a sample with an oxide-capping layer, the eventual bevel rounding will be located in the capping layer. Hence, the depth scale in the underlying silicon material remains unaffected. If access to the original surface of the silicon top layer is required (see Section 4.2.7), one either will have to measure the surface resistance prior to the oxide deposition or either remove the capping layer after the beveling. The latter can be achieved by a short dip in a diluted HF–HCl solution (1 ml HF (50%)–5 ml HCl (30%)–100 ml deionized water). It needs to be verified that the applied oxide deposition process does not lead to any unwanted profile distortions.

#### 3.1.4. Small area measurements (patterned devices)

Although typically applied to samples cut from blanket (monitor) wafers, SRP can also be applied to small sized, doped areas on patterned wafers. The minimum size needed to be able to obtain an SRP depth profile is directly related with the required depth resolution and applied probe separation.

For a sub-micrometer depth profile, for example, with a magnification of about a factor 100 (16' angle), a beveled surface of at least 100  $\mu\text{m}$  will be required. Taking into account the difficulty in realizing such a bevel, the sample size in the direction of the measurement (orthogonal to the probes) should be at least 300–500  $\mu\text{m}$ .

The impact of the presence of insulating (reduces current spreading = higher resistance) or conducting boundaries (increases current spreading = lower resistance) in the direction perpendicular to the probe alignment has been investigated [3] for boundary spacings (separations) in the range from

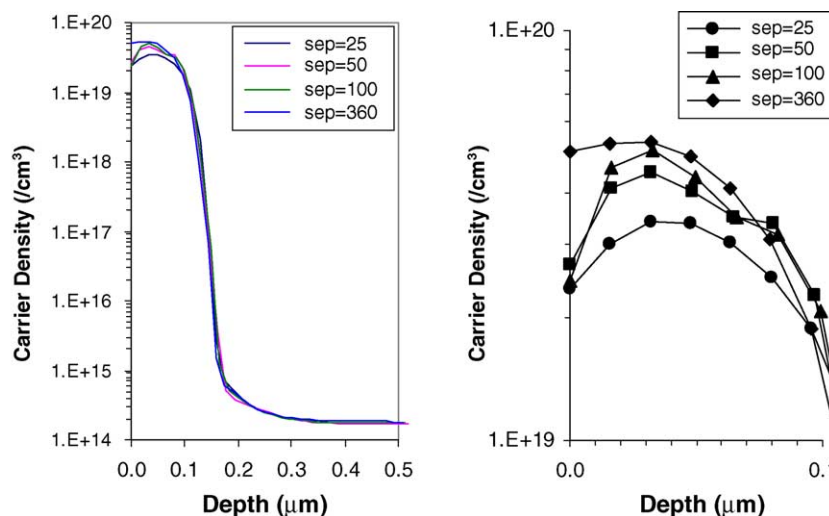


Fig. 9. (Left) Source/drain implant measured in between two oxide stripes with separations as indicated (in  $\mu\text{m}$ ). The probe separation was  $15\text{ }\mu\text{m}$ . (Right) Magnification of the concentration peaks.

25 up to  $450\text{ }\mu\text{m}$ , while performing the measurements in the middle between the boundaries. Fig. 9 illustrates the impact of the proximity of two insulating oxide boundaries on the carrier profile of a source/drain implant measured with a  $15\text{ }\mu\text{m}$  probe separation. A significant difference in profile shape (lowering of up to a factor of two of the peak concentration level) can be observed for oxide stripe spacings below  $80\text{--}100\text{ }\mu\text{m}$ , i.e. about five to six times the probe separation. Hence, the closer the probes can be put to each other the smaller areas can be measured reliably. Besides being able to measure smaller areas, there are other advantages in bringing the probes closer together as discussed in the next section. Oppositely, experiments where profiles have been measured as close as  $10\text{ }\mu\text{m}$  from conducting boundaries revealed no significant lateral current shunting and the presence of close conducting boundaries can therefore be safely ignored in SRP.

### 3.2. Probe preparation

The spreading resistance is measured between two metal probes, which are pushed against the silicon surface. For optimal dynamic range and resolution, the penetration depth and contact size of these probes should be as small as possible. As these requirements are basically in conflict, an optimization is required. On the other hand, with non-penetrating probes, the resistance would be dominated by the resistance through the native oxide and be almost not sensitive to the underlying profile. Also the separation of the probes should be kept to a minimum.

#### 3.2.1. Probe load and separation

Initially, relatively high probe loads ( $10\text{--}20\text{ g}$ ) were used, as these improve the contact properties and reproducibility (formation of Ohmic contact penetrating through the native oxide). Although adequate for deep, slowly varying depth profiles, they are too penetrating for sub-micrometer depth profiling for which the usage of  $5\text{ g}$  (or even less) is mandatory. Achieving this requires a careful design consideration of the total system (such as the usage of specially designed low weight probe arms).

In the state in which probes are bought, they cannot be positioned closer than about  $100\text{ }\mu\text{m}$  from each other. However, the smaller the probe separation, the smaller the correction factors

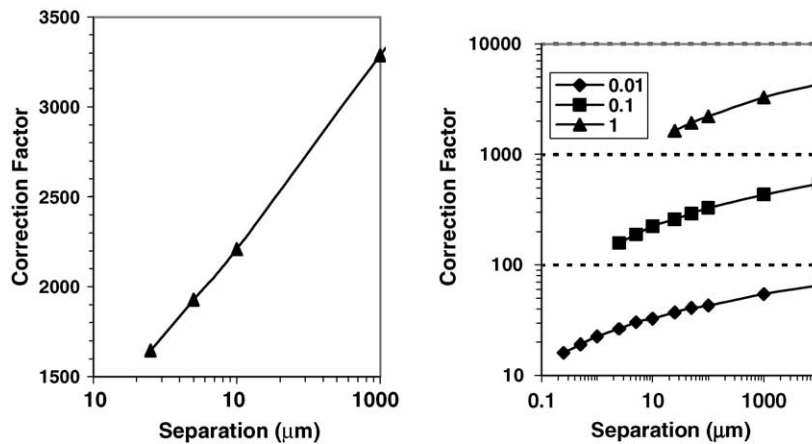


Fig. 10. (Left) Variation of the correction factor with probe separation for a contact with 1  $\mu\text{m}$  radius and for a 10 nm junction insulated box profile (doping level  $10^{21}$  atoms/cm<sup>3</sup>). (Right) Variation for other contact radii (in  $\mu\text{m}$ ).

needed for the resistivity extraction will be and thus the more accurate the conversion as illustrated in Fig. 10.

Bringing the probes closer together can be achieved by removing (abrasion) from each probe, part of its side directly opposite to the other probe and close to its own probe tip (as illustrated in Fig. 11). Well-prepared probes can be positioned as close as 20–30  $\mu\text{m}$  from each other as is required for sub-micrometer profiling. The actual setting is typically verified through a high-resolution microscope inspection of the probe tracks.

### 3.2.2. Probe conditioning

Ideally good SRP probes should provide an Ohmic contact to the sample (also on high resistive material) with an area as small as possible, while penetrating (deforming the sample) as little as possible. For a given load these are, however, conflicting requirements. Perfect spherical indentors, which have a size similar to SRP probes (probe curvature radius of about 10  $\mu\text{m}$ ) and use pressures in the same range (50 mN), have a contact radius of about 1  $\mu\text{m}$  and a penetration depth of about 400 nm [71]. Although the radius is quite attractive (see further), the penetration is unacceptable for SRP, as one wants to resolve sub-micrometer (and sub-100 nm) depth profiles. In principle, using blunter

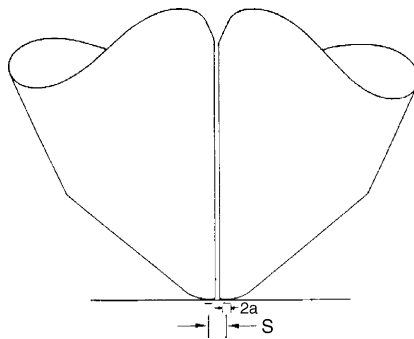


Fig. 11. Illustration of how the abrasion of probe sides opposite to each other enables them to come as close together as 20–30  $\mu\text{m}$ .

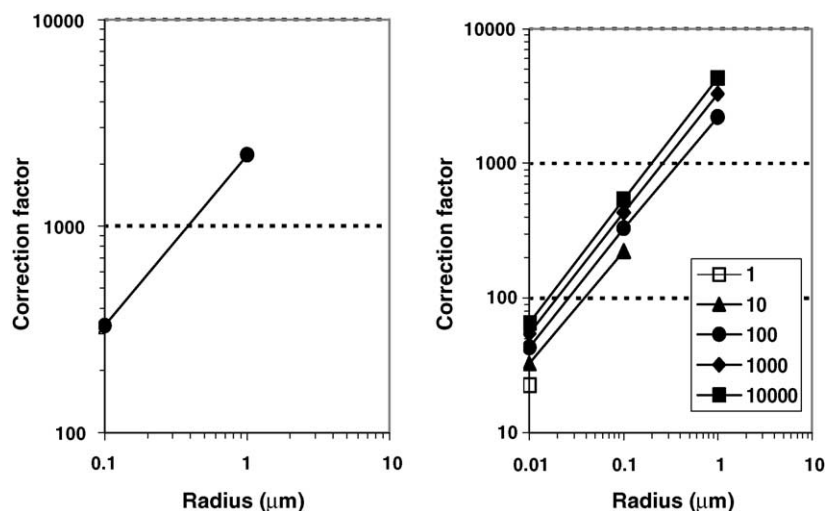


Fig. 12. (Left) Dependence of the correction factor on the contact radius for a 100  $\mu\text{m}$  separation on a 10 nm box profile doped  $10^{21}$  atoms/ $\text{cm}^3$ . (Right) Dependence for other separations.

spherical indentors can alleviate the penetration problem, but these will automatically lead to larger contact radii. This again is unacceptable as the size of the earlier discussed correction factor is, even more than the probe separation, dependent on the contact radius. This is illustrated in Fig. 12. Hence, an optimal equilibrium between contact size and penetration depth is not trivial.

The optimization starts from the observation that the key to achieving a low noise probe–silicon contact is the creation of a body-centered tetragonal  $\beta$ -tin (metallic) Si(II) phase immediately underneath the probes [22]. The phase transformation requires local pressures of up to 10–12 GPa, which are also sufficient to break through the native silicon oxide. At the same time, one wants to keep the size of the contacts as small as possible in order to reduce the size of the correction factor as much as possible as illustrated earlier. Applying a high pressure on a small contact, however, tends to lead to a large probe penetration. The latter needs, however, to be avoided as otherwise the spreading resistance of several sub-layers will be sampled simultaneously and Eq. (4) (assuming a planar contact on a single sub-layer) will no longer be valid (and thus also the inversion solution). Hence, the load needs to be minimized in order to contact as few differently doped sub-layers as possible leading to a high electrical depth resolution. Furthermore, one needs to establish a reproducible electrical contact over many thousands of measurement points. Finally, one should realize that, microscopically, a contact is rarely based on a perfectly planar surface contacting the silicon surface, but rather is composed of several asperities on the tip apex. Practice has shown that high-quality probes with a long lifetime are based on a large number of closely spaced, small micro-contacts at the extremity of the probe tip. Fig. 13 shows the topographic image of the imprint of an optimally prepared probe as obtained from an atomic force microscope (AFM).

The process of the creation of a micro-contact distribution appropriate for SRP measurements is referred to as probe conditioning. This process cannot be monitored directly, i.e. visually, on a daily basis. Analyzing a dedicated set of calibration samples monitors probe conditioning. The interpretation of these measurements is the basis of adjusting the probe conditioning process. This is one of the most time consuming and difficult parts of the whole SRP profiling process and requires an operator with a high expertise. For a given set of probes, the conditioning process can take from a few days up to more than a week, or it may fail completely. The lifetime of the conditioned probes is dependent on the initial quality of the probes, the type of layers being measured and the care taken during the



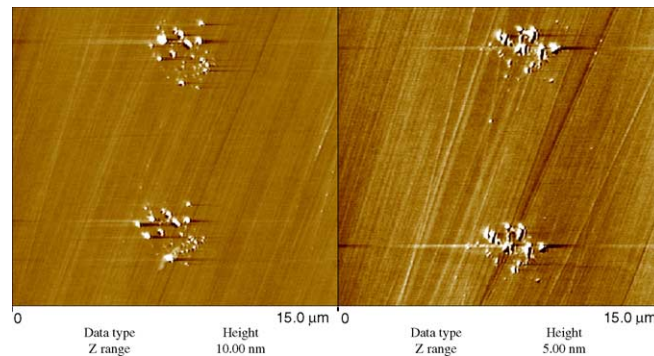


Fig. 13. Imprints of well-conditioned probes as imaged by atomic force microscopy (AFM).

measurements and can, in general, range from a few weeks to a few months. Exceptionally, periods of more than a year have been reported [23].

The probe conditioning procedure, as it is performed today in state-of-the-art laboratories, is based on achieving specific target values on a range of special control samples through a series of repetitive actions to, respectively, roughen, shape, and smooth the extremity of the probe. For the roughening and smoothing, the probes are put down repetitively on high concentrations of diamond paste on sapphire plates with different grades over the range 0.25, 0.5 and 1.0  $\mu\text{m}$ . The finest grade results in a smoothing effect, while the coarsest results in a roughening effect. The middle grade gives an intermediate result. For obtaining probes with small contact areas, it is mandatory to be able to shape the probe tips, i.e. to remove small parts of tips near its extremity. For this a special tool, called a probe shaper, as shown in Fig. 14 is required. More details on how to proceed with probe conditioning when starting from fresh probes can be found in [5].

One can discriminate between primary and secondary probe control samples. Achieving the target values for the first ones is the most difficult part of the work. Once these values have been met, the probes only need minor improvements to satisfy also the secondary target values. The target values for the control samples as used by the authors are listed in Table 2. The fourth control sample, i.e. the n·p·n·p bipolar transistor, by itself is a very sensitive tool for probe quality monitoring. Fig. 15 shows the raw data quality (cusp heights) one needs to achieve.

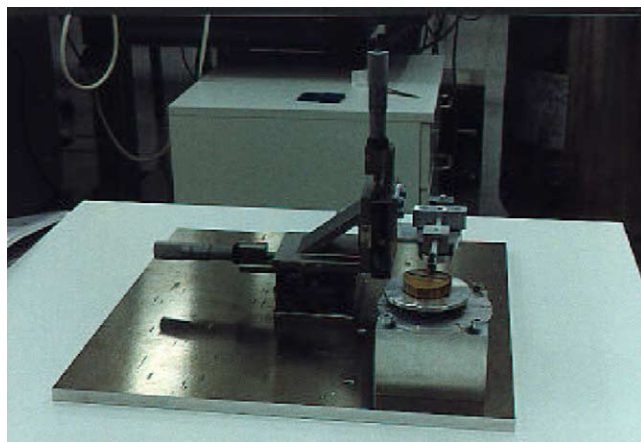


Fig. 14. Probe shaper tool required to reduce the size of the tip during probe conditioning.



Table 2

Target values to be achieved during probe conditioning on probe control samples

	Sample/action	Target
Primary control samples/actions	$\langle 111 \rangle$ n-type, 0.002 $\Omega$ cm alloyed back-contact	7–15 $\Omega$ per probe, <3% standard deviation
	$\langle 111 \rangle$ p-type, 100 $\Omega$ cm diffused back-contact	0.4–1.0 M $\Omega$ per probe, <10% standard deviation, <factor 2 rectification
	Optical examination probe imprints, dark field, magnification 500–1000 $\times$	Presence of plastically deformed micro-contacts, total area smaller than 2 $\mu$ m radius, no dominant features, uniform distribution micro-contacts
Secondary control samples	n-p-n-p bipolar transistor with 100 nm base width	Dynamic resistance range over base at least one decade, no difference in cusp height in forward or reverse biased probes
	OP08 (NIST calibration sample)	<5% standard deviation on noise with both probes
	OP16 (NIST calibration sample)	0.5–10 M $\Omega$ with both probes, <10% standard deviation

The final target is to achieve probe imprints that consist out of a large number (20–50) of densely packed, small (10–20 nm) micro-contacts each having a penetration of not more than 5–10 nm. The global radius of the physical imprint should be less than 1  $\mu$ m.

### 3.3. Data collection

Once a well-beveled sample and a well-conditioned set of probes are available, one can proceed with the actual raw data collection. Issues, which require attention here, are the bevel edge alignment of the probes (dynamic range), the need to do the measurements in the dark (elimination of photo-electrical effects), the number of data points (data density), where to start the measurement and how to smooth away the noise on the raw data adequately.

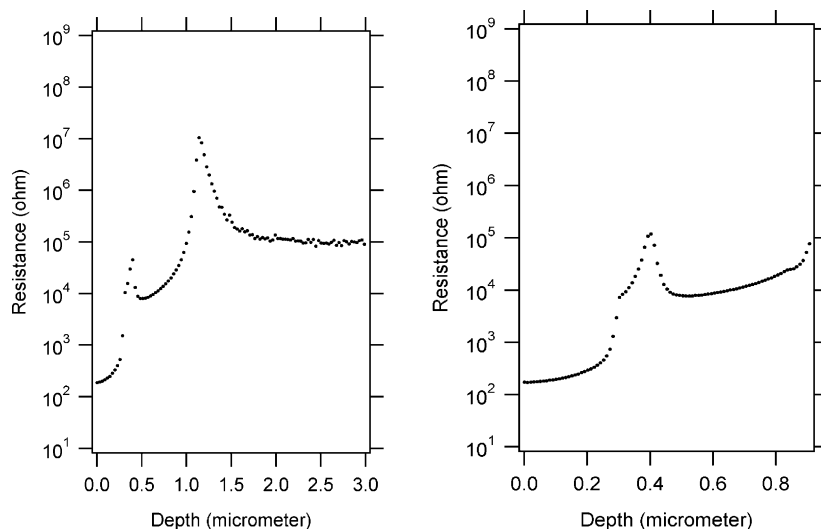


Fig. 15. (Left) Raw data obtained with well-conditioned probes on p-n-p-n bipolar control transistor. (Right) Magnification of the base region.

### 3.3.1. Bevel edge alignment

As two separate probes are used during the measurement, it is crucial that as they move together over the beveled surface, they contact precisely the same sub-layer, i.e. are at equal distance from the bevel edge. Otherwise, the measurement will inevitably suffer from a loss in dynamic range and depth accuracy in the determination of, for instance, the electrical junction between two layers of different impurity type. Electrically this can, for example, be verified with the aid of the bipolar control transistor as discussed in the probe conditioning section, which is very sensitive for probe misalignment. Typically, a junction peak will be reduced and often forward and reverse bias will lead to different measurements when probes are misaligned. Afterwards, the alignment can also be verified by investigation of the probe imprints on a separate high-magnification microscope.

### 3.3.2. Photo-electrical currents

Practice has shown that the SRP measurement circuits can output wrong resistance values [24], especially in the neighborhood of electrical junctions, apparently due to the presence of unwanted photo-electrical currents generated by the light impacting the sample. Therefore, it is highly recommended to perform all measurements in the dark.

### 3.3.3. Depth resolution

The depth resolution is determined by the bevel angle and the lateral probe step size used. Dependent of the complexity of the structure (different impurity sub-layers with highly differing thicknesses), it may be necessary to use multiple depth resolutions (multiple bevels) to fully characterize the structure.

In order to get reasonably reliable quantitative carrier levels in a particular sub-layer, one needs at least 20 and preferably more than 30 data points. For shallow sub-50 nm layers, this means one has to achieve a 2–3 nm depth resolution, which will require bevel angles as small as a few minutes when using a lateral step size of 1  $\mu\text{m}$ . When using such small step sizes, the probe imprints will inevitably overlap as they have a typical size of 2  $\mu\text{m}$ . It has been verified that this leads to a moderate (10–20%) increase of the resistance relative to the case without overlap, and that by using calibration curves which have been recorded under the same conditions, this will have little impact on the final accuracy of the measurement.

### 3.3.4. First measurement position

At first sight, one might assume it is most convenient to take as the first measurement position one which is as close as possible to the bevel edge (or even exactly on it), because it then agrees directly with the start point of the depth profile. In practice, however, this is rarely done, because there remains always some doubt on the correctness of the first point due to the limited capabilities of the on-line microscope. In general, the first measurement position is taken at least 10–20 data points before the start of the bevel (on the original surface) or before the oxide–silicon interface in the presence of a capping oxide. The start point of the depth profile itself can then be determined as indicated in the next section.

For structures which are shallow enough (irrespective of whether they are junction-isolated or not), it may be necessary to take even much more data points before the bevel edge (e.g. 100) or to perform the measurement in two stages, i.e. first measure 20–30 points very far away from the bevel (on the original surface) and then to do the normal measurement starting 10–20 points before the bevel edge (or cap oxide–silicon interface). The underlying problem for structures with a shallow junction-isolated top layer is that the resistance will already start to increase before one has reached the bevel edge, i.e. the resistance at the bevel edge may be significantly larger (more than one order of magnitude

for sub-50 nm layers) than far away from the bevel (on the original surface). We will come back to this issue, which is referred to as the pre-bevel resistance increase problem (Section 4.2.7). In order to be able to correct for this important problem, we need to have the undistorted measurement data far away from the beveled (damaged) surface. For samples with an oxide-capping layer, the later will have to be removed in such a case.

### 3.3.5. Start point depth profile

The careful determination of the actual start point ( $x = 0$ ) of the depth profile is obviously very important especially as, in many cases, it lies in a highly doped portion of the profile (e.g. source/drain extensions) and therefore has a large impact on the final accuracy of the integrated dose and corresponding sheet resistance of the top impurity sub-layer.

The best way to determine the depth profile start point (in the absence of a capping oxide) is by using a high-magnification ( $500\times$ ) microscope in combination with a computer-aided visualization system. First a high-magnification image of the region of interest taken in dark-field illumination mode is stored in the visualization software. Next, two lines parallel with the bevel edge are drawn interactively on the screen, one representing the bevel edge itself, and one going through the first measurement point. Then, the distance between these two lines is measured orthogonal to their direction. This distance is then divided by the known lateral probe step size set on the SRP tool, and thus results (after rounding to the nearest integer) in the measurement position number corresponding with the start point of the depth profile, i.e. the measurement point on the bevel edge.

In the presence of an oxide-capping layer, the above procedure can also be used taking the oxide–silicon interface as the bevel edge. Alternatively, the starting point can be determined directly from the electrical resistance depth profile [25], as illustrated in Fig. 16. The initial drop in resistance (depth A) corresponds with the point where the first micro-contact (of the whole SRP contact) makes electrical contact with the underlying silicon material. Dependent on the step size, angle and probe penetration it will take between 2 and 10 measurement points, before the whole probe exclusively contacts the silicon (depth B). Traditionally, the latter point (B) is considered to be the starting point of the depth profile. For ultra-shallow profiles, the difference between depths A and B typically lies around 5–10 nm.

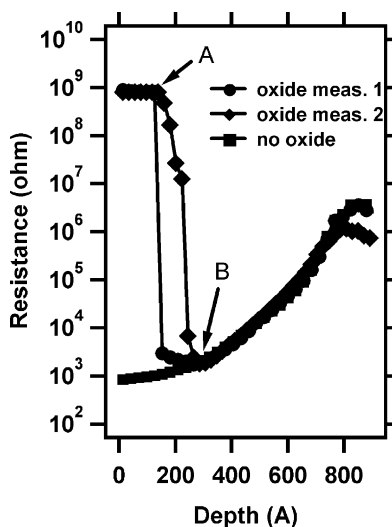


Fig. 16. Raw data for an ultra-shallow source/drain profile, as obtained from two different measurements with a capping oxide vs. a measurement after cap removal.

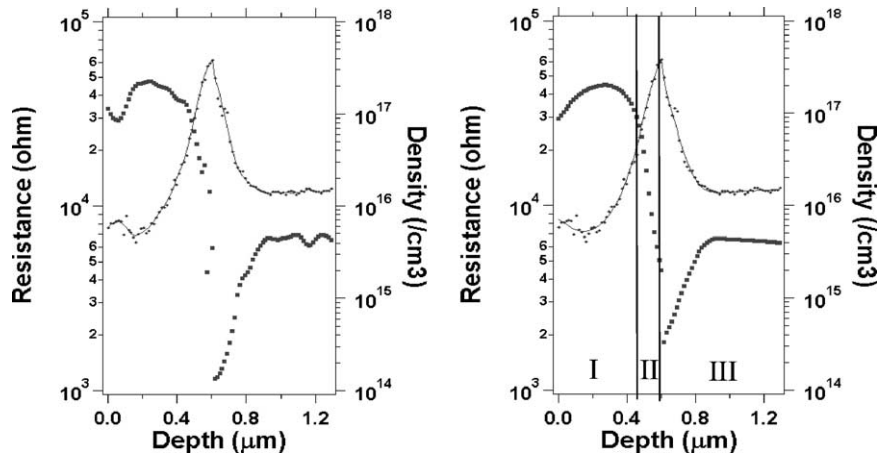


Fig. 17. Comparison of the impact of smoothing on the final carrier depth profile. The small dots are the raw data, the line is the smoothed raw data, and the larger dots are the carrier profile. The left part illustrates a general smoothing scheme, the right part illustrates the specialized constrained cubic spline scheme. Region I = convex; region II = concave; region III = convex.

This value relates directly to the amount of probe penetration (see Section 4.2.6). Note that, as illustrated by Fig. 16, the transition behavior can be dependent on the local oxide–probe characteristics, but that both resistance depth profiles coincide from the starting point onward. In most cases, the actual starting point can be deduced from a significant change in behavior in the raw data (kink in the resistance curve). It should be noted that in the presence of a capping oxide on ultra-shallow structures some extra care must be taken regarding the near surface data smoothing [25]. For completeness, Fig. 16 also shows the raw data profile obtained after removal of the oxide-capping layer. Note the pre-bevel resistance increase.

### 3.3.6. Data smoothing

Even the raw data profiles collected under the best possible conditions will inevitably have a non-negligible amount of noise. Typically, the noise levels are higher for p-type than for n-type material, and for medium and lowly doped p-type relative to highly doped p-type (Section 4.3.7).

Because the resistivity (and carrier) extraction algorithms to be discussed further on act as strong amplifiers of noise, it is crucial to smooth the raw data profiles prior to their deconvolution. However, while doing so we want of course to distort the underlying real physical profile as little as possible. Many different algorithms have been proposed to this respect [26]. Over the past decade, it has become evident that one algorithm, proposed in 1986, is especially well suited for this task [5]. It is referred to as constrained cubic spline (CCS) smoothing [27]. It implements a least-square fitting of a cubic spline function to the raw data, while taking into account constraints on its second derivative, i.e. convexity and concavity constraints (see Fig. 17). Although the latter have to be pre-defined interactively by the user, practice has proven, that this is in the majority of the cases by no means a critical step nor a limitation of the algorithm. Fig. 17 illustrates the performance of the CCS smoothing scheme relative to a less optimized scheme for a sub-micrometer implantation profile.

## 4. Data analysis

Once high quality raw data are available, the next step is to extract from them the underlying electrical depth profile, i.e. resistivity and/or carrier concentration profile, as accurately as possible,

i.e. by staying as close to the physical phenomena involved as possible. The number of physical phenomena to be taken into account is proportional with the complexity of the structure being characterized. For very slowly varying ( $20\text{ }\mu\text{m/decade}$ ) single impurity (no junction) structures, one can suffice with the simple direct inversion of the measured resistance data into the corresponding resistivity through the usage of the calibration curves. As steeper transitions are involved ( $1\text{--}2\text{ }\mu\text{m/decade}$ ) and/or multiple sub-layers with different impurities (junctions), more elaborated Laplace-based schemes need to be applied. Finally, for the most demanding structures, such as ultra-shallow ones with the steepest transitions ( $10\text{ nm/decade}$  or steeper), but also near the depletion region of some deeper slowly varying junction-isolated implants, one needs to take into account the impact of carrier spilling (diffusion) and a Poisson-based analysis is mandatory. Ultimately, deviations from the 2D plane approximation are required and 3D current spreading effects need to be considered.

#### 4.1. Direct inversion

In order to be able to extract the underlying resistivity (or carrier) information from the measured resistance profile, it is always necessary to have a record of the probe characteristics at the moment of the measurement. This can, for example, be done by recording the resistance of the probes on a set of calibrated, homogeneously doped samples. This results in a conversion curve between resistance and resistivity, named the calibration curve. Each impurity material (n- or p-type) has its own calibration curve. Once such calibration curves are available, they can be used for the direct inversion of very slowly varying depth profiles. The resulting resistivity depth profiles can then be converted to carrier density profiles through the knowledge of the crystalline mobility relations for the used dopant species. Note that this assumes that these relations are valid for the sample under study. If lower mobility would be present, SRP will correctly determine the resistivity profile, but underestimate the carrier concentration (Eq. (6)).

##### 4.1.1. The calibration curves

Originally calibration curves were always obtained by measuring a large set (at least seven to eight for each impurity type) of homogenous, calibrated samples covering the resistivity range of interest. Recently, a specialized, epi-layer-based, staircase structure has been introduced, which allows for the much faster and daily recording of these calibration curves (only one sample for each impurity type).

**4.1.1.1. Homogeneous calibration samples.** The National Institute of Standards and Technology (NIST) along with other sources [28] have been supplying since the early beginning, homogeneously doped SRP calibration samples. The complete set consists out of 16 samples for each impurity type. They cover the range  $6.61 \times 10^{-4}$  to  $76.75\text{ }\Omega\text{ cm}$  for  $\langle 1\ 0\ 0 \rangle$  p-type, and  $1.14 \times 10^{-3}$  to  $179.3\text{ }\Omega\text{ cm}$  for  $\langle 1\ 0\ 0 \rangle$  n-type silicon. In dopant density, this corresponds to  $2 \times 10^{20}$  to  $2 \times 10^{14}\text{ atoms/cm}^3$  for p-type and  $7 \times 10^{19}$  to  $2 \times 10^{13}\text{ atoms/cm}^3$  for n-type. For optimal accuracy, each of these samples (32 in total) should be measured before measuring the unknown samples. In practice, typically half (or even less for n-type due to its highly linear calibration curve) are being measured. Nevertheless, it is still time consuming to measure let say 12 calibration samples each day. Therefore, in practice, the latter is not always done every day in all laboratories. It has, however, been shown that this is a crucial requirement in order to achieve a high level of accuracy and reproducibility [7].

Calibration curves depend on bevel surface quality and the step size used during the resistance measurements. Obviously, the same polishing procedure needs to be used for the calibration samples as for the unknown samples to be measured. Typically, 20–30 measurement points are taken on each

sample and their average and standard deviation is calculated. It is known that when using small step sizes for which the probe imprints start to overlap, the measured calibration resistance goes up by 10–20%. Therefore, one needs to pay attention to always use calibration curves in agreement with the step size with which the unknown samples have been measured.

Typically, n-type calibration curves will be quite linear, while p-type curves may be highly non-linear. The shape and slope of these curves are highly sensitive to the precise conditioning of the probes, especially for p-type material. The latter can be related with the presence of a thin n-type inversion layer on p-type doped layers caused by the presence of filled surface states induced by the beveling process (Section 4.2.6).

As already indicated, the main focus of the probe conditioning process is to create a large amount of densely packed, small micro-contacts, resulting in a small probe penetration and reproducible electrical performance. For such qualified contacts, both the n- and p-type calibration curves will be quasi-linear and have a slope larger than one. These are important characteristics in order to be able to apply the more elaborate Laplace- and Poisson-based deconvolution schemes.

**4.1.1.2. Epi-layer staircase calibration.** The determination of the calibration curves can be speeded up substantially by using the staircase structures introduced a few years ago [29]. These structures consist, as illustrated in Fig. 18, out of a series of homogeneously doped calibration stairs (about 5  $\mu\text{m}$  thick) separated by thinner, slightly more highly doped, interface layers (about 1  $\mu\text{m}$  thick). The thickness and dopant level of the interface (shielding) layers has thus been designed that the resistance measured on the flat calibration stairs is equivalent with separate homogeneously doped structures (which is non-trivial taking into account the impact of differently doped sub-layers as discussed further on). As the p-type calibration curve is more non-linear, the p-type staircase structure contains seven different calibration levels, while the n-type one only contains five.

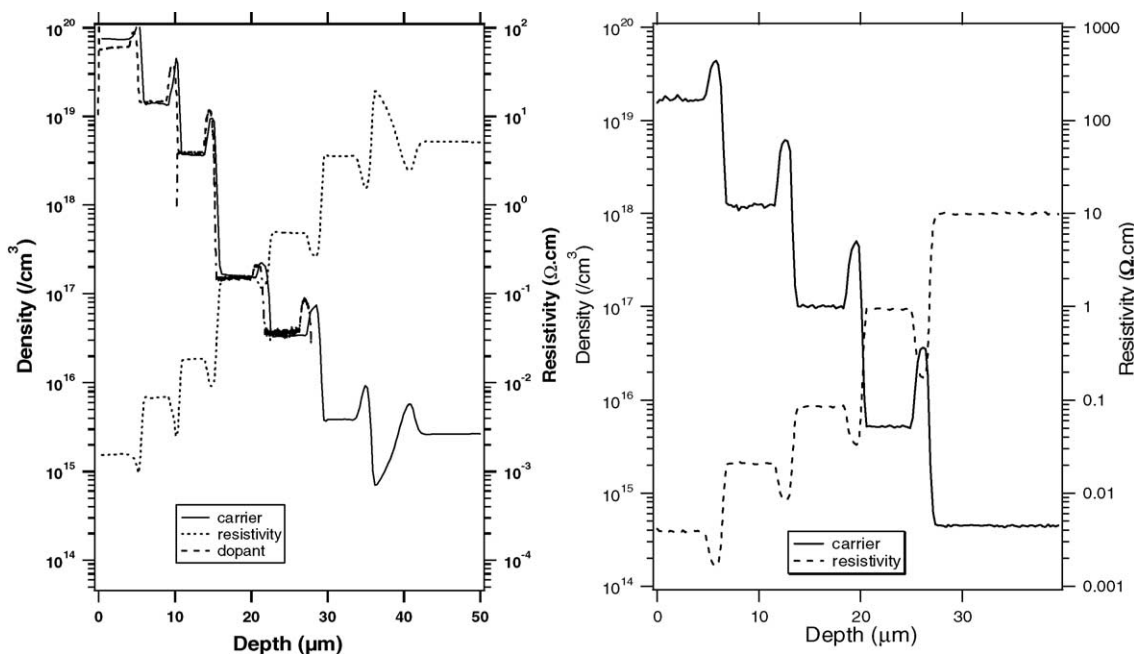


Fig. 18. Epi-layer staircase structures for calibration purposes. (Left) p-type; (right) n-type. The dashed line is resistivity, the full line is carriers and the short dashed line is total dopant (as measured by SIMS).

As only two staircase samples need to be measured, one for p-type and one for n-type, to obtain a complete set of calibration curves, this can easily be done on a daily basis and thus greatly improves the reproducibility of the final SRP results [7].

#### 4.1.2. The resistivity and carrier concentration profile

For structures with very slow in-depth dopant variations (and no junctions), their resistivity profile can be obtained in a straightforward manner from the measured resistance profile by direct inversion, i.e. by direct conversion through the measured calibration curves (Fig. 1) for the impurity type involved. For the interpretation of a resistance value in between two measured calibration values, it is recommended to use linear interpolation on a log–log scale.

Once the resistivity profile  $\rho(x)$  is available, it is a straightforward process to obtain for crystalline silicon material, the corresponding carrier density  $n(x)$  through the usage of standardized mobility relations  $\mu(N(x))$  for n- and p-type material, where  $N(x)$  represents the total dopant density. The formula used is:

$$n(x) = \frac{1}{q\rho(x)\mu(N(x))} \quad (6)$$

where  $q$  is the elementary charge. The recommended mobility model is the one proposed by Thurber [16]. For slowly varying profiles, the carrier  $n(x)$  and dopant levels  $N(x)$  can be set equal to each other (if one can assume complete activation). Vice versa, a comparison between  $n(x)$  and  $N(x)$ , as obtained, for instance, with SIMS, will enable to determine the degree of electrical activation.

#### 4.2. Laplace-based modeling

For all but the simplest structures, direct inversion will not be sufficient to extract the correct underlying resistivity (and carrier) profile. This is a direct consequence of the different impact a more highly or more lowly doped sub-layer will have on the current distribution under the probes (and therefore the measured resistance) on a given reference surface layer. The interpretation of the measurement is further complicated by the presence of a large number of micro-contacts instead of an ideal, flat, circular contact. Also the probe–semiconductor contact (or barrier) resistance needs to be taken into account. In certain cases, a probe penetration correction may be required. Finally, the surface roughness has been found to play a non-negligible role in the measured resistance for shallow enough sub-layers, and needs to be corrected for in those circumstances.

In Laplace modeling, typically, a heuristic approach is taken towards the physical modeling of the probe–bevel surface contact, where one quantifies non-spreading resistance components through calibration without the need for a deep physical understanding of the internal operation of the contact. In the upcoming Poisson sections, relating to the so-called carrier spilling phenomenon, however, a deeper insight into the internal contact physics is mandatory and, hence, will be discussed at that point.

##### 4.2.1. Schumann–Gardner multi-layer theory

As soon as (constantly doped) sub-layers start to become thinner than a few times, the contact radius they start to influence the resistance measured at the contacted sub-layer along the bevel surface. Consequently, for such structures, it is no longer possible to use direct inversion, but a more elaborate solution of the full Laplace equation is needed.

After some initial attempts Schumann and Gardner [30] achieved a first breakthrough when they proposed their multi-layer (Fig. 19) correction factor algorithm. Assuming the resistance contributions of both probes can be superimposed, they determined a theoretical expression for the solution of the



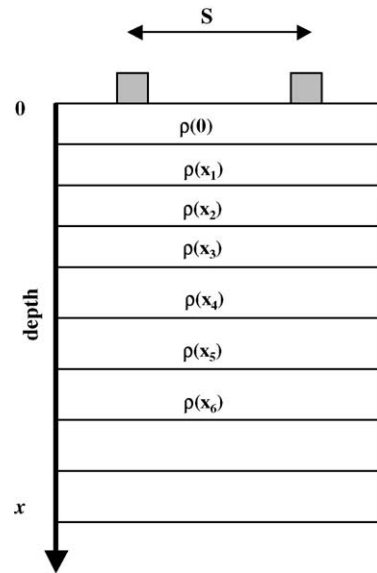


Fig. 19. Multi-layer structure with multiple differently doped sub-layers where the probes contact the top layer.

three-dimensional problem of current flowing through a single ideal, Ohmic, flat, circular contact with radius  $a$  and a large back-contact in the presence of a variable number of different (constantly) doped sub-layers. This expression is:

$$R_{\text{meas}} = \frac{\rho(0)}{2a} \text{CF}(\rho(x), S, a) \quad (7)$$

with

$$\text{CF} = \frac{4}{\pi} \int_0^\infty K(t, \rho) I(t, a) \left[ \frac{J_1(at)}{at} - \frac{J_0(St)}{2} \right] dt \quad (8)$$

where  $a$  is the contact radius and  $S$  is the probe separation. A crucial part of this formula is the so-called correction factor CF. It contains three main parts: first, there is the kernel term  $K(r)$ , which takes into account the impact of the underlying layers (resistivities and thicknesses); second, the current density term  $I(a)$ , which depends on which assumptions one makes regarding the current density distribution under the contact (semi-infinite slab, uniform or ring delta function); and third, a combination of first- and zero-order Bessel functions, which relates to the two-probe setup being considered (radius, separation). For homogeneous material, the correction factor  $(1 - (2/\pi)\arcsin(a/S))$  is almost equal to one. For insulating boundaries, the measured resistance will be higher than expected and, therefore, the correction factor will be larger than one. For sub-50 nm insulating layers, the correction factor can become as large as a factor of 1000. On the other hand, for conducting boundaries, the opposite will be the case, and the correction factor will be smaller than one (down to 1/1000).

The practical implementation of the crucial formulas (7) and (8) was initially, however, hindered by the difficulty in accurately evaluating the integral in the formula (containing Bessel functions with different oscillation frequencies), the long calculation times needed to solve the large set of non-linear equations (proportional to the number of measurement points) and the appropriate choice for the current density function underneath the probes.

A second breakthrough was established by Choo et al. [31] when a recursion relation was proposed, which allowed the resistivity profile to be calculated point by point starting in the substrate, i.e.

eliminated the need to solve large systems of non-linear equations. This was accomplished by defining the kernel term for the  $n$ -layer problem in terms of the simpler  $(n - 1)$ -layer problem, as follows:

$$K_n(t) = \frac{w(t)\rho_n + \rho_{n-1}K_{n-1}(t)}{\rho_n + w(t)\rho_{n-1}K_{n-1}(t)} \quad (9)$$

with

$$w(t) = \frac{1 - e^{-2td}}{1 + e^{-2td}} \quad (10)$$

where  $d$  is the layer thickness.

From then on, it was possible to perform calculations, both simulations and deconvolutions, in a reasonably fast time and to start focusing on the accuracy of the computation, i.e. the optimization of the numerical integral calculation and its relation with the choice of an appropriate current density model.

#### 4.2.2. Current density model

Over the years, different current density models have been studied while maintaining the assumption of a single flat circular contact, ranging from the uniform current model to the semi-infinite slab model. Dependent on the model used, different solutions for the integral calculations were proposed [32].

In 1981, Berkowitz and Lux [33] made a new breakthrough with their very fast integrator based on the uniform current model, which was shown to perform well in a large variety of circumstances. It has consequently been implemented in many SRP deconvolution software tools, and is still being used today.

The research group of Choo et al. has further refined this work and proposed a variational algorithm [34,35], in order to cope even more accurately with all kinds of structures. The latter algorithm is based on a combination of the uniform current density and semi-infinite slab current density model, where the amount of each current is varied according to a variational principle. An ultimate accuracy of up to 1% was demonstrated. As indicated by the authors themselves, the differences with the uniform current model are, however, never expected to be larger than 10%.

#### 4.2.3. Micro-contact distribution

As structures in the sub-micrometer range were measured more frequently, it became apparent that especially for lowly doped on highly doped structures, as can be made in an epi-reactor, the interface resistivity (and carrier) levels obtained from the Schumann–Gardner (SG) algorithm could be very much in error as compared to, for example, secondary ion mass spectrometry data. Fig. 20 illustrates the problem for an implantation and epi-layer structure. Initially, explanations relating to surface states [36] and contact (barrier) resistance [37] as expected to be present on the beveled surface and due to the metal–semiconductor contact were proposed. Although the latter do play a role in SRP as we will see further on, obtaining correct epi-layer results is first of all a matter of taking the micro-contact distribution [38], opposite to the ideal circular contact, properly into account.

The presence of the micro-contacts can be taken into account by splitting up the measured resistance into two separate components, the *self-resistance* and the *interaction term*. For homogeneous material, Eq. (2) therefore needs to be replaced by:

$$R_{\text{homog}} = \rho \left( \frac{1}{2na_\mu} + \frac{1}{2\alpha} \right) \quad (11)$$

The self-resistance (first term in Eq. (11)) relates to the resistance of the individual micro-contacts when they are far away from each other, and depends on the total number of micro-contacts  $n$  and on

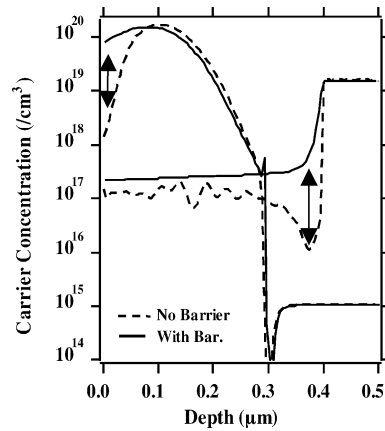


Fig. 20. Impact of the contact modeling on the extracted carrier profile. The black lines are closest to the corresponding SIMS profile.

their average contact radius  $a_\mu$ . The interaction component starts to play a role when the micro-contacts are close together as is the case in SRP, and depends on the so-called Holm radius  $\alpha$ , which defines the circle within which all the micro-contacts are located. For a qualified SRP system (see further on) and for homogeneous material, both components are approximately equally important, i.e. contribute each for about 50% to the total resistance. In this context, the single radius as used in Eq. (2) is sometimes called the effective radius  $a_{\text{eff}}$ . It follows from Eqs. (2) and (11), that:

$$\frac{1}{a_{\text{eff}}} = \frac{1}{na_\mu} + \frac{1}{\alpha} \quad (12)$$

For non-homogeneous material, the relative contribution of the self-resistance and interaction component becomes dependent on their different sensitivity depth, which is proportional to the involved radius, and is the largest for the interaction term. The measured resistance is then given by the formula:

$$R_{\text{meas}} = \frac{\rho}{2na_\mu} \text{CF}(\rho, a_\mu, S) + \frac{\rho}{2\alpha} \text{CF}(\rho, \alpha, S) \quad (13)$$

For lowly doped on highly doped structures (with Schumann–Gardner correction factors smaller than one), the correction factor of the interaction term will be the smallest, and therefore the self-resistance term will dominate (see Fig. 21, left). Consequently, as one moves away from the low/high interface (towards the surface), the resistance will flatten out much more quickly than expected based on a single large circular contact (dashed line in Fig. 21, left). If such raw data are incorrectly deconvoluted with a single large contact radius, this will result in an overshoot of the correction factor algorithm, and lead to typical profile artifacts close to low/high interfaces as shown in Fig. 20.

On the other hand, for junction-isolated structures (with SG correction factors much larger than one), the interaction term (which resembles best the single circular contact model) will dominate (see Fig. 21, right). Hence, for such structures, neglecting the impact of the micro-contacts on the measured resistance will only have a limited impact on the final results.

#### 4.2.4. Contact (or barrier) resistance

In SRP, contact is made between two metal probes and a semiconductor. It is well known that the alignment of the Fermi levels in the metal and the semiconductor typically will cause a distortion of the

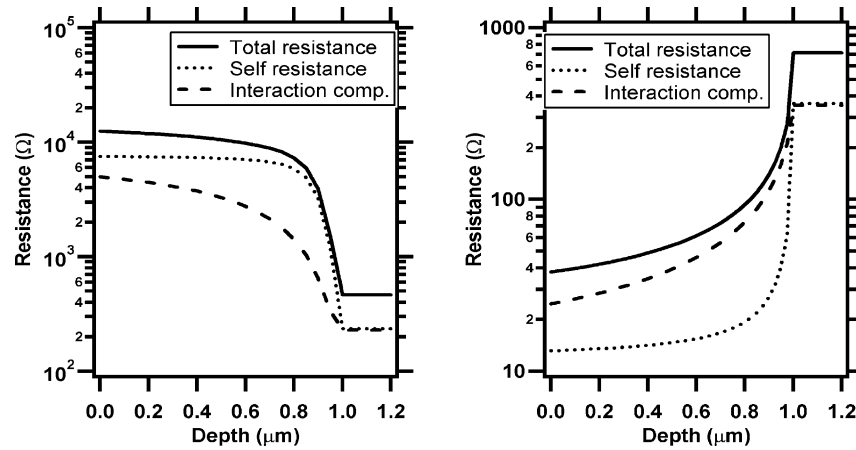


Fig. 21. Relative contribution of the self-resistance and interaction term to the total resistance for (left) a low/high ( $CF < 1$ ) and (right) a high/low ( $CF > 1$ ) structure.

energy bands in the semiconductor, i.e. cause band bending (see Fig. 22), and as such will generate an additional contact resistance [39] (also termed barrier resistance), which is in series with the spreading resistance one is interested in.

The precise Fermi alignment is known to depend on the presence of surface charge and/or surface states on the contacted surface. In the absence of surface states, the amount of band bending in the semiconductor is dominated by the metal work function (Mott theory [13]). In the presence of a large amount of surface states, Fermi pinning will occur prior to establishing contact with the probe, and the band bending in the semiconductor will only be marginally changed when making physical contact with the probe (Bardeen theory [13]). As discussed into more detail in the upcoming Poisson-based modeling sections, where also the important issue of pressure is taken into account, a combination of both cases is considered most appropriate for SRP beveled surfaces.

Dependent on the dopant level, different conduction models (thermionic and/or field emission) for the current density  $J = f(V, \phi_B)$ , as a function of the applied bias  $V$  and barrier height  $\phi_B$ , are valid. Irrespective of the involved model, the specific contact resistivity  $\rho_c$  (expressed in  $\Omega \text{ cm}^2$ ), can be defined as follows:

$$\rho_c = \left( \frac{\partial V}{\partial J} \right)_{V=0} \quad (14)$$

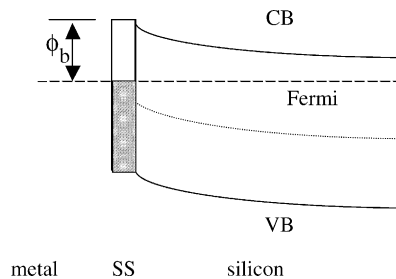


Fig. 22. Band bending responsible for the contact resistance at the metal probe–semiconductor interface. SS = surface states; VB = valence band; CB = conduction band;  $\phi_b$  = barrier height.

Consequently, the total contact resistance  $R_{\text{barrier}}$  at the probe–semiconductor interface can in principle be determined from the formula:

$$R_{\text{barrier}} = \frac{\rho_c}{\pi a_{\text{eff}}^2} \quad (15)$$

Taking into account the presence of a contact resistance component, the general spreading resistance equation becomes:

$$R_{\text{meas}} = R_{\text{barrier}}(\rho) + \frac{\rho}{2na_{\mu}} \text{CF}(\rho, a_{\mu}, S) + \frac{\rho}{2\alpha} \text{CF}(\rho, \alpha, S) \quad (16)$$

For homogeneous material, where  $\text{CF} = 1$ , this simplifies to:

$$R_{\text{homog}} = R_{\text{barrier}}(\rho) + \rho \left( \frac{1}{2na_{\mu}} + \frac{1}{2\alpha} \right) \quad (17)$$

Based on available theoretical (ideal contact) curves for the dependence of the specific contact resistivity on the bias and barrier height, it is possible to obtain a first estimate for the relative importance of the barrier resistance relative to the spreading resistance component one is actually interested in. For a barrier height of, for example, 0.25 eV, Fig. 23 illustrates the behavior of the contact resistance. For highly doped (low resistivity) material, a low contact resistance exists due to the dominance of tunneling through the thin barrier layer. For lowly doped (high resistivity) material, the contact resistance is constant and is dominated by thermionic emission proportional to the barrier height. For intermediate doping (resistivity) ranges a gradual transition of the contact resistance between both regimes occurs. It follows (Fig. 23) that in the medium resistivity range the contact resistance can be of the same order of magnitude as the spreading resistance component, and therefore needs to be taken into account during data analysis.

#### 4.2.5. Radius and barrier calibration

From the general Eq. (16), it follows that in order to be able to deconvolute unknown profiles, it is, in principle, necessary to know the values of the resistivity-dependent radii ( $a_{\mu}$  and  $\alpha$ ), the number of micro-contacts ( $n$ ) and the specific contact resistivity ( $\rho_c$ ).

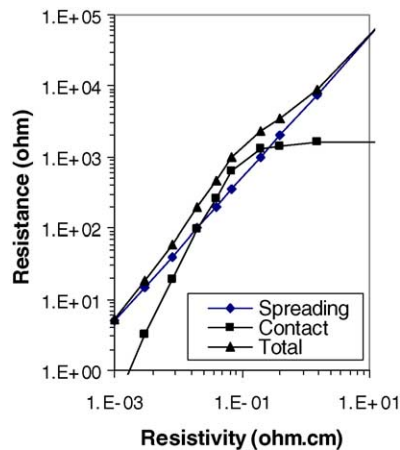


Fig. 23. Comparison of contact resistance vs. spreading resistance for a barrier height of 0.25 eV and a radius of 1  $\mu\text{m}$ .

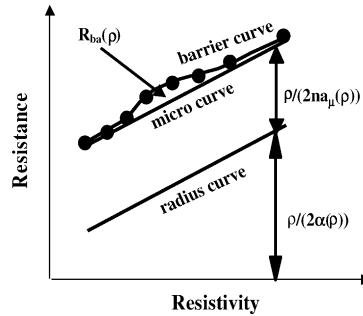


Fig. 24. In theory, three different calibration curves (for each impurity type) determine the complete spreading resistance response. In practice, only the barrier and radius curve are needed.

An alternative formulation is to say that the electrical behavior of the whole probe–semiconductor interface can be fully characterized by three different calibration curves (for each impurity type). The initial (experimental) calibration curves, as introduced in Section 4.1.1, will from now on be termed the barrier calibration curves. Besides these, we introduce, respectively, the radius and micro-contact calibration curves. The relation between these three curves is illustrated in Fig. 24.

The homogeneous, interactive contact contribution is given by the height of the radius curve. The homogeneous, self-resistance component is given as the difference between the micro-contact and the radius curve. The barrier (contact) resistance component is given by the difference of the barrier (measured) calibration curve and the micro-contact curve. The sum of all three components is the measured homogeneous resistance as given by Eq. (17).

In practice, it has been found that one can limit oneself to only two calibration curves, namely the barrier and radius calibration curves. Simulations have shown that for practical purposes the micro-contact component can be combined with the barrier resistance component into a generalized barrier component, denoted  $\bar{R}_{\text{barrier}}(\rho)$ . Hence, the generally applied formula is typically (see also Eq. (4)):

$$R_{\text{meas}} = \bar{R}_{\text{barrier}}(\rho) + \rho \frac{\rho}{2\alpha(\rho)} \text{CF}(\rho(x), \alpha(\rho), S) \quad (18)$$

The accurate determination of the position of the radius calibration curve is therefore crucial for obtaining reliable results. The generally assumed shape for the radius curve is defined by the equation:

$$R_{\text{spreading}} = \frac{\rho}{2\alpha(\rho)} = C\rho^m \quad (19)$$

i.e. a linear curve on log–log scale. Several alternative approaches have been proposed for the determination of the coefficient  $C$  and the exponent  $m$ . Either a sheet resistance matching, an epi-layer matching or a probe spacing experiment can be used.

In sheet resistance matching [44], the radius is optimized in order to get a close agreement between the sheet resistance obtained from the SRP depth profile and an absolute FPP measurement on a well-chosen implantation structure. Typically, the slope of the radius curve is assumed to be one in this case (although this is not necessary). It has been reported that the radius thus obtained is also in close agreement with the radius of the probe imprints in the probe traveling direction [40].

Alternatively, in epi-layer matching, a lowly doped epi-layer with a sharp interface on a highly doped substrate can be used [38], and the shape of the SRP profile is optimized versus the corresponding SIMS profile (minimization of the interface dip). In this case, typically, the slope of the radius curve is taken to be parallel to the slope of the regression line through the barrier (measured) calibration points. Given the high sensitivity of the generalized contact resistance

(containing the impact of the micro-radii), i.e. the difference between the barrier and radius curves, this approach is considered to be the most sensitive one today.

Finally, probe spacing experiments [44,41] have been proposed for radius calibration (Section 4.4.3). A probe spacing experiment involves the measurement of the spreading resistance between the probes for several probe separations on the original (non-beveled) surface of the structure in the absence of a capping oxide. The obtained resistance values are plotted versus the logarithm of their separations ( $S$ ). For junction-isolated structures, the slope of the linear regression line through these data points is proportional to the sheet resistance (Section 4.4.3). Here, it is important to note that it has been proposed that the intersection of this regression line with the  $\ln(S)$ -axis, is a direct measure of the electrical radius. In practice, this approach is still under debate, as significant changes in the intersection value have been reported.

For qualified systems, typically, the radius calibration curve can be positioned at half the height (50%) of the barrier curve. Note, however, that this 50% factor depends on the local probe conditioning procedure, i.e. the precise distribution of the micro-contacts, as has been found during a recent round robin experiment [7]. The slope of the radius and barrier curves will, for qualified systems, typically be larger than one. For non-qualified systems, slopes less than one may be encountered as discussed in the next section.

Due to the non-linearity of the barrier curve, there may occur an intersection between the extrapolation of the barrier curve (through its last two measured points) and the linear radius curve, at the high resistivity end. This situation, which would lead to negative barrier resistance values, can be avoided, either by measuring one or two additional extreme high resistivity homogeneous samples, which are, however, not easy to acquire, or by adding a fictive high resistivity data point to the barrier curve, such that the intersection of both calibration curves is avoided.

It cannot be stressed enough that the usage of up to date (daily) barrier calibration data, in combination with properly derived radius calibration curves is essential for the accurate determination of the resistivity (and carrier) depth profiles. Recall that different bevel surface finishes or different probe steps require each their own sets of calibration curves.

#### 4.2.6. Impact of probe penetration

Note that we have neglected probe penetration up to now in the spreading resistance equations (Eq. (16) or (18)). Probe penetration is expected to have an impact both on the behavior and shape of the calibration curves and on the extraction accuracy of the carrier depth profiles.

Let us first consider the impact on calibration curves. For non-qualified systems, where larger probe penetration depths may occur, this will be reflected in the shape of the barrier (measured) calibration curves. The reason for this is probably related with the existence of surface states along the bevel plane, which may create a n-type surface inversion layer on medium and lowly doped p-type material (see Fig. 25 and Section 4.3.7). For lower penetrations, there will only (or mainly) be conduction through the surface inversion layer, and resistances slightly higher than expected will be measured leading to p-type calibration curves with a slope slightly larger than one. Note that the presence of the n-type inversion layer has been verified, among others, through probe spacing sheet resistance measurements (see Sections 4.4.3 and 4.3.7). For higher penetration, however, as in the case of non-qualified systems, there is a parallel conduction through the surface inversion layer and the substrate leading to lower than theoretically expected resistance values (Section 4.3.7). Hence, especially, for p-type material, the slope of these curves will become smaller than one (for medium or lowly doped n-type material only a surface depletion is expected). It is well known that for such curves, especially if the slopes become less than 0.85, a serious numerical instability can occur in the reverse calculations [42], i.e. when trying to extract the underlying resistivity profile from a



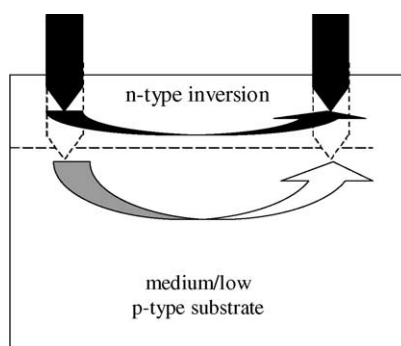


Fig. 25. The impact of probe penetration on the parallel current conduction through a surface n-type inversion layer (due to surface states) and medium or lowly doped p-type bulk material.

measured resistance profile. The threshold for the slope for which this occurs depends on the amount of barrier resistance being used. More barrier allows stable calculations for a smaller radius slope.

If due to penetration the barrier curve has a slope considerably less than one, and a radius curve with a slope of one is being used, again an intersection between both may occur leading to negative, i.e. unacceptable, barrier values. The best way out of this situation is to spend more time in improving the conditioning of the probes, i.e. reduce the probe penetration, which automatically will lead to calibration curves with slopes larger than one and ultimately better quantitative results. Alternatively, one can try to use a radius curve with a slope smaller than one, to avoid the intersection problem.

Second, let us consider the impact of probe penetration on the extraction of carrier depth profiles. Two issues have to be considered here. On the one hand, the measured resistance may become distorted because one is not only contacting the surface layer but also a number of underlying layers. This might lead to wrong dose and sheet values. On the other hand, once close enough to the electrical junction, one expects to penetrate it, hence possibly leading to a too shallow junction (or interface) position and therefore a wrong junction (interface) depth.

Regarding the first issue, i.e. wrong carrier levels, it has been verified that for certain types of structures, such as ultra-shallow source/drain implants with high concentration levels near the surface and therefore virtually no impact of the surface states along the bevel surface, the impact of the 5–10 nm probe penetration is very limited [43]. This is due to the fact that most of the current irrespective of the penetration will flow through the surface (most conductive) layer, and as such will still be proportional to the resistivity one is trying to measure.

Regarding the second issue, i.e. wrong depth scale, it has been proposed that the shape of the two-dimensional electrical junction plays an important role [43]. To understand this, some insight in the carrier spilling phenomenon as discussed in detail later on is required (see Section 4.3). Two extremes can be considered. For source/drain like profiles on a medium doped underlying layer (well structure), the shape of the two-dimensional electrical and metallurgical junctions will not be too different (quite flat and parallel with the original surface). Hence, probe penetration needs to be corrected for, as the junction (or interface) will be penetrated too early by a depth discrepancy equal to the amount of probe penetration. A procedure for doing so has been proposed elsewhere [43]. Alternatively, for a box-like (steep slope) profile on a lowly doped substrate, the shapes of the two-dimensional electrical and metallurgical junctions will be quite different. The electrical junction will remain much deeper than the metallurgical one, until very close to the position where the metallurgical junction reaches the

bevel surface (one to two measurement points). As such, basically no probe penetration correction is required, as the probes basically step “over” the electrical junction, without actually penetrating it.

#### 4.2.7. Pre-bevel resistance increase

Even when applying proper barrier and radius calibration procedures one will observe that as one starts characterizing thinner and thinner layers (sub-100 nm for highly doped source/drain extensions), the sheet resistance values extracted from the deconvoluted SRP resistivity depth profiles are systematically too high relative to absolute FPP measurements [44–46].

This phenomenon can be related directly with an increase of the measured resistance before one has reached the beveled surface, i.e. in the region where in theory one expects a flat resistance curve (along the original surface). Consequently, the resistances on the bevel appear to be too high and, hence, lead to carrier depth profiles, which are too low, with correspondingly wrong (too high) sheet resistance values. The phenomenon is illustrated in Fig. 26, which shows the raw data (and their respective bevel edge positions) for a set of CVD-grown layers with different interface depths. For the deeper structures (sample 4.13), the resistance level remains almost flat up to the depth where the bevel, i.e. the depth profile, starts, as one would expect. However, once the structure depth becomes too shallow, the resistance starts to increase before the bevel edge. For the shallowest structure in Fig. 26 (sample 4.5, 50 nm junction), the pre-bevel increase is already a factor of four. For even shallower layers, increases of more than one decade have been observed.

Besides a possible impact of bevel rounding (which may be non-negligible for very shallow structures in the absence of an oxide cap), two main causes have been identified, i.e. the geometric bevel effect and the surface damage effect.

**4.2.7.1. Geometric bevel effect.** First, if one considers the extreme case of a 90° bevel angle, it is clear that as the probes approach the bevel edge (similar to approaching a cross-sectional edge), the resistance needs to increase by, at most, a factor of two, as only a half plane remains available for the current flow between the probes [45,47]. For two probes on the surface of a junction-isolated layer,

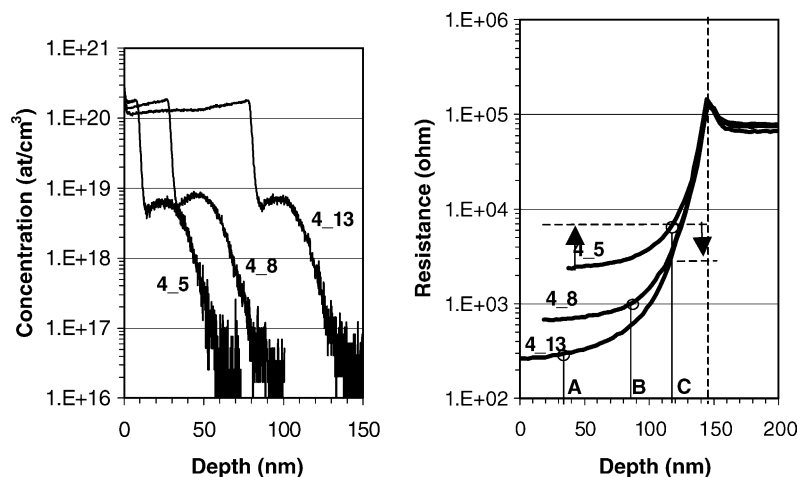


Fig. 26. (Left) CVD-grown layers with different top-layer thicknesses. (Right) Corresponding spreading resistance profiles, aligned to their electrical junctions. This figure illustrates both the impact of the pre-bevel resistance increase component and the lateral 3D current flow component. The depths labeled A–C indicate the bevel edge positions of the curve with the circular marker.

arranged parallel to a cleaved edge, the potential distribution and resistance measured between them can be readily found using the methods of images. The resistance is [47]:

$$R = \frac{\Re}{\pi} (\ln(S) - \ln(a) + \ln(\sqrt{S^2 + \Delta^2})) - \ln(\Delta)$$

where  $\Re$  is the sheet resistance,  $S$  is the probe separation,  $a$  is the contact radius, and  $\Delta$  is twice the distance from the probes to the boundary (the distance to the images). This formula has been confirmed by experiments. This formula has been extended by Dickey [47] to the case of multiple boundaries as involved in the presence of a bevel plane (approximated by a staircase).

This, so-called geometric (bevel) effect [47], is always present in junction-isolated structures and should be accounted for before considering any other factors, especially if the increase is less than a factor of two.

**4.2.7.2. Surface damage effect.** Pre-bevel increases larger than a factor of two may be attributed to two alternative (additional) explanations. First, the beveling process is probably not as ideal and a (modified) damage layer may be created at the beveled surface. The impact of the beveling process on the thickness of a damaged (non-conducting) layer at the bevel surface has been studied [46]. For the highest quality of diamond slurry (maximum size particles 0.1  $\mu\text{m}$ ), a damaged layer thickness of 28 nm was extracted.

Alternatively, the modified layer could be described as resulting from surface states along the beveled surface [48]. Basically, the presence of the surface states induces a thin depletion (or inversion) layer, which narrows the already ultra-shallow layer. Consequently, the sheet resistance in between the probes is now the parallel resistance of the depletion (inversion) layer (due to surface states) and the remaining (undamaged, narrowed) layer. For highly doped junction-isolated layers, this circuit is dominated by the second component, which is now higher than without surface states (narrowed layer, i.e. pinch-off effect).

Consequently, it will appear as if an additional surface damage component, denoted  $R_{\text{damage}}$  along the layer in between the two probes has appeared, which is in series with the barrier and spreading resistance components at the probes themselves (see Fig. 27). Note that this pinch-off effect does not exist when considering thicker junction-isolated layers or homogeneous samples, explaining why no pre-bevel increase is seen in these cases. The term surface damage component has been chosen as the surface states distribution is expected to be dependent on the surface roughness of the bevel surface. Hillard et al. [49] has presented some evidence for the latter. The latter approach has the main advantage that it can explain the pre-bevel resistance increases of more than a decade, as observed experimentally on ultra-shallow structures.

If no surface damage correction is performed, the integrated dose for shallow structures (e.g. source/drain extensions) will be too low and the corresponding sheet resistance too high. Note that for

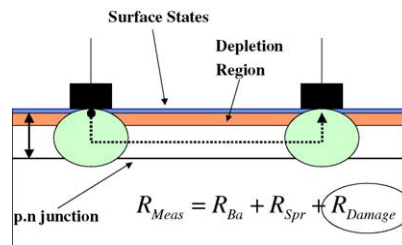


Fig. 27. Illustration of how the depletion region due to the surface states on the bevel narrows the current path between the probes and hence leads to an additional surface damage component.

a surface layer this phenomenon can be directly recognized by the pre-bevel resistance increase which remains after the correction for the geometric bevel effect has been performed. However, it is always present, also for thin, junction-isolated sub-layers deeper within the structure. For example, the base region of a bipolar transistor will also suffer from this problem. In practice, however, the problem is most frequently of importance for surface layers, and correction schemes have, up to now, focused only on this special case.

The simplest possible correction (for thin surface layers) is to subtract from all raw data up to the first electrical junction a fixed surface damage resistance component. The latter can easily be obtained, provided there is no capping oxide on the sample, by subtracting the resistance very far away from the bevel (on the original surface) from the resistance measured on the bevel edge.

If one, however, takes a closer look at the underlying mechanism causing the surface damage problem (depletion layer due to surface states), it becomes clear that as the probes move over the bevel and get closer to the next electrical junction, actually the impact of the surface damage component is expected to increase, i.e. to be inversely proportional with the distance from the next electrical junction. Consequently, for ultra-shallow structures, it is to be expected that a proportional (depth-dependent) scheme, as, for example, proposed by Pawlik [44], gives better results than the constant damage correction scheme.

#### 4.2.8. Three-dimensional effects

Both in the Laplace-based modeling and the upcoming Poisson-based modeling, it is assumed that there is only current flow between the probes in the region underneath the plane running through the probes and parallel with the original surface. Consequently, if one has two structures with, for example, different thickness, which have an identical dopant profile shape below a given reference depth, one expects to measure exactly the same spreading resistance at that reference depth irrespective of any possible differences between them above this reference depth.

However, recent work has indicated that this is not the case. Comparison of SRP data on CVD-grown, almost ideal box profiles (Fig. 26), with different thickness, has shown that for a given reference depth the resistance decreases proportional with the thickness of the structure [50]. For example, in Fig. 26, at depth position C ( $\sim 120$  nm), the resistance of the structure labeled 4\_8 is  $3500\ \Omega$ , while for the shallower one labeled 4\_5 it is twice as much, i.e.  $7000\ \Omega$ , at the same distance (25 nm) from the underlying junction-isolated interface (and identical depth profile between depth C and the interface). This implies that for shallow enough structures, there is indeed a lateral three-dimensional current flow through the higher lying regions of the structure (relative to the probe depth), which can significantly distort the raw data (Fig. 28).

Quantitative three-dimensional device simulations have confirmed this. The first structure (Fig. 29) was, a five-step staircase bevel, with step heights of 10 nm and a step width of  $1\ \mu\text{m}$ , i.e. a magnification of a factor 100. A p-type Gaussian dopant profile with peak concentration of  $10^{19}$  atoms/cm<sup>3</sup> (on top of a  $10^{15}$  atoms/cm<sup>3</sup> background) and a steepness of 5 nm/decade was used (insulating boundary at 50 nm depth). A single, 40 nm size, square contact was defined in the middle of the step located at 30 nm depth, and at a distance (separation) of  $10\ \mu\text{m}$  from a large side contact. The thus obtained current density lines are equivalent with two identical contacts at double separation. The second structure (not shown) was a flat surface, which was basically the first one, from which the top three 10 nm sub-layers (steps) had completely been removed (and the last step had been made twice as high), corresponding to the idealized case of a pure planar geometry without 3D effects. The calculations show that the current density distributions for both structures (bevel versus flat) are significantly different. In the bevel case (Fig. 29), the current tends to flow first to the more highly doped surface layers (in the upward direction) and then laterally towards the side contact through the

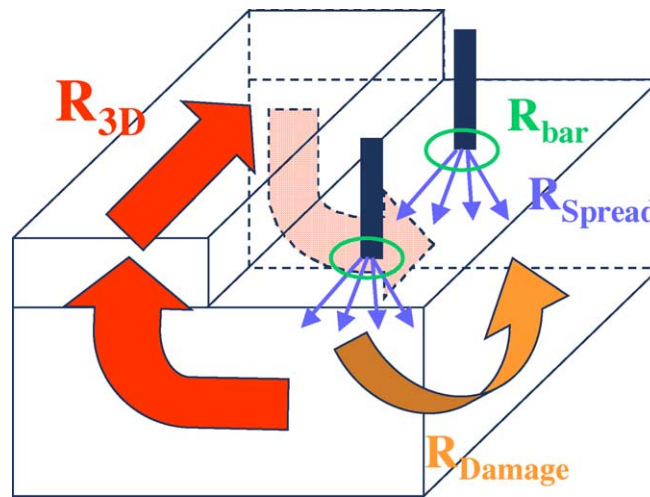


Fig. 28. In general, the total resistance between the two probes is composed of the contact and spreading resistance close to the contact in series with the parallel resistance of, on the one hand, the damage component and, on the other hand, the 3D lateral resistance component.

more conductive top layers. As such, the calculated resistance for the beveled structure, i.e.  $1.8 \text{ M}\Omega$ , is about four times smaller than the resistance from the flat structure, i.e.  $7.5 \text{ M}\Omega$ .

Further analysis of the available data reveals an even more remarkable observation, namely that the resistance decrease due to the lateral current flow is of approximately the same magnitude as the pre-bevel resistance increase at the same depth (geometric effect, surface states). For a given shallow structure, which clearly needs pre-bevel resistance increase correction at the bevel edge, the latter will obviously be applied, lowering the resistance to its value far away from the edge. For a second much thicker structure (identical with the first one for all depths available in the first one, relative to a common underlying isolating boundary), there will be no apparent need for pre-bevel resistance increase correction (as it is much thicker), and therefore the latter will not be applied. However, in

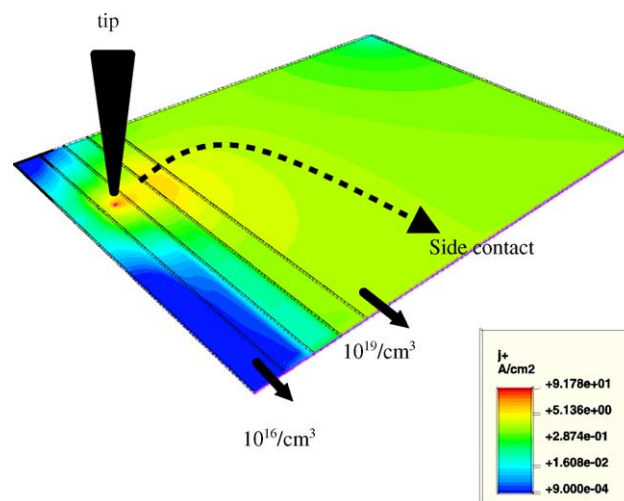


Fig. 29. Three-dimensional device simulation illustrating how current flows upwards through the more highly doped layers to reach a side contact.

principle, at the depth in the second structure, which corresponds to depth zero in the first one, there is certainly an identical resistance increase due to the geometric effect and surface damage (surface states). Therefore, the fact that we, in practice, do not correct for the latter on the second structure, implies that we are assuming automatically a resistance decrease of the same magnitude, which we now know is due to the lateral current flow phenomenon.

For completeness, it should be noted that only relatively little research has been done on this lateral current flow problem up to now. It has been proposed that the formulas describing the complete geometric bevel effect [47] mentioned earlier (in the pre-bevel resistance increase section) account intrinsically also for the here discussed lateral current flow problem and therefore are able to correct for it completely. As the 3D lateral flow component, similar to the pre-bevel resistance increase, can also be larger than a factor of two, this may need, however, some further consideration. Future work may prove that the lateral current and pre-bevel resistance increase component (when dominated by surface states) not always cancel out each other, in general, and may themselves need their own correction factor for silicon. Note that the latter has been found to be necessary, for other material types, such as metal films, as discussed further on.

#### 4.2.9. Qualification procedure

For any characterization technique, the issues of repeatability and reproducibility are crucial to its application. In the present context, repeatability (following the ISO 5725 standard [51]) is defined as the value below which the absolute difference between two single test results may be expected to lie with a probability of 95% when the accuracy tests are performed within a single laboratory in a short period of time. Reproducibility is defined similarly but for tests performed at different laboratories or over longer periods of time.

In 1995, a project entitled “Qualification of SRP operations” was launched under the auspices of the European Economic Commission (EEC) [52]. The main aim of the project was to develop a detailed written qualification procedure and a set of fully characterized samples, which could allow laboratories to independently evaluate and monitor the quality of their SRP operations. A target accuracy of 10% standard deviation was put forth as the final goal. The project included a large-scale international round robin involving 20 different participants and 22 different structures to be characterized. The latter included structures such as sub-micrometer epi-layers, various types of implants (well, source/drain,  $V_T$ -adjust) and bipolar related ones (transistors with a poly-crystalline emitter and narrow base and highly doped buried layers).

A detailed description of the initial and final results of this project can be found elsewhere [6–8]. A set of primary qualification parameters have been defined based on the round robin results and for each of these, quantitative specifications have been put forward as essential in order to achieve the target accuracy. Next, a set of electrically verifiable secondary qualification parameters together with a set of qualification samples has been introduced. The complete qualification procedure contains both the primary and secondary qualification specifications and a description of the qualification samples.

The final conclusion of this work was that the target accuracy of 10% (i.e. a reproducibility of 30%) can indeed be achieved for sub-micrometer structures provided the proposed qualification procedure is followed. The accuracy results on sheet resistance as obtained from SRP versus FPP values for a wide range of structures and laboratories are shown in Fig. 30. Note that the better laboratories (for example, round robin participant RR24) do achieve the target put forward.

Despite the fact that other dopant characterization techniques, and most notably SIMS, do achieve higher accuracies (better than 1%) and reproducibility, SRP remains nevertheless an attractive technique as it is widely applicable and gives intrinsically electrical information, which is not obtainable through other means (see Section 5).



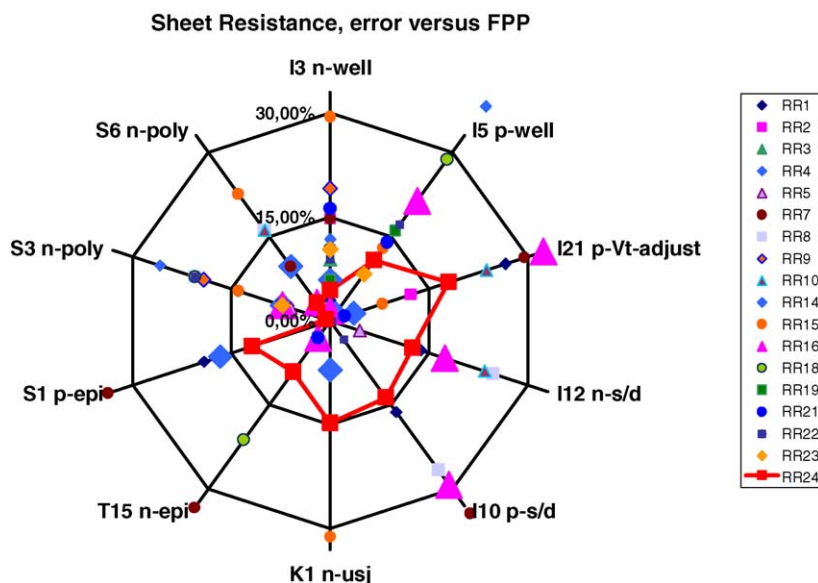


Fig. 30. Relative error of sheet resistance as obtained from SRP depth profiles vs. absolute FPP values. The relative error for one of the better laboratories is always within 15% irrespective of the type of structure, epi-layer, source/drain, well, ultra-shallow profile, poly-crystalline layer, etc.

#### 4.2.10. Summary

By taking into account all of the above issues, one can for a large range of structures extract quite accurate carrier depth profiles, with a good agreement with FPP sheet measurements, as illustrated in the upcoming applications section. In the late 1980s, however, it was recognized that there was also another large range of structures which had interfaces which were steep enough, for example, as those which can be grown by MBE, such that they could no longer be adequately treated by simple Laplace-based tools, because of the impact of carrier spilling (diffusion) leading to a significant carrier redistribution relative to the fixed dopant ion positions. This has given rise to a whole new branch of research which we discuss in the next section and has given us in many cases a whole new perspective on issues already touched on earlier in this review.

#### 4.3. Poisson-based modeling

Ultimately, in SRP, we are interested in the electrically active portion of the dopant profile, opposite to the total dopant profile as obtained from SIMS, as the former governs the actual device performance. However, in the 1980s, it has been recognized for the first time by Hu [53] that, for example, the presence of (need for) an (ideal flat) bevel surface by itself is sufficient to cause significant discrepancies between the apparent *on bevel* mobile carrier profile as directly probed by SRP and the underlying *internal* (or vertical, in-depth) mobile carrier profile of real interest to the end-users (Fig. 31). Furthermore, both of these carrier profiles are different from the active atomic (fixed ion) dopant profile. Note that in Laplace-based analysis, it is intrinsically assumed that these three profiles are always identical.

The discrepancy is related with the phenomenon of carrier redistribution near steep dopant transitions and/or adjacent lowly doped regions of opposite impurity type. Because initially it sometimes appeared, as (expected) carriers were lost (for example, in the tail section of implantation



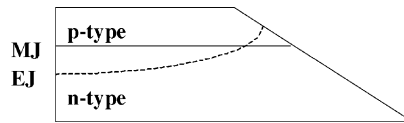


Fig. 31. Illustration of the impact of the presence of a bevel on the curved shape of the internal electrical junction (EJ) relative to the straight metallurgical junction (MJ) for a p-n structure. Note that, in practice, angles smaller than a few degrees are being used (not  $45^\circ$  as in the figure).

profiles), it was named the *carrier spilling phenomenon*. However, carrier diffusion would have been a better name.

#### 4.3.1. Experimental observations

For those who are not familiar with the carrier spilling phenomenon, let us first look at some examples to get a feeling for the magnitude of the problem and the kind of profiles that are affected.

The first examples to bring this problem dramatically to the foreground were different types of thin molecular beam epitaxially grown layers with very sharp interfaces [54]. For example, for a thin, medium doped, buried  $p^+$ -type layer (Fig. 32) on very lowly doped ( $p^-$ ) surrounding material, it can be seen that the apparent on bevel SRP carrier profile (as obtained from a Laplace-based calculation) sees a large amount of free carriers in the first 400 nm of the structure (before the doped layer), where no dopants are present. On the other hand, beyond the doped layer, one sees that, as expected, the SRP carrier profile drops quickly to the lowly doped substrate dopant level. Apparently, there is a significant difference between so-called forward (up-hill along the bevel) and backward (down-hill) on bevel carrier spilling. In the presence of a top layer of opposite type material, this effect becomes even more disastrous. As illustrated in Fig. 32, the apparent electrical on bevel junction is now located 400 nm closer to the surface than the metallurgical junction (at 800 nm).

The fact, that SRP sees large amounts of carriers where there should be none or of opposite type, may at first sight be surprising, but is a direct result of the non-localization of the mobile carriers relative to the fixed positions of the dopant atoms (trying to reduce the dopant gradient). Of course, their displacement relative to the ionized impurity atoms will cause an internal electrical field, counter acting this displacement. In equilibrium, carriers will be displaced over a distance proportional with the Debye length. Their equilibrium distribution can be found by solving the Poisson equation.

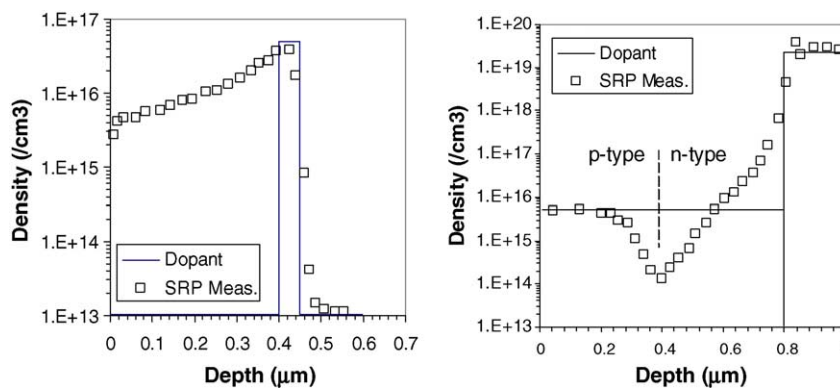


Fig. 32. MBE-grown structures showing the on bevel carrier profile vs. the dopant profile. (Left)  $p^- \cdot p^+ \cdot p^-$  structure; (right)  $p^+ \cdot n^+ \cdot p^-$  structure.

The real problem with understanding the measured on bevel epi-profiles was, however, that they are completely different in shape, i.e. they are asymmetric, relative to the internal (diffused) carrier profile as can be obtained by solving the one-dimensional Poisson equation starting from the dopant profile (as illustrated in the left part of Fig. 35 by the curve labeled “vertical”). Experiments on MBE-grown structures in a special upside down configuration resulted in exactly the opposite carrier spilling behavior [54], i.e. little spilling near the original surface and a lot of spilling towards the substrate. This proved that it was the presence of the bevel (and its orientation relative to the structure), which played a major role in the detailed understanding of the carrier spilling phenomenon as discussed in the next section.

One should not make the mistake to assume that the carrier spilling phenomenon is only limited to epi-layer structures. Structures where this phenomenon is at least as important, if not more, are implantation and diffusion profiles. As illustrated in Fig. 33, for a p-well implant, typically the backside of an SRP carrier profile drops faster (both on opposite and same type substrate), and has an apparent electrical junction (or interface) shallower than the corresponding dopant profile. Note that the apparent junction shift towards the surface is significantly larger in the presence of an insulating boundary. This apparent junction (or interface) shift has in the past sometimes been attributed erroneously to an inactive dopant tail.

Note that carrier spilling can sometimes have a quite surprising behavior. One might, for example, assume that carrier spilling will be negligible for very deep, slowly varying implantation profiles (and Laplace calculations will be correct). Nothing is, however, more from the truth. For deep well implants (as used in power transistors), differences in apparent electrical and metallurgical junction depth of several micrometers are no exception.

#### 4.3.2. The zero-field model

In the 1980s, it became clear, initially based on two-dimensional Poisson simulations, that the primary cause for asymmetric carrier spilling behavior in SRP is the need to use a bevel for the measurements [53], irrespective of how it is produced or its exact properties, i.e. its roughness, for example. Although the latter also plays a role, as will be discussed further on, it is the fact that inevitably material needs to be removed to make the bevel that is the primary cause. Therefore, in this

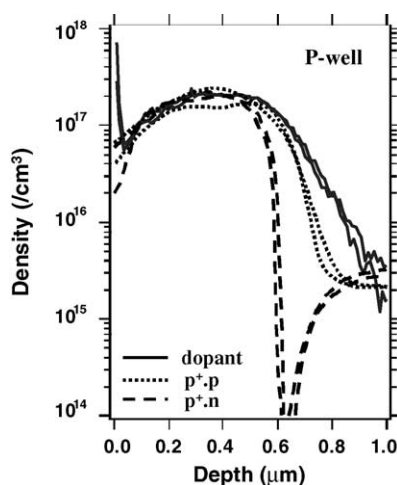


Fig. 33. SRP on bevel carrier profiles of the same dopant (single line) profile into same (dotted) and opposite (dashed) type substrate.

section, we assume for a moment that one can make an ideal, perfectly flat, electrically neutral bevel surface. Conversions based on that model were, however, problematic as their iterations then needed to include a full 2D Poisson solution at each iteration step.

In 1987, an important breakthrough was realized by Casel and Jorke [55], when they realized that for the small bevel angles, as routinely used in sub-micrometer SRP profiling, the solution of the two-dimensional Poisson equation could be simplified to a series of one-dimensional (1D) simulations, leading to a much shorter calculation time. This is achieved by considering the bevel as a gradual removal of parts of the dopant profile and solving the 1D Poisson equation for the remaining part of the dopant profile. For a perfect bevel surface, they imposed a zero value for the electrical field boundary condition at the bevel surface (and deep in the substrate). Hence, the name of the most widely used carrier spilling model, i.e. the zero-field model.

How the presence of the bevel exactly distorts the measurements is illustrated in more detail in Fig. 34 for an implantation profile. Other detailed explanations can be found elsewhere [55–57]. At each measurement point, SRP probes the resistance proportional to the internal, underlying, in-depth profile. At the bevel edge (making abstraction of other issues, such as the earlier mentioned surface damage problem), SRP will probe the internal electrical profile one obtains by solving the 1D Poisson equation, starting from the SIMS profile (assuming full activation for simplicity) and assuming zero-field boundary conditions. This internal electrical profile initially has an electrical junction deeper than the metallurgical one. As subsequent points are considered further down the bevel, for each one we have to re-solve the 1D Poisson equation, but now with an input dopant profile equal to the original SIMS profile from which the top portion (corresponding to our present depth) has been removed (beveled away). At first, for shallow depths, this makes little difference on the shape of the internal electrical profile. But, as one comes closer to the metallurgical junction (near the depletion region), and more and more of the highly doped material has been removed (by beveling) the electrical equilibrium starts to shift significantly. First, the peak carrier concentration at the surface will start to fall below the dopant level, and the internal electrical junction will start to move towards the surface, i.e. towards the metallurgical junction depth. At a given depth (dependent on the steepness of the dopant profile near the metallurgical junction), the internal electrical junction will always become shallower than the metallurgical one. Finally, it will reach the bevel surface, i.e. the on bevel electrical junction will be recorded, at a depth shallower than the metallurgical junction depth. Consequently, the on bevel (mobile) carrier profile typically has a much steeper descent rate near the junction than the (fixed ion) dopant profile, and a shallower junction than the metallurgical one.

Fig. 35 shows the simulation results with the zero-field model for the MBE structures discussed earlier illustrating a good qualitative agreement with the experimental data. Note the significant

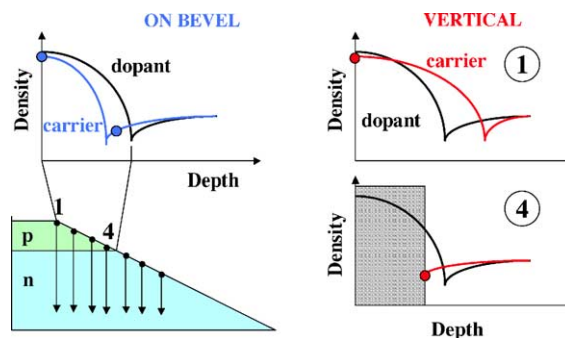


Fig. 34. Illustration of the relation between the SRP on bevel carrier, the vertical (or internal) carrier and the dopant profile.

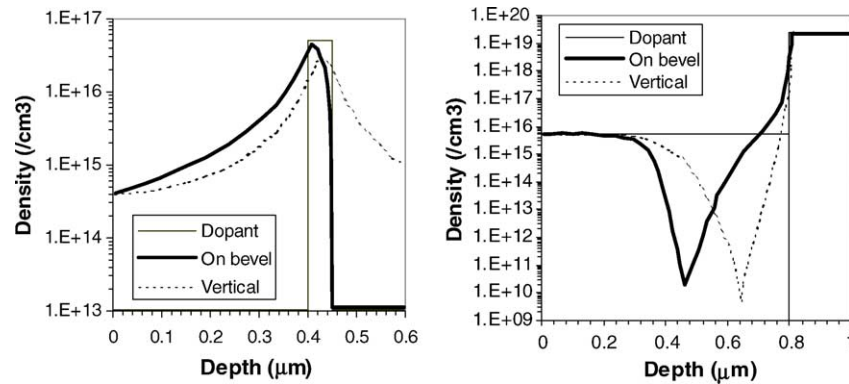


Fig. 35. Carrier spilling simulations with the zero-field model for the experimental MBE structures shown in Fig. 32.

differences between the shape of the on bevel and internal (vertical) carrier profile (at depth zero). It has been verified for a wide range of structures that their *qualitative* carrier spilling behavior can indeed be simulated satisfactorily through a series of one-dimensional Poisson solutions using the zero-field model boundary conditions.

#### 4.3.3. Need for physical modeling

After the initial success of the zero-field model, it became, however, rapidly clear that this model was unable to achieve *quantitative* agreement with experimental data, neither on MBE-grown layers nor on fully activated implantations [58], when using the corresponding SIMS dopant profiles as input for the Poisson simulations. Typically, a discrepancy in the apparent on bevel junction shift (i.e. difference between SRP on bevel electrical junction and metallurgical junction) of a factor of two up to four was observed between experimental and simulated data (see Fig. 36), the shift being the largest for the experimental data.

When trying to deconvolute the carrier spilling effects, using the zero-field model, this inevitably leads to the need to add lowly doped, exponential tails to the calculated dopant profile [57,59]. Unfortunately, there has never been any independent confirmation of the validity of this approach

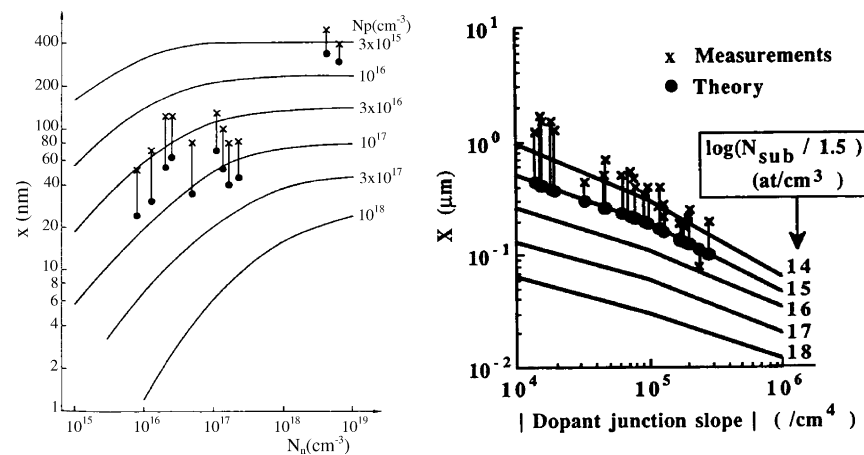


Fig. 36. Comparison of theoretical, zero-field (circles) and experimental (crosses) on bevel junction shift for (left) abrupt p-n epi-layers and (right) p-type implants in n-substrate.

through SIMS (or other) dopant profiling techniques. Moreover, the ubiquitous presence of this discrepancy on a very large dataset, which includes several MBE-grown samples, makes it highly unlikely that such a tail always should be present.

A more realistic assumption is that the boundary conditions used in the Poisson calculations with the presence of these tails, i.e. the zero-field model, are *over-simplistic* for an intrinsically complicated metal probe pressure contact on a rough beveled surface as used in SRP. Hence, there is a need for a more detailed understanding of all of the different physical processes, which occur beneath the probes during spreading resistance measurements. Once this understanding has been reached more realistic boundary conditions can be put forward.

Let us therefore start with a short historical review on physical contact modeling. In the early days of SRP, Keenan et al. [60] proposed a parallel circuit for the contact, consisting of an Ohmic (pure resistance) component, representing the plastically deformed portion of the contact (i.e. the total contribution of all the micro-contacts), and a non-linear component, representing the elastically deformed portion of the contact. Based on simulations of n-type calibration curves measured with tungsten carbide probes at 15 g load on  $\langle 111 \rangle$  material, Keenan et al. attributed the non-linear component to the presence of a surface state distribution with a density of  $5 \times 10^{11}$  states/eV/cm<sup>2</sup> and a neutral (zero) level of 0.2 eV above the top of the valence band. For p-type calibration curves, only a qualitative description was given.

Subsequently, Severin [61] proposed for the contact a parallel circuit of Ohmic components, where each component represented a single micro-contact. Eventual diode-controlled branches were discarded, based on the linear shape of Si and Ge calibration curves as measured with a steel tip at very high load of 200 g on  $\langle 111 \rangle$  material (30  $\mu\text{m}$  diameter macro-radius). Severin suggested that appreciable band gap compression was to be expected.

Next, Kramer et al. [62] presented an extensive study on the influence of temperature on spreading resistance measurements. Here, tungsten–ruthenium probes, at a load of 35 g on  $\langle 111 \rangle$  material, were used. Based on the variation of the spreading resistance over the temperature range 100–315 K for different homogeneously doped structures, a model was proposed with a non-linear component in series with the spreading resistance component. This non-linear component consisted of a parallel circuit of a thermal emission (Schottky) barrier and a tunneling component. The model fitted best the p-type results. Barrier heights of 0.32 and 0.25 eV were found for, respectively, p- and n-type high resistivity material. Assuming the interface Fermi level has in both cases the same energy relative to the band edges, it was concluded that the total band gap under the probes was only 0.57 eV, i.e. 0.54 eV lower than normal due to the presence of pressure. It was suggested that n-type material was the most sensitive to pressure variations.

Next, Marchand and Van Khiem [63] investigated more closely the impact of pressure on the shape of the current–voltage ( $I$ – $V$ ) curves for an SRP contact over the range from 20 to 100 g. Tungsten carbide needles were used on a p-type lowly doped sample. They basically considered the same modeling approach as Kramer et al., i.e. a non-linear diode component in series with the spreading resistance component. It was found that the real contact area was proportional with the load, leading to the conclusion that plastic deformations dominated the measurements. A local pressure of 63.4 kg/mm<sup>2</sup> ( $\sim 6$  GPa) was derived in agreement with the latter conclusion. The electrical behavior of the plastically deformed regions was best modeled by considering it as an elastic layer having many point defects distributed in space corresponding to the depletion region. A barrier height of 0.58 eV was derived.

Finally, Hillard et al. [64] modeled the  $I$ – $V$  curves as obtained from SRP point contacts and (low pressure) Hg gate contacts on p-type bulk material. A Frenkel–Poole model that accounts for tunneling through defects was found to fit the forward and reverse IV data best. An effective barrier height of 0.2–0.3 eV was reported.

The picture that emerges from the above work is one where two main aspects are important. On the one hand, the existence and impact of quite large pressures under the probes, leading to local plastic deformation at the micro-contacts and possibly band gap narrowing. On the other hand, the presence of a non-linear, Schottky-like behavior of the contact ( $I$ – $V$  curves) including tunneling behavior and possibly related with the presence of surface states.

In the subsequent sections, further progress on these two main issues will be reviewed. Note that up to now modeling focused on the shape of the calibration and  $I$ – $V$  curves. Recent progress in the SRP modeling has been triggered by, on the one hand, the availability of new experimental data relating to mechanical and electrical nano-indentation experiments in combination with a spreading resistance-based technique (namely scanning spreading resistance microscopy as discussed later) that uses a single, very small micro-contact (10 nm size) and, on the other hand, by the close monitoring of the carrier spilling behavior, i.e. the junction shift of the electrical versus the metallurgical junction, on well-calibrated junction-isolated structures.

#### 4.3.4. Impact of pressure

A simple calculation assuming a probe load of 5 g ( $\sim 50$  mN force) and a contact radius of 1  $\mu\text{m}$  leads to an approximate average SRP pressure of about 16 GPa. As we will see in a moment, these are quite high local pressures, which have a significant impact both on the mechanical and electrical properties of the silicon underneath the probes and therefore also on the carrier spilling problem.

The importance of pressure for the carrier spilling phenomenon is, for example, illustrated in Fig. 37. The apparent electrical junction depth of MBE-grown impatt structures, and hence the amount of carrier spilling (junction shift), is dramatically dependent on the probe load [65].

In order to better understand the impact of pressure on the intrinsically difficult SRP contact consisting of multiple extrusions, it is useful to first take a closer look at what indentation theory, in general, and recent experimental nano-indentation experiments (with specialized tools) on silicon (and germanium), in particular, can learn us on the mechanical and electrical behavior of single contact indentations with spherical indentors.

From general indentation theory [66,67], it is known that one can typically discriminate between the following three subsequent regimes as one increases the load on a spherical indenter. (1) Initially one enters the elastic regime where the Hertz classical theory is applicable. (2) As the pressure increases, the stress field under the contact will increase until at a certain depth along the axis of symmetry the local stress exceeds the uniaxial yield stress. This is the start of the elasto-plastic regime.

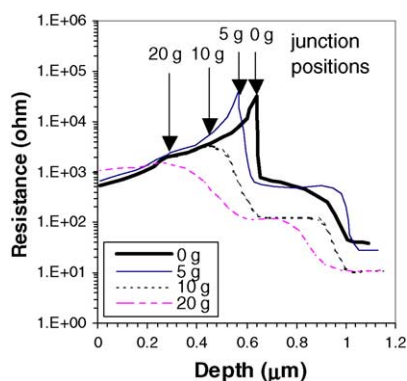


Fig. 37. Spreading resistance profiles of a single MBE-grown impatt ( $p^+ \cdot p \cdot n^+ \cdot n \cdot n^+$ ) structure measured with different probe loads vs. a zero-field simulation.



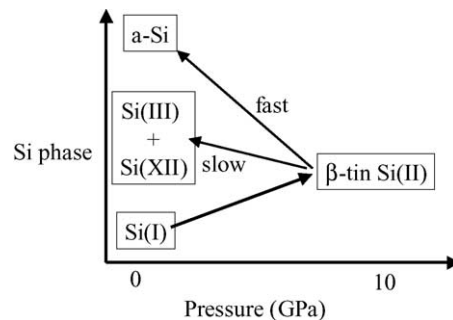


Fig. 38. Silicon phase changes upon loading and unloading of a spherical indenter.

(3) Finally, as the plastically deformed material reaches the surface, one enters the fully plastic regime. In this regime, the pressure flattens out over the contact area and an increase of pressure is compensated by an increase of the plastically deformed region. Formulas exist to determine the regime one operates in based on the material and geometric properties of the indenter and indented structure [68].

The situation for silicon is, however, additionally complicated by the fact that high-pressure experiments have shown that silicon (and also germanium [74]) undergoes phase transformations from the cubic structure Si(I) to the denser metallic  $\beta$ -tin structure Si(II) (22% volume reduction) at moderately elevated pressures [69]. The  $\beta$ -tin material is believed to be ductile (can easily flow) and has a low resistivity of about  $10^{-4} \Omega \text{ cm}$  [70]. The pressures needed to trigger the transformation depend on the nature of the stress state. Under pure hydrostatic conditions, the transformation takes place over the range 11.3–12.5 GPa, but this is reduced to values as low as 8 GPa when shear stresses are present (Fig. 38).

Upon slow release of the pressure, a reversion to another phase, i.e. Si(III), with a body-centered cubic structure has been reported [69]. This phase has a density intermediate between Si(I) and Si(II) with approximately an 8% reduction in volume over Si(I). This reverse transformation is proposed to occur at a pressure of 8.5–10.8 GPa. Alternatively, upon fast pressure release a reversion to amorphous silicon has been reported.

Evidence for the existence of the  $\beta$ -tin state under an indenter has been found through several approaches, such as the detailed study of load–unload force versus penetration curves for a spherical indenter, transmission electron microscopy (TEM) analysis, electrical resistance measurements on rectifying gold–chromium and epi-layer contacts, and the observation of material extrusions immediately adjacent to the indenter. Some of these studies are discussed into more detail further.

**4.3.4.1. Load–unload curves.** Load–unload force versus penetration curves as can be recorded with today's nano-indentation tools typically display discontinuities on loading (pop-in event) and unloading (pop-out event) when using spherical indentors (probe radius 4–8  $\mu\text{m}$ , contact radius about 1  $\mu\text{m}$ ) on silicon material with forces up to 100 mN (and penetrations up to 400–500 nm) [71,72].

A good agreement between simulations and experiments could be obtained over a load range from 70 up to 800 mN through the implementation of a Si(I) to Si(II) transition at 11.8 GPa (for the pop-in) and a unload Si(II) to Si(III) transition at approximately 8.3 GPa (for the pop-out) being in good agreement with earlier high-pressure results obtained mainly with pressure cells and not through indentation analysis [73].



Recently, a detailed study was made of spherical nano-indentation load curves at different maximum loads and load rates, in combination with Raman spectroscopy and XTEM analysis [72]. From this work, the following complex picture emerges. Below pop-in load (30 mN), the deformation behavior appears predominantly elastic. However, at such loads slip lines are observed by XTEM that appear to be nucleated at the depth of maximum stress (at about a depth equal to the contact radius). Beyond pop-in, a large volume of deformed material is observed, which extends beyond the maximum contact diameter. The extent of the slipped material, however, does not appear to change significantly after pop-in. Pop-in seems to occur when the volume of transformed Si(II) material just extends beyond the contact diameter. This allows catastrophic plastic deformation and Si(II) material flow. Fast unloading gave rise to amorphous silicon, while slow unloading resulted in a mixture of Si(III) and Si(XII) material as evidenced by Raman spectra.

Hence, although slip can be observed in intended silicon, the prime deformation process, which determines the hardness during room temperature indentation, is phase transformation. It is interesting to note that the indentation induced deformation for germanium, a semiconductor gaining rapidly interest for future technologies, appears to be due to a completely different process [74], i.e. twinning aligned along the  $\{111\}$  planes. Thus, unlike silicon, it appears that the hardness of germanium at room temperature, as measured by indentation, is not dominated by the initiation of a phase transformation.

*4.3.4.2. Electrical measurements.* Ultimately, one is interested in how indentation affects the conductance (local resistance) underneath a pressure contact. Experiments with triangular-shaped tips on and in-between gold–chromium contact pads between which the resistance could be measured have indicated that substantial resistance lowering occurs when the indenter crosses the metal–silicon interface [75]. It has been shown that this process is reversible. This behavior can be attributed to the creation of a  $\beta$ -tin phase transition under the indenter, which is expected to have metallic properties. Consequently, the metal–silicon interface is transformed from a rectifying Schottky towards an Ohmic-like contact during loading.

Recently, the resistance has been monitored in situ between a large Ohmic back-contact and large front Schottky contact (20 nm Al deposited on 7  $\mu\text{m}$ , 5  $\Omega\text{cm}$  epitaxial silicon, on highly doped silicon) while performing indentation experiments with a spherical indenter up to 100 mN loads (>500 nm penetration) [76]. Pop-in and pop-out were established at about 25 and 35 mN, respectively. Three phenomena could be highlighted.

First the electrical resistance starts to drop before the pop-in event. This indicates the presence of  $\beta$ -tin Si(II) material, but not yet in a sufficient amount to flow away along the sides of the indenter as required for the pop-in event (elasto-plastic regime).

Second, while maintaining the pressure constant over a few seconds, the resistance was not constant but increased. The latter is attributed to the immediate conversion of metallic  $\beta$ -tin Si(II) towards amorphous silicon as soon as the former (due to its ductile nature) is pushed out of the contact (fast pressure release).

Third, on pressure release, the resistance rises much faster towards its original (zero-pressure) value than expected (relative to its decrease during loading). The latter is attributed to the rapid initiation of a thin amorphous silicon interface between the original Si(I) and transformed Si(II) material upon initial pressure release, hence, leading to a fast deterioration of the electrical conductivity. Subsequently, dependent on the pressure release rate, either all Si(II) material is transformed to amorphous silicon (fast rate) or to Si(III)/Si(XII) material (slow rate).

To summarize, it is clear that at pressures around 10 GPa (dependent on the shear stress conditions and impact speed) a metallic,  $\beta$ -tin Si(II) phase forms, which lowers the contact resistance

drastically and therefore allows for an intimate (Ohmic-like) contact with the underlying silicon. As we further discuss, in the next section, it is this  $\beta$ -tin phase, which makes spreading resistance profiling actually possible. The presence of amorphous silicon after unloading can be considered proof of the presence of the  $\beta$ -tin phase during the loading (when fast unloading is the case).

#### 4.3.5. Pressure contact modeling

In the previous section, indentation experiments were discussed with quite large penetrations, i.e. with a penetration as deep (500 nm) as half the contact size (1  $\mu\text{m}$ ). In spreading resistance, however, one conditions the probes as to have only a 5–10 nm penetration for a similar 1  $\mu\text{m}$  contact radius. As already discussed, this is achieved by the creation of a multitude of small 10–50 nm micro-contacts.

Consequently, what happens beneath an SRP probe upon impact with the silicon material is somewhat different, but not completely dissimilar, to what has been discussed earlier. A fully conditioned probe has a surface from which multiple protrusions are sticking out. Upon impact with the silicon, these small protrusions (10–20 nm in size) will make first contact. Given the load of 5 g (for a qualified system) readily pressures above 10 GPa are locally present. These pressures are large enough to penetrate through the native silicon oxide and to trigger (as discussed earlier) locally a phase transformation from crystalline Si(I) towards body-centered tetragonal  $\beta$ -tin Si(II) [22,77], i.e. to create locally plastically deformed micro-contacts as shown in Fig. 13. Upon further impact, the plastically deformed material near the protrusions is pushed outward [78] until full contact has been established.

At that moment, three different pressure regions can be discerned as illustrated in Fig. 39. Namely, the plastically deformed  $\beta$ -tin Si(II) micro-contacts, the elastically deformed stressed Si (I) and in theory there may also exist a buried plastically deformed Si(II) region [22]. Each of these regions is now discussed into more detail.

##### 4.3.5.1. Metallic Si(II) regions

- (i) *The micro-contacts:* The presence of the  $\beta$ -tin phase in the plastically deformed micro-contacts has been investigated by plan view and cross-sectional transmission electron microscopy (TEM) [22] measurements (Fig. 40). The latter have identified the presence of amorphous silicon material at the micro-contacts after pressure release. In combination with the extrusion of material, being proof of its ductile nature under pressure, and the fast pressure release rates used in SRP (10 GPa/s), this leads to the conclusion that a  $\beta$ -tin phase is very likely present at the micro-contacts during SRP measurements. Also the shape of load–unload curves as studied with SRP probes [77] confirms this conclusion.

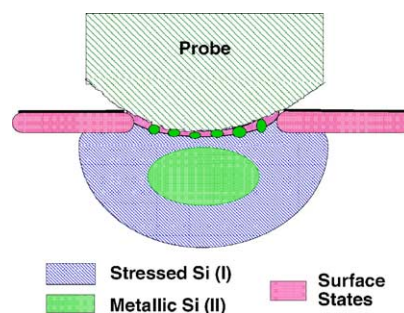


Fig. 39. Illustration of the physical SRP contact model.

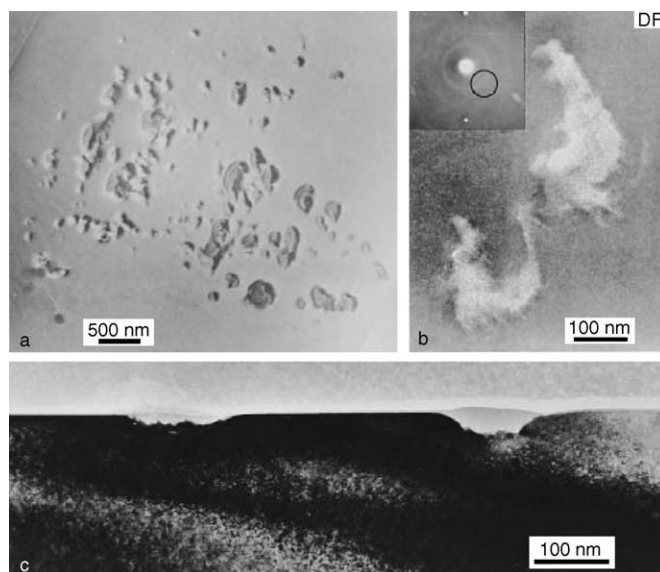


Fig. 40. TEM images: (a) plan view of an SRP imprint; (b) dark field image of a micro-contact and diffraction pattern (inset); (c) cross-section through two micro-contacts.

Measurements with single micro-contact SSRM (see also further), in which a very fine pressure control is possible, have shown that the presence of the  $\beta$ -tin phase is mandatory for making a reproducible contact with a low contact resistance [79]. Consequently, the main goal of probe conditioning in SRP is to create a sufficient number of such micro-contacts during probe contact.

The  $\beta$ -tin micro-contacts are surrounded by elastically stressed Si(I) material, to be discussed hereafter. Consequently, the current path at the micro-contacts flows from the metal (WOs) probes, through the metallic  $\beta$ -tin transformed micro-contacts towards the stressed Si(I) material and finally to the unstressed silicon. Hence, this is basically a metal<sub>1</sub> (probe)–metal<sub>2</sub> ( $\beta$ -tin)–semiconductor (stressed) contact, where each of the interfaces makes an intimate contact with the other one due to the ductility of the  $\beta$ -tin material. Eventual interface states (or native oxide) originally present on the bevel surface (before the  $\beta$ -tin transformation) are considered to have no impact on the current flow through the micro-contacts due to the metallic  $\beta$ -tin transformation.

Consequently, the  $I$ – $V$  behavior at the micro-contacts should be dominated by the metal<sub>2</sub> ( $\beta$ -tin)–semiconductor spherical interface within the silicon sample. This basically relates to a Schottky–Mott [39] contact (no surface states), for which the barrier height is dominated by the work function of the  $\beta$ -tin material. As such, the intrinsic micro-contact behavior will be the same for SRP and SSRM measurements, and hence the latter can be used to gather further information. It has been shown that  $I$ – $V$  curves measured with SSRM on fresh surfaces (with a minimal impact of surface states as discussed further on) can be satisfactorily modeled as a Schottky contact with a barrier height of 0.36 eV [80] when allowing for tunneling through a 10 nm thin interface layer.

The latter generates almost Ohmic  $I$ – $V$  curves for highly doped material as observed experimentally.

- (ii) *Buried metallic region*: General indentation theory predicts the presence of a plastically deformed, i.e.  $\beta$ -tin, buried region (Fig. 39) as on a macroscopic scale plastic deformation starts within the sample (not at the surface) [67]. The presence of such a buried metallic region could, however, up to now not be verified through cross-sectional TEM images taken after pressure release. This can either be due to the fact that at pressure release full re-crystallization occurs

when the small  $\beta$ -tin phase region is fully imbedded in crystalline material or either simply because it is not present at all.

Note that opposite to the earlier discussed indentation experiments in TEM-images of SRP imprints no slip lines have been seen.

**4.3.5.2. Stressed Si (I) region.** General indentation theory indicates that the depth of the stressed Si(I) region will be of the same size as the macro-radius of the contact. Note that for a qualified SRP system this is about a 1  $\mu\text{m}$ , while for an SSRM system this is only 5 nm. The contact at the surface with the probe is expected to be much less intimate and reproducible than in the micro-contacts case. In fact, for SRP at certain positions in between the micro-contacts there may even be virtually no contact (native oxide, air gap).

In this region, pressures of up to 4.4 GPa can occur. The impact of such pressure on the band gap, permittivity (dielectrical constant) and resistivity has been investigated [22]. It has been found that band gap narrowing up to 50% is to be expected (Fig. 41), and the intrinsic carrier level can increase up to  $10^{14}$  atoms/cm<sup>3</sup>. Up to 1 GPa, the permittivity (and resistivity) is not expected to change much. However, as from 8 GPa onward a dielectric catastrophe ( $\beta$ -tin formation) can occur, it is reasonable to expect a non-negligible increase of the permittivity above 1 GPa.

It is well known that silicon is a piezoresistive material, and it has been reported that the resistivity for n-type is more sensitive to this phenomenon than p-type material [22,81] (i.e. up to a factor of two change at 1 GPa for n-type [81]). It should be noted, however, that the applied piezoresistance tensor values have only been verified experimentally up to 0.3 GPa [82], and the original tensor data were for 10  $\Omega\text{ cm}$  material [83]. For more highly doped material, the components of the piezoresistance tensor are known to decrease significantly to only 20–30% of their original value [84]. One might expect therefore a non-linear behavior of the n-type calibration curves, but this is rarely observed. It is typically the p-type calibration curve, which displays a non-linear behavior. Furthermore, one can have (for n-type) simultaneously an increase and decrease of the resistivity dependent on the direction considered, hence, possibly canceling out the global effect. Consequently, the impact of piezoresistivity on SRP measurements is not completely clear at the moment and more work in this area might be useful.

In between the micro-contacts, the current flow will therefore be dominated by a metal<sub>1</sub> (probe)–semiconductor (stressed) interface. At this interface, the impact of surface states present on the beveled surface (see next section) may be reduced due to the smaller band gap, but not eliminated.

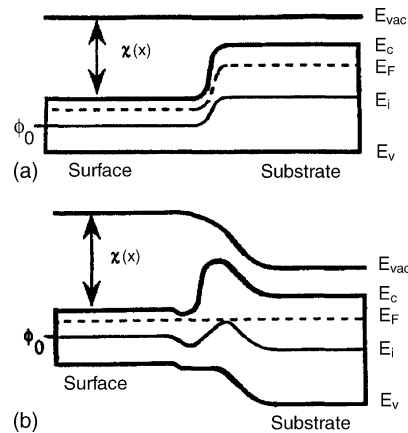


Fig. 41. Illustration of the impact of band gap narrowing for the n-asymmetric model on a n-type substrate, where it is assumed that the position of the top of the valence band remains virtually unaffected by the pressure.

Therefore, the current flow in between the micro-contacts may best be approached as a Schottky–Bardeen [39] contact (with surface states) for which tunneling is probably less likely to occur. Here, the barrier height will partially be determined by the probe work function and partially by the density and zero level of the surface states along the bevel surface.

#### 4.3.6. One-dimensional pressure simulations

It follows that the SRP contact can be considered as a parallel circuit of, on the one-hand, Schottky–Mott diodes (including tunneling) representing the micro-contacts (also referred to as the plastic component) and, on the other hand, Schottky–Bardeen diodes representing the region in between the micro-contacts (referred to as the elastic component). For low resistivity material, the plastic component is expected to dominate the circuit (lowest resistance) due to its Ohmic-like behavior (tunneling through barrier). For high resistivity material, the relative weight of both components will depend on their effective barrier height and contact area (Eq. (15)). Assuming similar barrier heights for both components, the elastic component is expected to dominate, as it typically relates to the largest area (smallest resistance). Oppositely, if the barrier height of the plastic component is smaller than for the elastic one, the plastic component may also prevail for high resistivity material. Experimentally, the former case has been reported for p-type material, and the latter for n-type material [22]

For the stressed Si(I) material modified values for the permittivity and band gap (intrinsic carrier level) need to be considered. The increase of the former gives rise to more carrier spilling (larger Debey lengths), as seen in practice, while the narrowing of the latter one reduces the peak resistance values as seen at junction cusps, again in agreement with practice. In between the micro-contacts, surface states need to be taken into account, to be discussed in the next section. This leads to the need for solving a generalized version of the Poisson equation as discussed in detail elsewhere [65]. As for the zero-field case, one starts from the known (SIMS) dopant profile ( $N(x)$ ) and first performs a series of one-dimensional generalized Poisson simulations (for each position along the bevel) where the surface states come into the bevel surface boundary conditions. Next, to allow comparison with the experimental resistance profile, each internal carrier profile ( $n(x)$ ) is converted to its corresponding internal resistivity profile ( $\rho(x)$ ) using the correct mobility's based on the dopant profile ( $\rho(x) = 1/(qn(x)\mu(N(x)))$ ) and subsequently the earlier discussed three-dimensional Schumann–Gardner multi-layer model is used to generate the simulated resistance profile. During the latter calculation typically no heuristic Laplace-based barrier resistance (as discussed before) is taken into account, as the shape of the internal resistivity profile already accounts for the presence of a barrier through the presence of surface states in the one-dimensional Poisson calculations.

Such one-dimensional simulations [65] (see Fig. 42) have shown that for particular structures (such as p-wells), it is possible to obtain a very good quantitative agreement between measured on bevel resistance profiles and simulated ones (from SIMS data), both with respect to the apparent on bevel electrical junction position, the resistance cusp height at the junction and the shape of the measured resistance profile behind the electrical junction. It should be noted that for the pressure parameters considered in these simulations the same enhanced forward on bevel carrier spilling behavior was obtained irrespective of whether a p-n or n-p structure was considered. However, in order to extrapolate the applied modeling parameters (dielectric constant, band gap narrowing) to a broader set of dopant profiles (with steeper slopes near the metallurgical junction) unrealistic parameter values, for example, for the depth range of the modified physical parameters were necessary.

Therefore, although pressure undoubtedly plays a role in the concise quantification of carrier spilling, other physical issues need also to be considered into more detail.

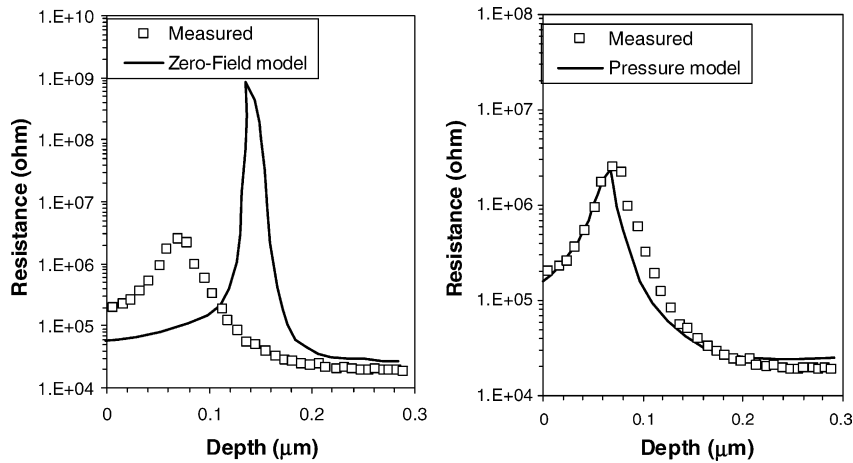


Fig. 42. Illustration of improved agreement with experimental raw data of the pressure model (right) vs. the zero-field model (left).

#### 4.3.7. Role of surface states

It is well known that an inevitable amount of surface states exists wherever the silicon matrix abruptly ends. In the processing of devices, continuous efforts are made to keep the levels of surface states at interfaces between different materials as low as possible (typically below  $10^{11}$  states/eV/cm<sup>2</sup> at mid-band gap [39]). Note that these are values for extremely flat (near-ideal) interfaces. In SRP, measurements are done on, in comparison, much rougher (mechanically polished) surfaces. Consequently, it is to be expected that significantly higher levels of surface states exist and may consequently affect the measurements themselves.

Experimental work involving the characterization of bevels obtained with different polishing procedures and subsequent low-pressure Hg-probe characterization have lead to values for the on bevel surface states density for state-of-the-art bevels of  $4 \times 10^{12}$  states/eV/cm<sup>2</sup> near the band edges [85].

Earlier, it was already indicated (in the Laplace-based modeling) that one needs to perform a surface damage correction for shallow structures. The size of these corrections for ultra-shallow (sub-50 nm) structures can be larger than one decade. Up to now, such large distortions can only be explained by the presence of surface states [48]. The surface states distribution required to obtain agreement between simulations and experimental data on p-n structures was around  $2 \times 10^{13}$  states/eV/cm<sup>2</sup> with a neutral position of 0.27 eV below mid-band gap. Note that in these simulations, not the precise shape of the surface distribution itself, but rather its induced surface charge for the structures considered was important. The same effect can be achieved with the distribution discussed hereafter.

Consequently, the presence of surface states can also be expected to have a non-negligible impact on the crucial carrier spilling phenomenon, especially near junction-isolated regions. Recently, this has been investigated in detail for a uniform density of  $5 \times 10^{12}$  states/eV/cm<sup>2</sup> of acceptor states above and donor states below a neutral level positioned at 0.28 eV above mid-band gap [86]. The most important conclusions of this work were as follows.

First, for medium ( $10^{16}$  atoms/cm<sup>3</sup>) and lowly ( $10^{14}$  atoms/cm<sup>3</sup>) doped p-type material, the assumed surface states distribution predicts a n-type inversion layer along the beveled surface (barrier height larger than 0.5 eV, up to 0.7 eV) as illustrated in Fig. 44a. The presence of the latter has been verified by SRP probe spacing experiments (see Section 4.4.3) on p-type  $8 \times 10^{14}$  atoms/cm<sup>3</sup> doped



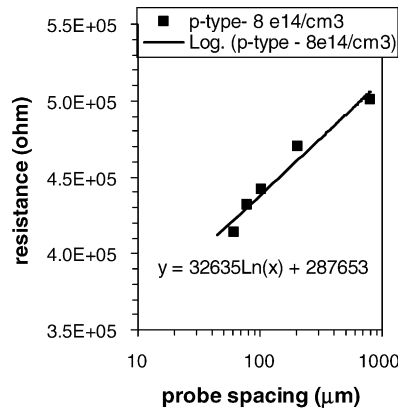


Fig. 43. SRP probe spacing experiment on beveled homogeneous  $8 \times 10^{14}$  atoms/cm<sup>3</sup> p-type doped sample. A sheet resistance value of more than  $1 \times 10^5 \Omega$  (slope regression line times  $\pi$ ) is found, indicative for the presence of a n-type inversion layer (substrate sheet resistance is about 200  $\Omega$ /square).

homogeneous samples as illustrated in Fig. 43. For the latter probe, spacing sheet values of  $10^5 \Omega$ /square have been measured opposite to the normally expected behavior as predicted by Eq. (2a), i.e. virtually no separation dependence for large enough separations (without surface states), implying that the measured spreading resistance values are dominated by the resistance of the inversion layer and not by the underlying substrate (of about 200  $\Omega$ /square). This remarkable result has been discussed in more detail elsewhere [86]. Note that the latter implies one needs to take care that calibration curves and unknown samples are measured at the same probe separation. The presence of such an inversion (or depletion) layer is in agreement with the experimental behavior of calibration data during different stages of the probe conditioning process. Furthermore, the fact that one observes for well-conditioned probes (i.e. with very low penetration), the highest noise levels for medium p-type material (shallowest inversion layer) and calibration slopes larger than one for p-type (no parallel conduction through n-type surface inversion layer and underlying p-type substrate) can be understood through this mechanism. For highly doped p-type and most n-type (except very lowly doped), in general, only depletion near the surface is expected, with a barrier height in the range 0–0.4 eV (dependent on type and dopant level) (Fig. 44b and c). Note that, in a first approximation, underneath the probes, due to the 50% band gap narrowing, the indicated barrier heights may also have to be divided by two, i.e. leading to barriers of 0.25–0.35 eV for p-type, and 0–0.2 eV for n-type, in reasonable agreement with most experimental data available.

Second, the different impact of the surface states distribution on different impurity types and their respective dopant levels causes an asymmetric effect on the electrical junction displacements along the

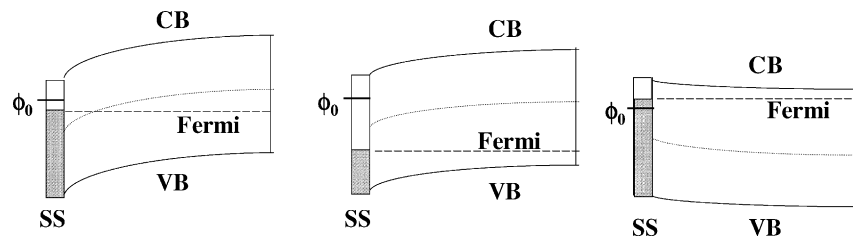


Fig. 44. Expected impact of surface states along beveled surface on bulk material: (a) n-type inversion layer for lowly and medium doped p-bulk; (b) depletion layer for highly doped p-bulk; (c) depletion layer for medium and highly doped n-bulk.  $\phi_0$  represents the surface states neutral level.



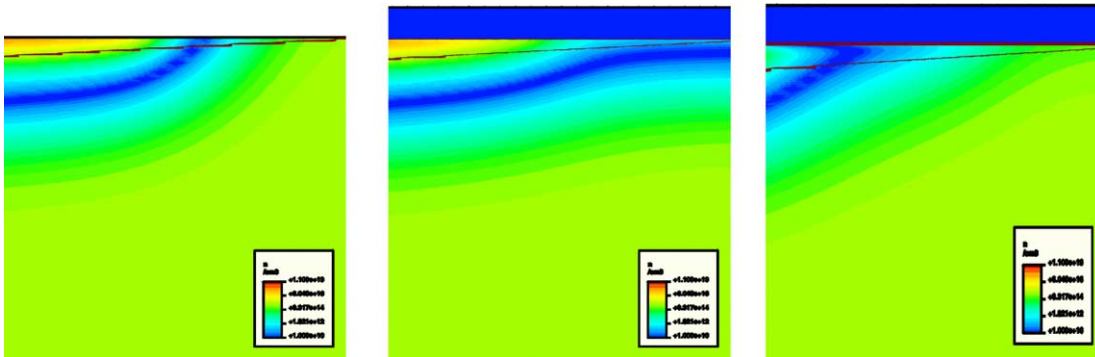


Fig. 45. Net carrier profile in the presence of surface states, along a bevel (at top of figures) with magnification  $20\times$ , between the lateral positions 5.25 and 6.25 mm. (Left) Zero-field (no surface states); (middle) n-p structure; (right) p-n structure. The 100 nm top oxide present in the two rightmost parts is necessary for defining the surface states during the simulations. The fine, slightly tilted straight line is the metallurgical junction. The dark gray curved band is the electrical junction.

bevel, relative to the metallurgical junction (opposite to the behavior obtained from pressure based calculations). For n-p structures, the apparent on bevel electrical junction displacements remain limited (i.e. close to the zero-field model, making abstraction of the pressure effect), while for p-n structures, there is a much more serious impact (see Fig. 45). Actually, if one compares the on bevel junction position for shallow, fully activated structures with the underlying dopant (SIMS) profile, one systematically observes (with a qualified SRP system) that the former corresponds in-depth with dopant levels near  $10^{18}$ – $10^{19}$  atoms/cm<sup>3</sup> (see Fig. 46). We refer to this level as the apparent SIMS depletion level, i.e. the SIMS concentration level (and depth), which based on SRP data seems to be completely depleted of carriers. Note that for the zero-field model, this depletion level (and depth) is much lower (and deeper), i.e. near  $10^{16}$ – $10^{17}$  atoms/cm<sup>3</sup>. The steeper structures become, the higher the depletion level (and the shallower the corresponding depth) will become because a fixed amount of charge has to be compensated to counteract the presence of the surface states. This behavior has been found to be in agreement with experimental comparisons of SRP and SIMS data for implantations with different steepness near the metallurgical junction and/or different thickness.

Third, the existence of a surface states distribution, as discussed earlier for SRP bevels, has been confirmed by experimental data as obtained from SSRM [80,87]. In SSRM, much smaller (10–20 nm

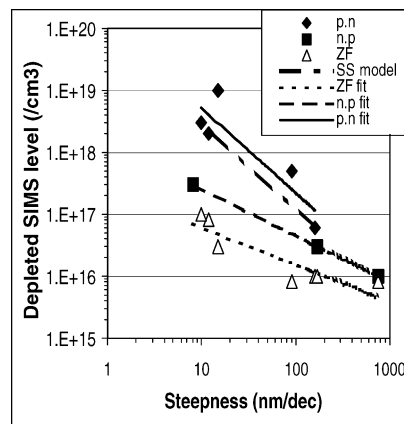


Fig. 46. Illustration of the relative impact of carrier spilling on the apparently depleted dopant level for different dopant slope steepnesses for, respectively, experimental n-p and p-n structures and as predicted by the zero-field and surface states models.

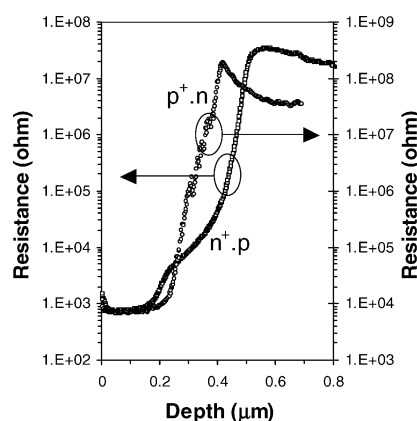


Fig. 47. SSRM raw data for  $p^+ \cdot n$  structure I10 (see also Fig. 57a) and  $n^+ \cdot p$  structure I12 (see also Fig. 57b.) Note that a clear junction cusp (one decade) is measured for the  $p^+ \cdot n$ , but not for the  $n^+ \cdot p$  structure at low bias due to the presence of a n-type inversion layer on lowly doped p-type material.

contact radius) highly doped, diamond-based tips are being used. It is systematically observed that for highly doped n-implants in lowly doped p-substrates, i.e.  $n^+ \cdot p$  structures, opposite to highly doped p-implants in lowly doped n-substrates, i.e.  $p^+ \cdot n$  ones, SSRM does *not* observe any junction cusp (sharp resistance peak) where the impurity transition occurs at low bias (0.1 V at the tip) operating conditions as illustrated in Fig. 47. At best, only a very slow rounded and gradual increase can be observed for  $n^+ \cdot p$ . However, as soon as the underlying layer (substrate) becomes more highly doped ( $10^{17}$  atoms/cm<sup>3</sup>), a clear and sharp junction cusp is observed (at low bias) irrespective of the involved impurity types [87]. The latter corresponds with the fact that for higher doping levels on p-type material, a p-type depletion layer replaces the n-type inversion layer. Furthermore, the limited dependence of the on bevel (or cross-sectional) electrical junction (or interface) shift on the applied SSRM bias is well predicted by the proposed surface states model [87]. Note that SRP always sees a junction cusp on silicon, irrespective of the involved impurities or concentration levels, probably due to the fact that its larger contact size and higher penetration make it less sensitive to these surface states induced junction-cusp artifacts than SSRM [88]. However, recently it has been found that SRP also displays an impurity dependent junction cusp behavior on germanium diodes [89] (i.e. a more pronounced cusp for  $n^+ \cdot p$  than  $p^+ \cdot n$  = opposite to SSRM behavior on silicon), strongly indicating that surface states may even be more important here than for silicon.

In summary, it follows that taking into account the impact of surface states greatly enhances our insight in many of the experimental issues crucial to the understanding of the SRP raw data, i.e. higher noise for p-type than for n-type, sensitivity of the slope of p-type calibration curves, severity of the impact of surface damage and magnitude and asymmetry of the carrier spilling behavior on well-calibrated junction-isolated structures. Especially with respect to the latter, it, however, also means that an adequate quantitative correction becomes more difficult because the accurate knowledge of the actual surface states density distribution is required.

#### 4.3.8. The three-dimensional physical model

Based on our present understanding of the carrier spilling phenomenon, the following physical issues are believed to play an important role:

1. *The bevel*: The presence of a bevel causes a significant asymmetric carrier diffusion behavior relative to the expected electrically active dopant profile. As it is a pure geometric effect, it is the

same for n-p and p-n structures. For arbitrary angles, it is a two-dimensional phenomenon. For small angles, it can be reduced to a series of one-dimensional simulations.

2. *Pressure*: Under the probes two different current paths are created. One path running through 5–15 nm deep, plastically deformed, metallic,  $\beta$ -tin micro-contacts, resulting in a Schottky–Mott type behavior, including tunneling through the barrier for highly doped material, i.e. displaying an Ohmic-like behavior. The other path running in between the micro-contacts through stressed Si(I) material having a band gap about 50% smaller than normal (and therefore with higher intrinsic carrier levels) and possibly an enhanced permittivity of a factor 10–100. A Schottky–Bardeen type of behavior is expected (surface states). The pressure distribution determination is basically a three-dimensional phenomenon. Pressure can, however, in a first approximation also be treated as a one-dimensional phenomenon (only downward direction). In that case, available pressure enhanced carrier spilling studies have in the past focused on the symmetry of the electrical on bevel junction shift, i.e. the same for n-p and p-n structures based on structures with moderate steepness at their metallurgical junctions. Dependent on the precise position of the narrowed band gap relative to the bulk one, however, also asymmetric behavior is feasible.
3. *Surface states*: Along the beveled surface, i.e. in between the probes (normal silicon band gap) and under the probes in between the micro-contacts (narrowed band gap), a non-negligible amount of surface states is expected to be active. Given a neutral level above mid-band gap, more carrier spilling is expected to occur for p-n than for n-p structures in agreement with experimental ultra-shallow junction behavior. The surface states behavior by itself is intrinsically a two-dimensional phenomenon along the bevel. In combination with local distortions of the pressure the whole problem becomes, however, three-dimensional.

Despite the progress made over the last decade in the area of SRP contact modeling, there is still important work to be done. First, given the significant impact surface states can have on SRP and SSRM measurements, more detailed experimental data are needed to characterize their distribution more precisely.

Furthermore, a definite quantitative verification of the above physical model taking into account all aspects of pressure and surface states requires an intrinsically difficult full three-dimensional approach. First, for a given detailed probe tip geometry, in agreement with a specific experimental setup, the corresponding elastically and plastically deformed areas and corresponding stress distributions need to be calculated. Next, these stress distributions need to be imported into an generalized electrical 3D Poisson device simulator in order to be able to compare simulated  $I$ – $V$  curves and resistance calibration data and depth profiles with experimental ones. In doing so, decisions will need to be made regarding the position of the stressed, narrowed band gap relative to the original unstressed one, the behavior of the surface states under high pressure, the precise behavior of the permittivity at pressures above 1 GPa, etc. Once such a full 3D understanding has been established, one can try to deduce a more simplified model, which can be implemented for the routine application of the carrier spilling phenomenon.

#### 4.3.9. Carrier spilling correction

As illustrated earlier, carrier spilling can distort the shape of the dopant profile one is interested in, i.e., in particular, its electrical junction position, and also its integrated dose (and sheet resistance) if sufficiently high concentrations levels (relative to the involved peak level) are affected. Dependent on the kind of structure, the application of a carrier spilling correction may therefore be mandatory to extract the correct information about the underlying electrically active part of the dopant profile.

The most simple approach is to start from a set of parameterized shapes (Gaussian, box, etc.) and to fit the available parameters (peak level, slope, etc.) through a series of forward simulations until one achieves a good quantitative agreement between the Poisson-simulated and experimental on bevel resistance profiles [57,91]. The former one is generated by a series of one-dimensional Poisson calculations (at each measurement depth) to determine the internal carrier profile corresponding with the chosen dopant shape, followed (after the conversion of the carriers into resistivity) by the application of the three-dimensional Schumann–Gardner model to simulate the corresponding resistances. The final results obviously will depend on the applied boundary conditions used in the Poisson solver. Quite useful qualitative information can already be obtained by the application of the simple zero-field boundary conditions. Recall that these results are semi-quantitative for n-p-based structures. One should, however, be aware that when trying to do a quantitative fitting on other structures, errors due to the fact that the zero-field model is too simplistic (no surface states or pressure taken into account), might end up as unwanted distortions on the fitted dopant profiles. The aforementioned exponential tails are a typical example of these kind of distortions. More elaborated boundary conditions can in principle be applied, but at this moment prove to be too difficult to calibrate and too time consuming to be used on a daily basis. Furthermore, as discussed earlier, in principle a full three-dimensional treatment of the problem is probably required for full quantitative agreement.

Ultimately, as for the Laplace-based case, one is interested in an automatic deconvolution of the underlying electrically active dopant profile from the measured raw resistance data, i.e. the inverse calculation. Leong et al. [90] has presented a first solution based on the method of regularization combined with zero-field boundary conditions. However, quite long calculation times of several hours were reported for this procedure.

Clarysse and Vandervorst [91] presented an alternative solution based on the backward reconstruction of the underlying profile, starting the calculation in the substrate, as is routinely done in Laplace-based calculations. For the zero-field based model, it is possible to do this today in a semiautomatic way on a routine basis, as the latter procedure only takes a few minutes. Because there is a numerical bifurcation point involved in these calculations, it is sometimes necessary for the operator to manually intervene in the calculations. Furthermore, the usage of the earlier introduced constrained cubic spline fitting technique is essential for the success of this deconvolution. Again, for quantitative deconvolution in all cases all information about the surface states density and pressure is in principle required, for which appropriate calibration procedures are not yet available. Furthermore, the more complex the Poisson boundary conditions become the more difficult (numerical instability) and time consuming the calculations are expected to be. Clearly, much more work in this area is needed to come to a reliable and easy to use carrier spilling correction tool.

Some practical illustrations of carrier spilling correction will be presented in Section 5.

#### 4.3.10. Summary

As more complex structures are being considered more sophisticated Poisson-based schemes are needed for the extraction of the underlying electrically active dopant profile which can be significantly different (shape, depth, dose) relative to the on bevel carrier depth profile as can be obtained through Laplace-based calculations. Issues which play a crucial role in this so-called carrier spilling phenomenon are the presence of the bevel (=zero-field model), the surface states along the bevel (polishing process) and the relative high pressures under the probes (reproducible contact). Zero-field corrections can today be performed in a relative straightforward and very fast way for simple (single) junction-isolated structures. They can be considered to give semi-quantitative information for n-p-based structures. For more complex structures (multiple junctions) and/or p-n structures, either

heuristic algorithms (as far as available) or time consuming and difficult to calibrate pressure and surface states related calculations are needed. Further work is therefore needed to improve on the latter situation.

#### 4.4. Sheet resistance

In order to achieve the envisaged state-of-the-art performance of future CMOS technologies ever-shallower junction-isolated source/drain and/or extension implants are needed with ever increasing concentration levels, as ultimately one is interested in achieving sheet resistances for these layers which are as low as possible. Hence, the crucial importance of being able to correctly measure the sheet resistance of a given, junction-isolated surface layer. The latter becomes intrinsically more difficult with the continuously decreasing depths of the junctions.

Today, different probe based techniques are available for doing so. In the next sections, we will compare the sheet resistance values as they can be obtained through a four-point probe measurement with those that can be extracted from SRP depth profiling and so-called probe-space experiments which are also based on the SRP technique.

##### 4.4.1. Four-point probe measurement

An in-line four-point probe system is well known to be an absolute measurement technique for the determination of the sheet resistance. A current is put through the outer two probes, while the generated voltage difference between the inner two probes is measured. In general, the measured FPP resistance  $Z(S)$  for an insulating layer with thickness  $d$  is dependent on the probe separation  $S$ . For shallow insulating layers, where  $d/S$  is much less than one, the influence of the separation becomes negligible and the FPP resistance  $Z$  relates to the sheet resistance  $R_{\text{sheet}}$  through the relation [92]:

$$R_{\text{sheet}} = \frac{\pi}{\ln(2)} Z \quad (20)$$

One should, however, keep in mind that most FPP systems work with relative highly probe loads, i.e. about 100 g. As such, there is for ultra-shallow (sub-100 nm) structures a risk of either punching through the junction or at least generating a non-negligible amount of leakage current. The danger is that one may think one is actually measuring the correct sheet values as the distorted values will be in the expected range (200–300  $\Omega/\text{square}$ ), but actually one is just measuring the substrate sheet value.

The impact of probe penetration has been discussed in detail in Clarysse et al. [43]. The sheet resistance of a series of sub-50 nm deep (at a level of  $10^{18}$  atoms/cm<sup>3</sup>) source/drain implants (with and without underlying well implant) was measured with three different techniques: a 20 g (SSM-240) and 100 g (Veeco 5000) FPP system and the 5 g SRP probe spacing technique as discussed in one of the next sections. Atomic force microscopy imaging of their imprints revealed, respectively, probe penetrations of 30, 130 and 5 nm. The whole set of data could only be explained consistently by realizing that the internal electrical junction will be penetrated significantly sooner than based on one-dimensional simulations far away from the penetrating contact, because of the impact of highly doped material removal at the penetrating probe location (Fig. 48a). The latter significantly bends up the internal electrical junction towards the surface and causes a junction punch through at depths comparable to the apparent electrical junction position of on bevel SRP carrier profiles (20–30 nm for the investigated structures), as the latter are dominated by the same material phenomenon (cf. the zero field carrier spilling phenomenon discussed before). When penetration occurs the size of

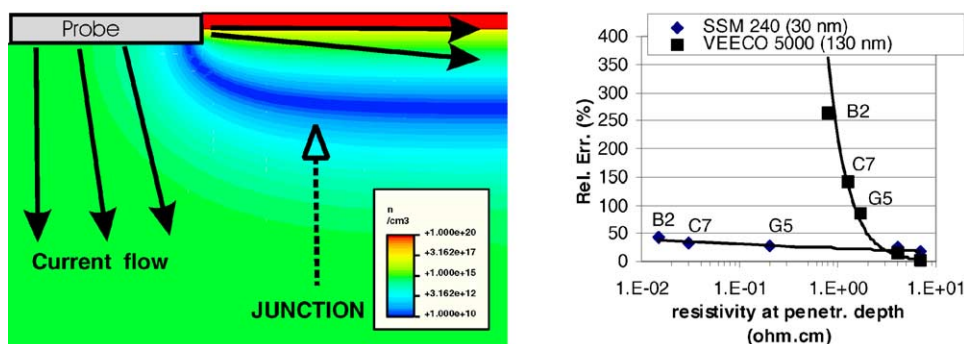


Fig. 48. (a) Two-dimensional device simulation illustrating the significant upward shift of the internal electrical junction (dark banded band) in the presence of penetration due to the impact of material removal. (b) Correlation of sheet resistance errors (relative to SRP-probe spacing) for 20 g (SSM-240) and 100 g (Veeco 5000) FPP measurements vs. the resistivity at the penetration depth.

the sheet resistance error could be correlated with the local resistivity at the penetration depth and the size of the contact (Fig. 48b).

It follows that either one needs to limit the probe weight or needs to ensure that punch through towards the substrate is impossible. The first can be accomplished either by using FPP systems with only 20 g load, or to use an SRP system as discussed further. The second can be achieved by a low dose deep implant, which will not influence the targeted sheet value, but will drive the shallow junction deeper into the substrate.

More recent data obtained on a series of ultra-shallow highly doped ( $10^{19}$ – $10^{20}$  atoms/ $\text{cm}^3$ ) CVD layers on opposite type substrate (Fig. 49) indicate that sheet resistance results between different techniques (20 and 100 g FPP and 5 g SRP probe spacing) start to diverge below 20 nm thickness. The FPP data typically converging towards the substrate sheet resistance value due to the short-circuiting of the substrate, and the low penetration probe spacing data converging towards unrealistic high sheet

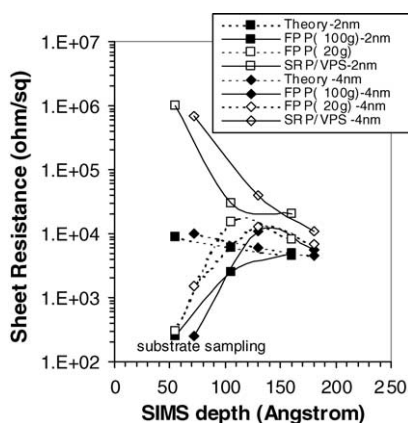


Fig. 49. Sheet resistance measurements of  $1 \times 10^{19}$  atoms/ $\text{cm}^3$  CVD layers with varying thickness (depth scale, depth at  $1 \times 10^{18}$  atoms/ $\text{cm}^3$ ) as measured by 20 and 100 g FPP and 5 g SRP probe spacing. The structures had either 2 or 4 nm undoped Si capping layer. Note that both sets of FPP data converge to the substrate sheet resistance value of  $200 \text{ } \Omega/\text{square}$  for decreasing thickness, while the SRP probe spacing rises to unrealistic high values. The expected theoretical values are also indicated for reference.



resistance values apparently affected by surface and/or contacting problems. It would therefore seem that none of the presently available pressurized probe systems is anymore able to characterize reliably the sheet resistance of sub-20 nm structures.

Alternative optical [93] (infrared spectroscopic ellipsometry) or non-contact systems [94] (frontier semiconductor measurements) exist which may alleviate this problem but are not discussed in this review.

#### 4.4.2. SRP depth profiling

Once an SRP depth profile has been calculated it is straightforward to determine from it the sheet resistance for any junction-isolated layer. As for a qualified system a probe penetration of only 5–10 nm is expected, the latter may prove to be more reliable than some high load FPP systems. The formula used in this case assumes a parallel conduction through all the sub-layers and is as follows, where  $\rho(x')$  is the resistivity depth profile:

$$R_{\text{sheet}} = \frac{1}{\int_0^x (1/\rho(x')) dx'} \quad (21)$$

It is clear that  $R_{\text{sheet}}$  will only be accurate provided all the effects discussed in Section 4 (correction factor, radius and barrier calibration, surface damage correction) are accurately implemented leading to the correct  $\rho(x')$  profile. Vice versa, Eq. (21) represents a valuable check on the accuracy of  $\rho(x')$ , provided a FPP sheet resistance value was obtained by an independent measurement.

An interesting alternative, i.e. SRP probe spacing, to obtain  $R_{\text{sheet}}$  exists, however, which is totally independent of any beveling, radius/barrier calibration or other correction scheme.

#### 4.4.3. SRP probe spacing experiment

During an SRP probe spacing experiment, the resistance on the original (unbeveled) surface is measured for five to seven different probe separations, ranging from the minimal value of 20–30 up to 1000  $\mu\text{m}$ . For each separation, 20–30 points are measured and their average and standard deviation are determined. Subsequently, the averaged resistance values are plotted against the Neperian logarithm of the separation. For a profile with a shallow insulating boundary, these points will lie on a straight line, the slope of which can be determined through a linear regression analysis. It has been verified both mathematically and experimentally that the sheet resistance for a junction-insulated layer can be obtained easily through the relation [92]:

$$R_{\text{sheet}} = \pi \frac{dR(S)}{d \ln(S)} \quad (22)$$

This is a direct consequence of the fact that two-probe and four-probe in-line resistances are always related to each other through [95]:

$$Z(S) = R(2S) - R(S) \quad (23)$$

as the spreading resistance increase with spacing solely reflects an increase in serial resistance proportional with the sheet resistance of the layer. Therefore, doing a probe spacing experiment is basically equivalent with doing an in-line four-probe point measurement.

The main advantages of an SRP probe spacing experiment relative to the FPP measurement are its absolute nature and its low probe penetration (5–10 nm) extending the applicability of sheet resistance measurements to shallower junctions. Furthermore, the linearity of the probe spacing curve gives an indication of the reliability of the measurement. If inadvertently a very leaky junction or non-junction-isolated layer is being measured, this will be reflected in a non-linear behavior of the probe spacing

curve. Disadvantages are that only small pieces (not whole wafers) can be measured, the fact that it is quite time consuming, the more limited availability of SRP relative to FPP tools and the absence of a wafer mapping capability.

It has been shown that for the specific case of a thin, junction-isolated, uniform layer, with resistivity  $\rho$  and thickness  $t$ , and therefore,  $R_{\text{sheet}} = \rho/t$ , the following relation holds [96]:

$$R_{\text{spreading}}(S) = \frac{R_{\text{sheet}}}{\pi} \ln \left( \frac{S}{a} \right)$$

where  $a$  is the contact radius. Provided Eq. (18) holds and assuming a negligible barrier component relative to the spreading resistance component (correction factor large for insulating layers), the latter equation implies that the intersection of probe spacing curves with the  $\ln(S)$ -axis correspond with the size of the electrical probe radius. This approach has as such been proposed as a possible calibration tool for the radius determination as discussed earlier. Some deviations from this behavior have been reported, implying that either Eq. (18) is not always valid or too simplistic (such as the presence of an important barrier) (see also Fig. 50).

For completeness, it should be noted that some anomalous behavior of probe spacing sheet resistance measurements have been encountered on CVD-grown structures (in addition to the earlier mentioned problems). The samples discussed in Fig. 51 and Table 3 consist out of a series of thin highly doped layers either with or without an additional thin lowly doped surface layer. The presence of an additional lowly doped surface layer should not influence the sheet value of the underlying highly doped layer (based on the shape of the SIMS profiles) and hence samples 4.1/4.4 and 4.2/4.5 should give identical sheet resistance values. The results in Table 3 indicate that with decreasing thickness of the doped layer, the SRP probe spacing experiments become more erroneous, although the latter are considered to be the more reliable ones given their minimal probe penetration (5 nm). On the contrary, techniques with higher loads (100 g) give results closer to the expected values despite their larger penetration (120 nm) relative to the internal electrical junction depth ( $\sim 600$  nm). Although the contact properties of the SRP contact should be irrelevant during a probe spacing experiment, as it is theoretically completely equivalent with a FPP measurement, the experimental behavior on these special CVD structures seems to indicate this is not always the case.

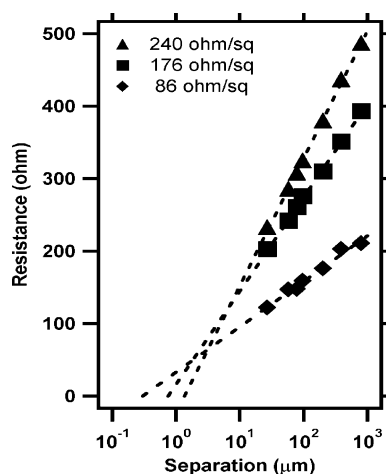


Fig. 50. Illustration of probe spacing experiments for different insulating layers. Note that they have different intersection with the separation axis, opposite to some theoretical predictions.

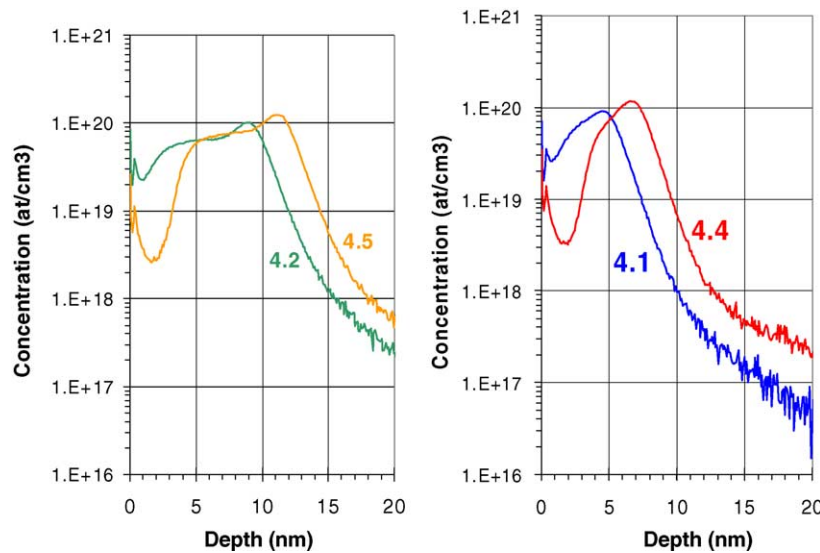


Fig. 51. Boron-doped CVD layers, with and without lowly doped surface layer.

Recent FPP data measured on metal films before and after etching (lower sheet resistance) revealed that FPP sheet values might also be affected by the quality of the probe contact (oxide interface layer). Further work is in progress to clarify the above issues [97].

## 5. Applications

The strength of qualified SRP is that it is able to characterize a wide variety of different structures, with a high dynamic range and good reproducibility within a short period of time and provide information on the electrically active dopant distribution opposite to SIMS which provides the total dopant distribution. Hereafter, we will briefly illustrate the capabilities of SRP for some widely used application areas, but also for some more exotic cases. Where possible, a comparison will be made

Table 3

Sheet resistance values for the CVD structures shown in Fig. 51, as measured by different techniques

	Sample	
	4.2	4.5
From SIMS (50% activation)	3196	2768 (−15%)
SSM-240 (20 g) FPP	4133	3184 (−29%)
PS (5 g) SRP	5279	4239 (−25%)
	Sample	
	4.1	4.4
From SIMS (50% activation)	5492	4772 (−15%)
SSM-240 (20 g) FPP	13020	6870 (−90%)
Veeco 5000 (100 g)	4850	5730 (+20%)
PS (5 g) SRP	47059	13062 (−260%)

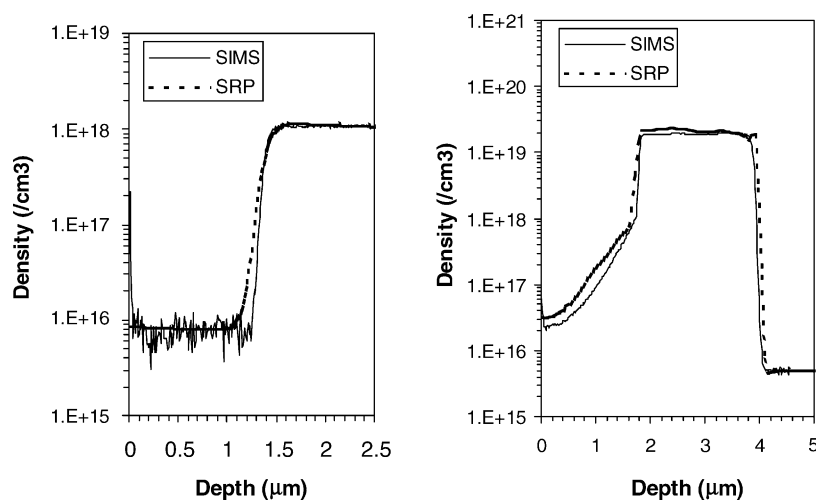


Fig. 52. SRP carrier and SIMS dopant profiles for p-p<sup>+</sup> and n-n<sup>+</sup>-p epi-layer structures.

with available SIMS dopant profiles and/or FPP sheet resistance values. The shown SRP carrier profiles were obtained with the Imecprof package [98] through Laplace-based calculations (including all discussed corrections) unless otherwise specified.

### 5.1. Epi-layers

Provided a qualified SRP system is being used, the measurement of micrometer deep epi-layers poses little problems. Fig. 52 shows two examples, one p-p<sup>+</sup> and one n-n<sup>+</sup>-p structure.

As can be seen a good overall quantitative agreement is obtained between the corresponding SRP and SIMS profiles. Recall, however, that achieving a good SRP accuracy at the (leading) low/high interface is critically dependent on the usage of well-calibrated radius and contact resistance values. If this interface is very steep, then a discrepancy between SRP and SIMS is to be expected (100–200 nm) due to carrier spilling (see p-p<sup>+</sup> example), i.e. the apparent leading interface steepness will be somewhat underestimated by SRP.

Also more complicated epi-layer structures can be measured. A typical example of such a structure is the earlier discussed staircase used for calibration curve extraction (Fig. 18). In Fig. 53, both the raw data (with smoothing) and the carrier (resistivity) are shown for the n-type case. Note that SRP is also able to nicely sense the slightly higher doped (factor 2–4) interface layers in between the actual calibration staircase layers. The smoothing is important for this type of structure. When using the recommended CCS algorithm discussed earlier (Section 3.3.6), about 10 different constraints need to be introduced. The latter takes somewhat more calculation time than routinely necessary for simpler structures, but the end result (flatness of each individual stair) is enhanced by the application of this smoothing scheme.

### 5.2. Well implants

Well implants play an important role in the operation of CMOS transistors. Fig. 54 shows a n- and p-type well implant in the same and opposite type substrate. The SRP versus SIMS agreement for the n-implant in n-substrate is excellent. Note, however, that for the p-implant in p-substrate one can already observe the onset of the impact of the carrier spilling phenomenon. Consequently, the tail

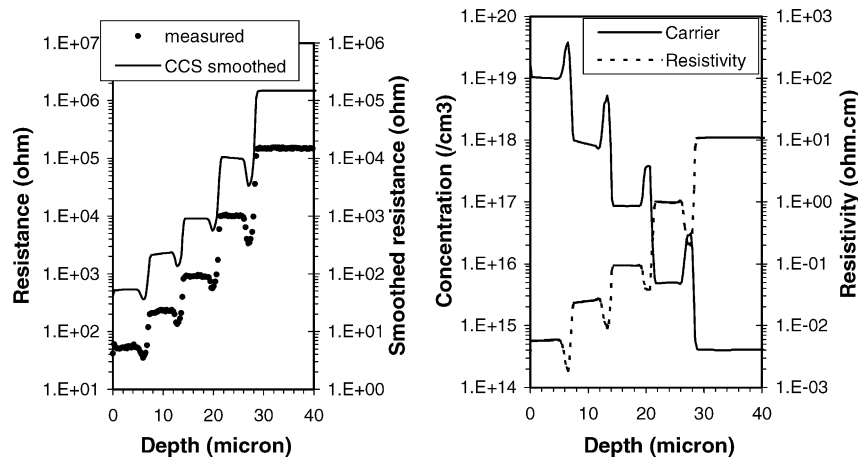


Fig. 53. Raw (and CCS smoothed) data and carrier (resistivity) SRP profile for n-type epi-layer staircase. The four calibration stairs (5  $\mu\text{m}$ ) are separated with higher doped (1  $\mu\text{m}$ ) interface layers.

portion of the SRP profile, below  $5 \times 10^{16}$  atoms/ $\text{cm}^3$ , drops faster than the actual dopant profile. For non-junction-isolated structures, the presence of this limited amount of carrier spilling will not influence the correctness of the integrated dose.

The situation changes somewhat when junction-isolated wells are considered. Both for the n- and p-well, the carrier profile now drops much steeper (and sooner) relative to both the actual dopant profile and the non-junction-isolated carrier profile. In fact, the impact of carrier spilling on the p-n structure has now become so large that errors on the dose (and sheet value) start to play a role. Hence, a carrier spilling correction is needed in the latter case. The result of a zero-field correction is therefore also shown in Fig. 54. The latter is, however, clearly not able to recover the correct dose value either. We come back to this issue in Section 5.4.

Keep in mind that for lower doping levels and less steep profiles (in the neighborhood of the junction) the bevel-induced carrier spilling will become more important. As such, the apparent on

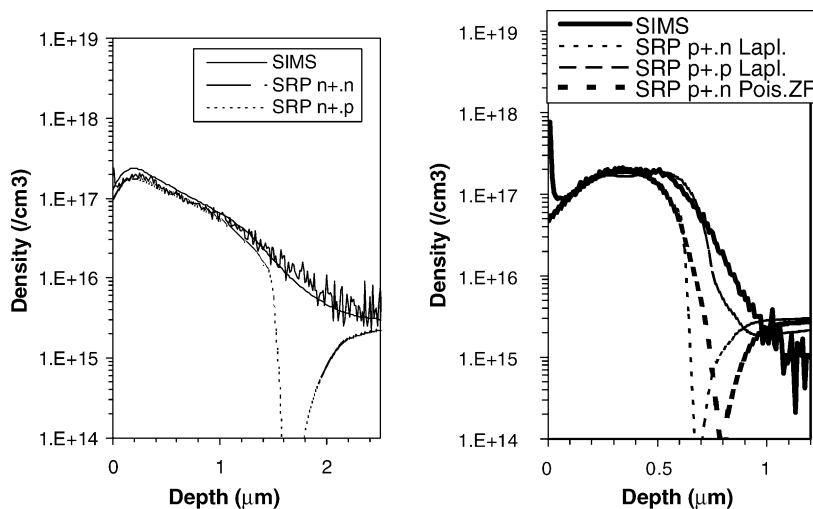


Fig. 54. The n-wells (left, P) and p-wells (right, B) in the same and opposite type substrate.

bevel electrical junction shift is for the n-p case (in Fig. 54) about 750 nm (moderate dopant slope near junction), while for the p-n case it is only 400 nm (steeper slope). For very slowly varying implant profiles, a carrier spilling induced junction (interface) shift of several micrometers has been encountered. Whether the carrier spilling induced electrical junction shift will or will not distort the dose and the sheet resistance results, depends on the size of the apparent absolute junction shift relative to the total depth scale involved.

### 5.3. Bipolar structures

Next, let us look at some results for bipolar related structures. Fig. 55 shows SRP versus SIMS profiles for a bipolar  $n^{++}\cdot p^{+}\cdot n\text{-p}$  transistor. Several issues need attention when interpreting such carrier profiles. First the carrier level of the top poly-crystalline (As) layer is underestimated due to the fact that SRP data deconvolution always uses crystalline Si mobility values in converting resistivity to carrier levels (Eq. (6)). Provided other mobility values are known these can, however, easily be incorporated.

Second, the width of the base region is underestimated due to carrier spilling. Note that the apparent junction shift is larger for the second (smaller dopant slope, lower levels) than for the first junction. However, also the first junction at concentrations levels of  $10^{18}$  atoms/cm<sup>3</sup> is not completely carrier spilling free. For even narrower bases than the one shown here (sub-100 nm), also the peak carrier levels will be underestimated. This is due to the fact that it is at this point (second layer of the structure) not possible to perform a complete pre-bevel resistance increase correction, although due to their shallowness this would actually be needed. The algorithm proposed by Dickey [47] can, however, be used to correct for the involved geometric bevel component.

In the collector region, as for the above well structures, one recognizes again a steep decent of the carrier profile towards the electrical junction long before the corresponding metallurgical junction has been reached. Note that an apparent junction shift of 1  $\mu\text{m}$  is observed here. In the presence of multiple junctions it is still quite difficult to perform automatic (zero-field or other) carrier spilling corrections. Hence, in such a case one will have to use carrier spilling simulation tools in order to interpret the SRP results in detail. Hence, it is fair to state that for this application SRP proves to be inadequate.

Fig. 56 shows a highly doped buried n-layer (As) with a lowly doped p-type layer (B) on top. In this case both the shape of the buried peak and the descending level of the top layer towards the surface

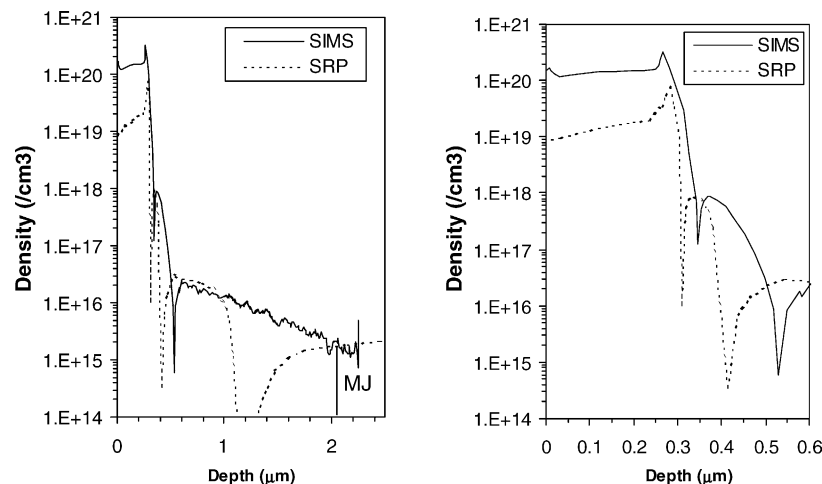


Fig. 55. SRP carrier and SIMS dopant profiles for a  $n^{++}\cdot p^{+}\cdot n\text{-p}$  bipolar transistor.



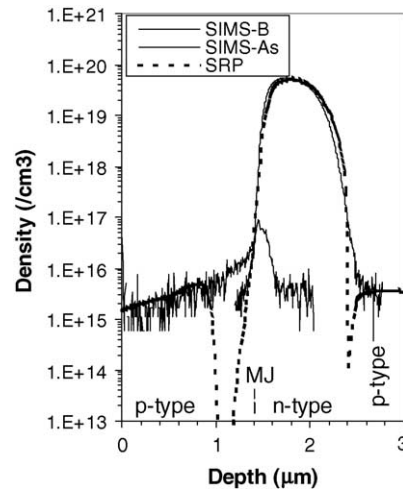


Fig. 56. SRP carrier and SIMS dopant profiles for a p-n-p buried layer.

are well resolved. However, the electrical junction is shifted towards the surface relative to the metallurgical junction by 300 nm again due to carrier spilling.

#### 5.4. Source/drain implants

Another category of important processes for CMOS technology is the source/drain and extension technology. Let us first take a look (Fig. 57) at a p- and n-source/drain implant in the sub-micrometer range. For such structures, there is in principle no problem for SRP to determine their profile shape above  $10^{18}$  atoms/cm<sup>3</sup> and hence to calculate the correct integrated dose and sheet resistance values.

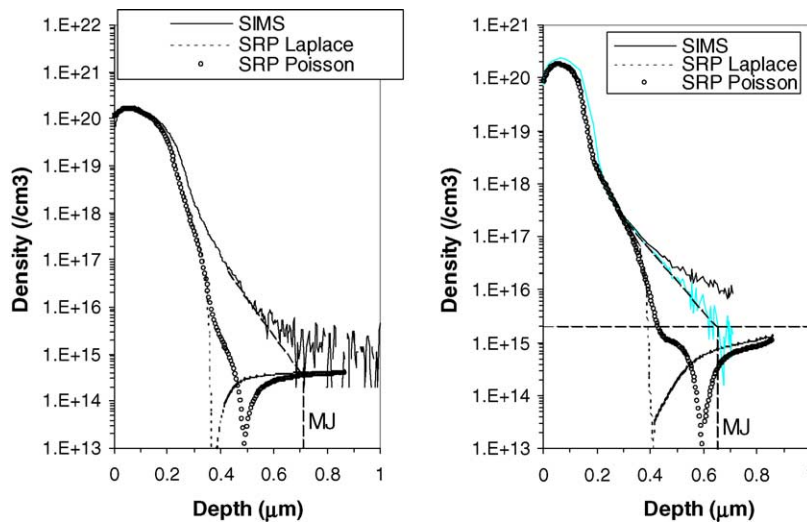


Fig. 57. SRP carrier (Laplace) and active dopant (Poisson-zero field) vs. SIMS dopant profiles for a (left) p-n (20 keV, B,  $4 \times 10^{15}$ /cm<sup>2</sup>, RTA 10 s, 1100 °C) and (right) n-p (120 keV, As,  $4 \times 10^{15}$ /cm<sup>2</sup> + 50 keV, P,  $6 \times 10^{13}$ /cm<sup>2</sup> with RTA 10 s, 1100 °C) sub-micrometer source/drain structure.

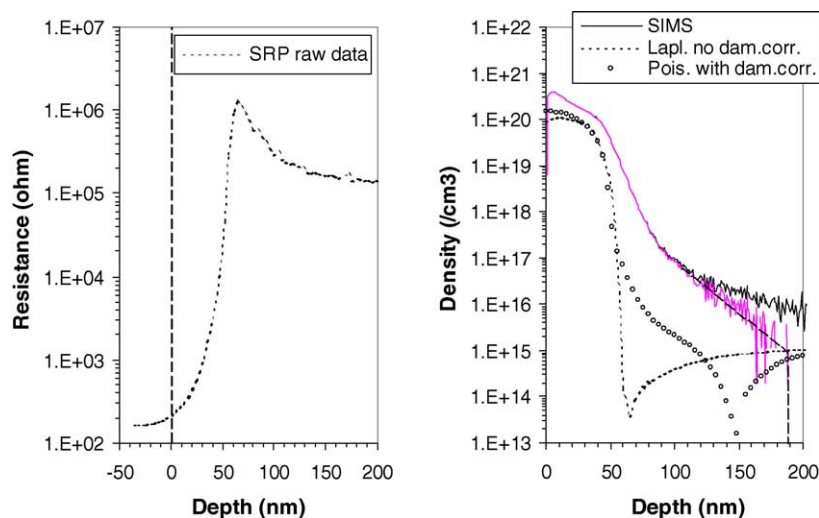


Fig. 58. (Left) Raw data and (right) SRP carrier (Laplace without surface damage correction) and SRP active dopant (Poisson with zero-field model and surface damage correction) vs. SIMS dopant profile for a sub-100 nm n-p source/drain structure (As,  $1 \times 10^{15}/\text{cm}^2$ ).

Although the absolute electrical junction shift towards the surface is in principle smaller for steeper dopant profiles, the relative impact of this shift is typically not negligible as the whole depth scale shrinks down as well. Hence, if one wishes to extract more accurate electrical junction positions, at least a zero-field carrier spilling should be implemented. The latter corrections are also shown in the indicated figure. Despite such a correction the SIMS profile cannot be fully recovered, although it has been fully activated. For the n-p structure, the active dopant junction (obtained from Poisson calculations) is rather close to the real metallurgical junction, but the tail shape of the profile is not high enough. For p-n structures, the situation is worse, neither the corrected junction depth, nor the tail of the profile come anyway close to the SIMS. It is believed by the authors that these discrepancies are mainly to our present deficiency to adequately correct for pressure and surface states related distortions.

Next, Fig. 58 shows an example of a shallow, 60 nm, n-type source/drain implant in p-type substrate. For this structure also, the raw data are shown. As the resistance clearly increases before the bevel edge (depth zero), the application of a pre-bevel resistance increase correction factor is mandatory. The measured FPP sheet value (with a 20 g load on the probes) was  $183 \Omega/\text{square}$ . Without pre-bevel resistance increase correction, the SRP-based sheet is  $224 \Omega/\text{square}$ , i.e. in error by 23%. However, with the latter correction this becomes  $174 \Omega/\text{square}$ , i.e. as close as 5% to the FPP value. A zero-field Poisson corrected profile is also shown. Note that the dopant junction is positioned about 90 nm deeper than the on bevel electrical junction, but that the profile remains unaffected above  $10^{18} \text{ atoms}/\text{cm}^3$ . It illustrates up to which point the original dopant profile can be recovered with zero-field Poisson corrections for such an n-p structure. The remaining discrepancy at a level of  $10^{19} \text{ atoms}/\text{cm}^3$  (relative to SIMS) is attributed to a combination of probe penetration, pressure effects and surface states.

Fig. 59 shows the SIMS and SRP profiles for the same p-n structure, after two different annealing steps. The SRP data were collected with a resolution of about 3 nm. Several points can be noted. First the difference in profile depth between both anneal conditions is similar for SRP and SIMS, i.e. SRP is able to resolve relative differences of 10 nm at a level of  $10^{18} \text{ atoms}/\text{cm}^3$  on 20–30 nm deep carrier profiles. Second the SRP surface carrier level for the first anneal condition is higher than for the second

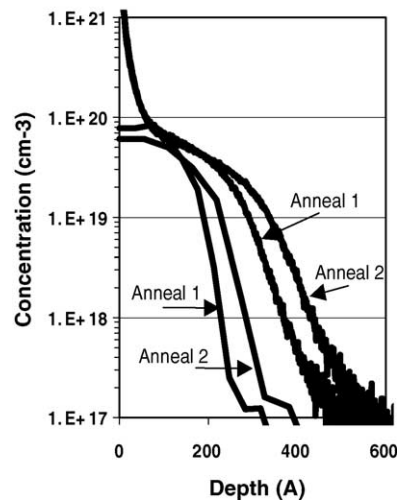


Fig. 59. SRP active dopant (zero-field) and SIMS dopant profiles for a low energy B implant in n-type crystalline Si for two different anneal conditions.

one. This is in agreement with the fact that the first anneal condition was performed at a higher temperature. Finally, one can observe that the SRP profiles are (again) systematically shallower than the corresponding SIMS profiles by about 10–15 nm at a level of  $10^{18}$  atoms/cm<sup>3</sup>. Similar SRP–SIMS depth differences have been observed over a larger set of profiles (with different total depths, see also Fig. 50) indicating that this difference is probably due to a combination of probe penetration and carrier spilling (pressure, surface states). The SRP profiles shown have already been corrected for zero-field carrier spilling. At a level of  $10^{18}$  atoms/cm<sup>3</sup> the carrier profile is shifted deeper by this zero-field correction by only 3–5 nm. Hence, there remains a need to improve the capabilities of our present zero-field based routine carrier spilling correction schemes.

Fig. 60 shows the same p-type implant in n-type crystalline silicon and in material pre-amorphized with germanium. If one considers only the Laplace-based profiles (not shown), which

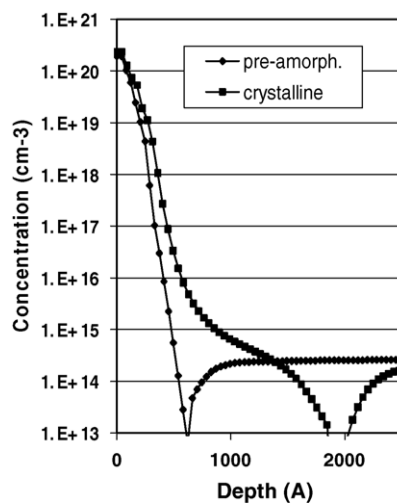


Fig. 60. SRP Poisson-based carrier profiles for the same low energy B implant into pre-amorphized and crystalline Si material. The different tail behavior would not be detectable with SIMS.

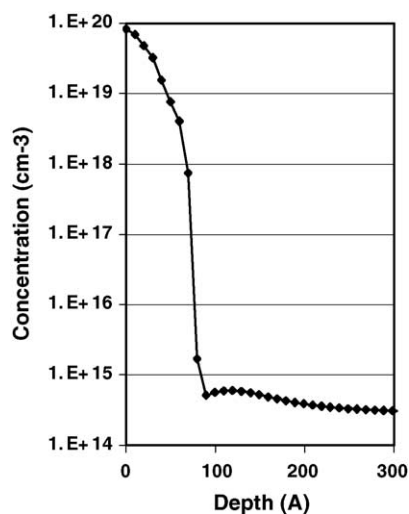


Fig. 61. High resolution SRP carrier depth profile of p-n structures (1 nm geometrical resolution). SRP sheet resistance is 4980  $\Omega$ /square. FPP is 5221  $\Omega$ /square. Electrical junction at 89 Å.

do not account for the phenomenon of carrier spilling (diffusion), then both profiles are quite similar, except in the tail section (beyond the junction). However, after a Poisson correction (for carrier spilling), we clearly observe a difference in the electrical junction position between both profiles of more than 100 nm. Note that this difference in junction position cannot be deduced from the corresponding SIMS data, due to their limited dynamic range. The fact that the implant in crystalline material has a significantly deeper electrical junction is in agreement with the fact that the implanted impurity element (boron) is expected to channel deeper into the silicon in the absence of any pre-amorphization.

Finally, Fig. 61 shows a high resolution SRP measurement of a boron implant. The depth resolution obtained here was 1 nm. The profile was measured after removal of a sacrificial oxide-capping layer, with optimized smoothing and a depth-dependent surface damage correction. On the one hand, this illustrates that SRP can resolve 10 nm deep steep state-of-the-art source/drain profiles. On the other hand, despite the fact that a quite good sheet resistance agreement with FFP could be established, there are only 10 data points (which is a bare minimum) and there is some doubt on the precise quantitative agreement with the real underlying profile, given the results as illustrated in Fig. 59 (see also Section 6.1).

Further examples on ultra-shallow source/drain structures are to be found elsewhere [99,46].

### 5.5. Ultra-shallow CVD profiles

For future CMOS technologies, ever-shallower structures are needed with ever-higher concentration levels to keep the sheet resistance at an acceptable level. Consequently, also the dopant slopes are getting steeper. As such, it is interesting to consider the performance of SRP on a series of constantly doped ( $10^{20}$  atoms/cm<sup>3</sup>) CVD-grown layers with a thickness ranging from 10 up to 90 nm. The main issue here is whether SRP is able to resolve the steep dopant slopes for these near-ideal box profiles and sense the small differences in junction depth.

A comparison of the SRP carrier and SIMS dopant profiles as shown in Fig. 62 illustrates that SRP is, in general, doing quite well in resolving the dopant slopes of about 1–2 nm/decade. Basically, this is because this is one of the few situations where carrier spilling is actually working in favor of the

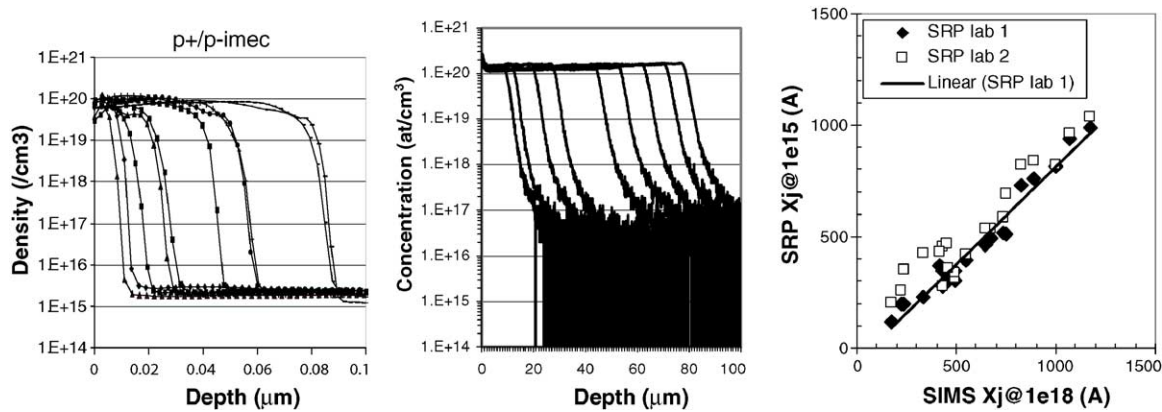


Fig. 62. Comparison of (a) SRP carrier and (b) SIMS dopant profiles for a series of box-like boron-doped CVD-grown structures with a steepness of 1–2 nm/decade. (c) Correlation junction depth ( $X_j$ ) extracted from SIMS profile at  $10^{18}$  atoms/cm<sup>3</sup> and SRP profile at  $10^{15}$  atoms/cm<sup>3</sup>. The SRP data originate from two different laboratories.

technique. Recall the asymmetric carrier spilling behavior as discussed in relation with Fig. 32. Here, we are interested in the backside of the profile, which can best be resolved by SRP. Fig. 62c provides a correlation between the junction depth of SIMS (taken at  $10^{18}$  atoms/cm<sup>3</sup>) and SRP (taken at  $10^{15}$  atoms/cm<sup>3</sup>). The small standard deviation of lab 1 (2–3 nm) illustrates that an excellent accuracy can be obtained with SRP.

Fig. 63 illustrates a more detailed comparison of one of the shallower profiles, namely the 15 nm thick one. Besides the good agreement of the carrier and dopant slope one can also observe the SRP peak concentration level is a factor of two lower than the SIMS dopant level. This is in agreement with independent FPP and SRP probe spacing measurements of the same layers (on opposite type substrate), i.e. the CVD layers were only activated to about 50%. The rounding in the near surface region for SRP, is probably an example of an SRP deficiency (bevel rounding, surface damage correction, etc.) as there is no obvious reason why the activation of these layers should be less at the near surface. Note also that a small error in the start point definition (for example, two points) would lead, in the present depth resolution (3 nm), to a 6 nm total depth error or a 30% relative depth error, illustrating the critical aspect of the starting point choice for such shallow structures.

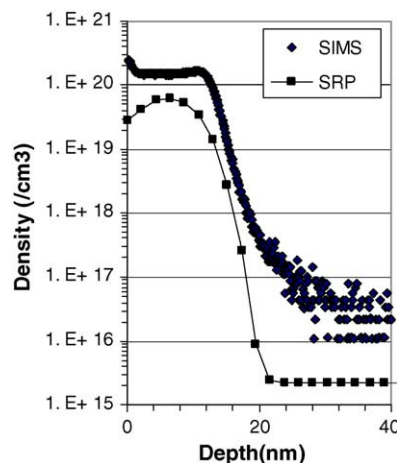


Fig. 63. SRP carrier vs. SIMS dopant profile for a 15 nm deep CVD-grown box profile.

### 5.6. Multi-layer structures

In principle, SRP has a geometrical depth resolution of better than 1 nm. However, obviously its electrical depth resolution is less as probe penetration, surface bevel roughness and carrier spilling limit it. One can get a clearer idea about the electrical resolution of SRP by measuring a series of closely spaced, alternating highly and lowly doped silicon layers with varying thickness and peak carrier concentration.

In a study where MBE-grown Sb layers were used with high/low levels of, respectively,  $10^{18}$  and  $10^{16}$  atoms/cm<sup>3</sup>, it was found that the thinnest superlattices which could be resolved adequately were 100 nm thick alternating high/low layers [100].

More recently, boron spikes either with constant peak dopant level ( $10^{19}$  atoms/cm<sup>3</sup>) and an increasing number of doped monolayers (4, 8, 24, 80) (sample #345) or with varying peak dopant levels (all 24 monolayers thick) (sample #358) have been studied [101]. The peak separations are in both cases 100 nm. Fig. 64 shows a comparison of the obtained SRP carrier versus SIMS dopant profiles. The latter have been measured, respectively, with a Cameca (#345) and an Atomika (#358) tool. Clearly, SRP is able to resolve in both cases the presence of all the boron spikes, irrespective of their thickness or peak dopant level. As expected, carrier spilling dominates the shape of the SRP peaks. Consequently, the SRP peak carrier levels are lower than the corresponding SIMS peak dopant levels and the leading edge of the peaks is considerably less steep in SRP than in SIMS. Note, however, that the trailing edge of the SRP peaks is, in general, very well resolved and in most cases has a comparable depth resolution as SIMS.

### 5.7. SPE regrown layers

Recently, there has been a renewed interest [102] in taking advantage of the high levels of activation achieved at low temperature by regrowth of a doped amorphous region as the out-diffusion of dopants is very small under these circumstances and thus ultra-shallow low sheet resistance layers can be obtained. Basically, the SPER process uses an amorphizing implant (often using Ge) creating a shallow amorphous Si–crystalline Si interface. Due to the low temperature regrowth, only dopants within the amorphous layer are activated and the amorphous depth will set the junction depth. After regrowth (600 °C, 1 min), the SRP profile (Fig. 65) shows a junction of 22 nm coincident with the

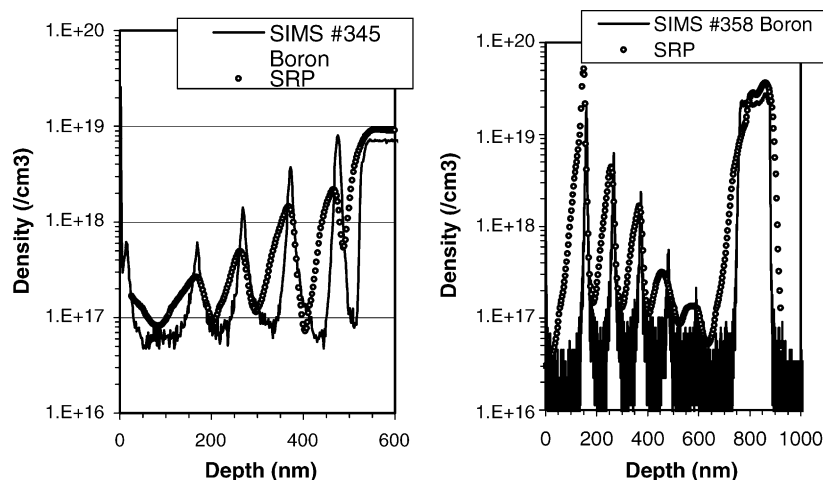


Fig. 64. SIMS and SRP profiles for a series of B spikes with 100 nm separation and different peak concentration levels.



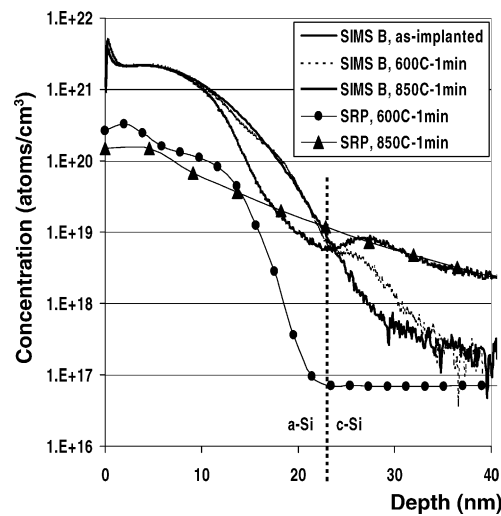


Fig. 65. Illustration of impact of 600 and 850 °C post-anneal on SRP carrier vs. SIMS dopant profile for SPE regrown layers.

amorphous depth (as determined with Rutherford backscattering spectrometry). Note the large inactive Boron fraction in the tail region (comparing SIMS versus SRP). An additional anneal at 800 °C for 1 min, leads to an increased activation beyond this interface as well as extra out-diffusion [103]. Furthermore, a lowering of the peak carrier concentration is observed in SRP, which can be attributed to a deactivation of dopants in that region.

### 5.8. As-implanted structures

Up to now, all examples related to annealed structures, as this is the primary application area of SRP. However, several authors have also reported SRP work on as-implanted structures [104,105].

After implantation, the apparent electrical concentration level of the originally perfect crystalline substrate may be affected either by locally reduced mobility in the presence of clusters of interstitial dopant atoms or by carrier trapping by the presence of point or extended defects. Both of these phenomena lead to a variation of the measured spreading resistance provided a sufficient number of carriers are affected. As such, SRP can, under certain conditions, successfully be applied to extract, for example, defect related information. This is nicely illustrated in [105], where a good agreement in defect distribution was established based on SRP and DLTS results.

### 5.9. Two-dimensional profiling

Given the success of SRP to probe one-dimensional depth profiles with nm-resolution simply due to one appropriate magnification angle, one may wonder whether it is not possible to do something similar to probe lateral carrier profiles under a mask with similar resolution. In the 1990s, before the advent of high-resolution 2D carrier profiling tools, such as SSRM or scanning capacitance microscopy (SCM), several papers have been published towards the usage of SRP for the determination of the lateral diffusion extent at different depths, i.e. the determination of lateral diffusion contour lines. All details can be found elsewhere [106–109]. Here, we briefly summarize the basic ideas underlying this approach and the accuracy one may expect from it.

For two-dimensional SRP profiling to work, one needs special test structures consisting of long doped stripes. Typically, oxide stripes of 10 μm width were used with implanted regions in between.

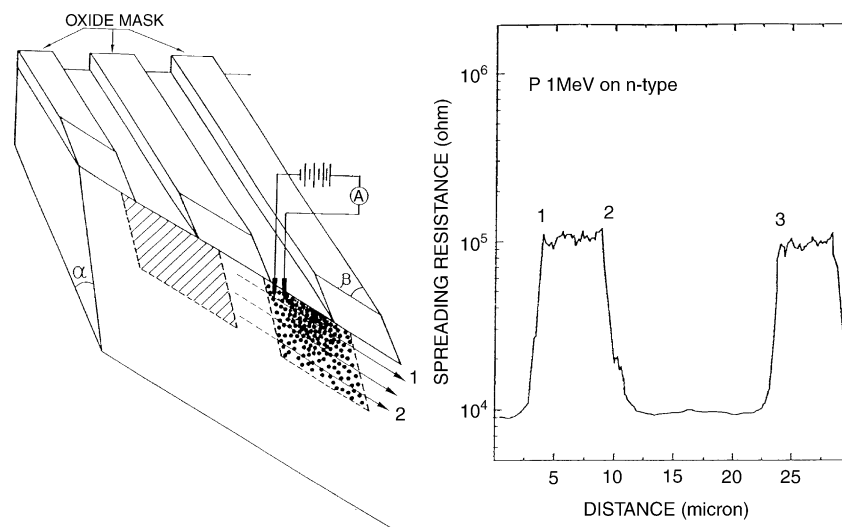


Fig. 66. (Left) Illustration of double-angle bevel on stripe pattern as needed for 2D carrier profiling. (Right) Single scan parallel with bevel edge (single probe).

Next, a special bevel plane (sometimes confusingly called a double bevel) is required as illustrated in Fig. 66. Actually, it is just a normal bevel plane, with a shallow angle  $\alpha$  relative to the original surface (determined by the bevel block used), made such that the bevel edge makes a very shallow ( $30^\circ$ ) angle  $\beta$  with the direction of the doped stripes.

Consequently, as illustrated in Fig. 66, one obtains both an in-depth and a lateral geometrical magnification.

Note, however, that this does *not* automatically imply one can achieve also a useful electrical magnification (improved resolution) in both dimensions simultaneously. This would only be the case if one could use infinitely small (point-like) probes for the measurements. In practice, however, the finite dimensions (circular shape) of the probes make this impossible. This is illustrated in Fig. 67.

On the left side, the one-dimensional profiling case is shown for comparison. As one uses smaller and smaller 1D bevel angles, the circular probe (making abstraction of the micro-contacts) contacts less and less sub-layers simultaneously, and therefore the depth resolution is proportionally improved. This can also be understood by considering the orthogonal projection of the circular contact (along the bevel) onto the cross-sectional plane through the structure. This projection is always an extreme flattened ellipse, whereby the small axis (in the depth direction) controls the depth resolution. When one moves the probe to its next position in a direction orthogonal to the bevel edge, the flattened ellipse projection shifts down in the vertical direction with virtually no overlap with the previous contact projection.

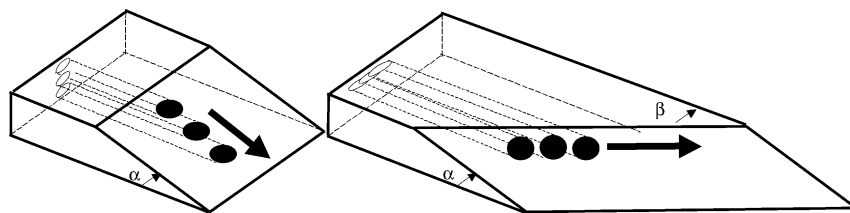


Fig. 67. Illustration of the differences in resolution behavior for (left) the 1D case and (right) the 2D case. The lateral extend of the contact projection on the cross-sectional plane limits the lateral 2D resolution.

Note, however, that the other axis (parallel to the surface) of the ellipse always remains exactly as large as the radius of the original (on bevel) circular contact. For 1D measurements this is irrelevant, as the sub-layers are laterally homogeneously doped, but it is precisely this property of the projected contact, which limits its lateral resolution capabilities when going to 2D measurements as illustrated on the right side of Fig. 67. Because the lateral extension of the projected contact is about 1  $\mu\text{m}$  (as the circular contact itself), even when one uses a very small lateral magnification angle  $\beta$ , one will always contact simultaneously laterally differently doped sub-regions over a distance of 1  $\mu\text{m}$  (although one may be interested in sub-100 nm lateral out-diffusions)! However, when one moves the probe(s) over a distance of also 1  $\mu\text{m}$ , then the projected contact will only move by approximately 0.01  $\mu\text{m}$  in the lateral direction, i.e. as dictated by the magnification angle  $\beta$ . So on a double bevel, in the vertical direction one gets, as expected, a depth resolution proportional with the magnification angle  $\alpha$ , but in the lateral direction, the projected probe maintains its real size and the only gain is that one can now move it over very small lateral distances as controlled by the angle  $\beta$ . Note, therefore, that (for our example) it will require about 100 lateral probe step movements (parallel with the bevel edge) before the projected probe no longer overlaps its original projection (at step 1).

The 2D measurements themselves are done in a different way than in the 1D profiling case. For 2D, the probes are stepped parallel with the bevel edge (at a constant depth) over the region of interest. This is done at different depths until the substrate is reached. Initially two probes were used, but for non-junction-isolated structures also a single probe and a back-contact can be used. Note that for the two-probe case, the probes given their different lateral position, will contact differently doped internal profiles (orthogonal to their position on the bevel). Due to the fact that the different resistances measured by both probes can simply be superimposed, the latter still allows extracting lateral diffusion information. Hence, 2D SRP measurements consist out of a set of lateral resistance profiles recorded at different depths. For two probes, these lateral profiles will either display separate high resistance plateaus (under the mask) separated with low resistance regions (in the doped regions), or overlapping high resistance plateaus separated with low resistance regions dependent on the used probe separation. For single probe measurements, only the former case can occur. The widths of the low resistance regions will be termed  $\Delta\text{Meas}$ .

For a two-probe scan at a given depth, the lateral diffusion at that depth can then be determined through the formula, assuming that all the other parameters can be determined accurately enough through other means:

$$\Delta z = \Delta\text{Meas} + \text{ParSep}/\text{Mag}(\beta) \pm \text{OrthSep} - (P_1 + P_2)/2 \quad (24)$$

where  $\Delta z$  is the nominal width of the stripe plus twice the lateral diffusion, ParSep and OrthSep are, respectively, the separations of the probes in the lateral and orthogonal direction relative to the bevel edge,  $\text{Mag}(\beta) = 1/\sin(\beta)$  is the lateral angle magnification and  $P_1$  and  $P_2$  are, respectively, the lengths of the first and second probe projections in the cross-sectional plane orthogonal to the stripe direction. Note that given the small angles  $\alpha$  and  $\beta$ , the projection of the circular contact is a very flat ellipse with the length of its large axis almost equal to the diameter of the probe contact and almost parallel with the bevel edge.

For a single-probe scan, the lateral diffusion can be determined in a similar way, but with a much simpler formula involving a minimum number of parameters:

$$\Delta z = \Delta\text{Meas} - P_1 \quad (25)$$

Obviously, the accuracy of the final lateral diffusion lengths is critically dependent on the involved parameters in the above two equations. Hence, the single-probe scan is considered to be the most accurate one. In order to determine with a high accuracy the electrical contact size in the scan

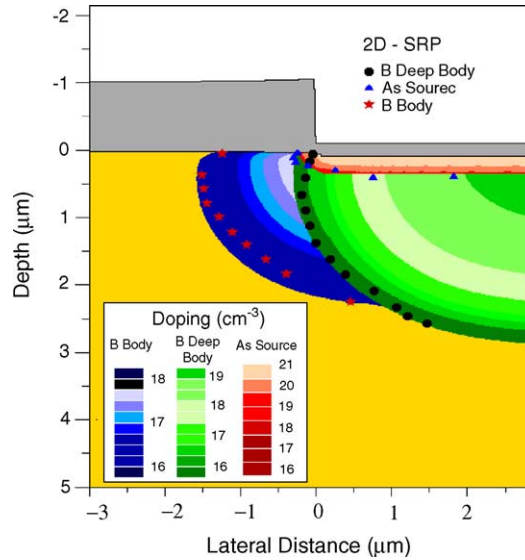


Fig. 68. Illustration of 2D contour lines as they can be extracted from 2D SRP measurements.

direction, a lateral scan on the surface of a calibration stripe pattern can be used as discussed elsewhere.

By combining the lateral diffusion lengths from the scans made at different depths, it is thus possible to create lateral diffusion contour lines. An example of such a contour map is shown in Fig. 68. When interpreting such contour maps, one should keep in mind that also lateral carrier spilling effects may be in effect.

Finally, it is, in principle, also possible to extract the full three-dimensional shape of the dopant profile. This is an iterative procedure where one starts from an initial 3D dopant profile, computes the expected 2D lateral SRP resistance scan, compares it with the experimental data and improves the shape of the dopant profile until convergence is achieved. For the latter, a special simulation program is needed, that assumes that the contact consists of a series of micro-contacts, and for any given position of the probe along the special double-angle bevel, determines for each micro-contact the local in-depth dopant profile below that micro-contact, in the direction orthogonal to the bevel plane. The resistance of the combination of all micro-contacts (each contacting a different internal dopant profile) can then be obtained through the relation:

$$\frac{1}{R_{\text{total}}} = \sum_i \frac{1}{\rho_i \text{CF}(\rho_i, a) / 4r^*} \quad (26)$$

where  $r^*$  is the micro-contact radius and  $a = Nr^*$ , with  $N$  the number of micro-contacts. It should, however, be noted that this is a quite tedious and time-consuming procedure and the success is critically dependent on the knowledge of the precise geometrical distribution of the micro-contacts.

Although originally developed for the characterization of sub-micrometer lateral out-diffusions, it is no longer used as such, given the rapidly growing capabilities of SRRM (and other 2D characterization tools). For larger out-diffusions (such as encountered in power devices), the earlier discussion of the complex projection remains valid, however, here the technique should be regarded as a good solution to increase the lateral resolution. For completeness, it should be noted that this double-angle bevel approach has recently also been used in an attempt to improve the resolution of 2D characterization tools (SCM) [110].

### 5.10. Metal films

Up to now, all applications have been related to silicon. Recently, however, the capabilities of SRP for the characterization of thin metal films (Cu, Al) have been investigated. The need for the latter is related with the need to better understand the physics behind the increase of resistivity of such films as their dimensions (thickness, line width) shrink down. Up to now, typically FPP measurements were performed on as deposited or annealed metal films and in combination with thickness measurements, their thickness dependent resistivity was determined. For very thin films, there is, however, the problem of the percolation nature of the conduction. Using SRP, where one can access information regarding thin films by beveling a thicker one, one can circumvent this.

Given the very low bulk resistivity of metals, for example,  $1.67 \mu\Omega \text{ cm}$  for Cu, it is not possible to apply SRP to thick metal films, as the resistance will be less than the minimum resistance of  $1 \Omega$  that can be measured on most systems. It is, however, possible to do such measurements on very thin (thinner than 70–80 nm) films deposited on an insulator, as the large correction factors due to the presence of the insulating underlying layer (silicon oxide) will bring the measured resistance for Cu film in the 1–100  $\Omega$  range.

More detailed information on this new application area for SRP can be found elsewhere [111,112]. Here, we briefly summarize some of the most important results obtained up to now. Experimentally, one is faced with two problems: (i) it is more difficult to get a sharp bevel edge as Cu is softer than Si; and (ii) reproducibility problems occur as Cu re-oxidizes rather quickly and the oxide becomes thick enough to affect the results.

The raw data profiles on the metal film have a behavior very similar to silicon, and the impact of a pre-bevel resistance increase and a lateral 3D current flow component can readily be observed. The magnitude of the latter seems, however, to be smaller than for silicon. Consequently, it is necessary to correct metal profiles separately for this phenomenon, where this is found not to be necessary for silicon. As such correction is not yet available, it follows that the data for the thinnest films (with the least 3D current flow) are the most reliable ones.

For the extraction of the underlying resistivity profile, the probe–metal contact needs to be calibrated. Given the larger contact size (three times larger, without micro-contacts) and the larger penetration (45 nm) than for silicon, the electrical radius has been determined through AFM topographical measurements. Subsequently, the amount of contact resistance is estimated by subtracting the expected theoretical resistance at the surface from the experimentally measured one. The theoretical surface resistance can be determined from a known value for the sheet resistance of the film as obtained from FPP measurements. Note that, as a consequence of this calibration choice, the sheet resistance based on the extracted SRP resistivity depth profile will automatically lie close to the FPP value, and cannot be considered an independent result.

Finally, given the large penetration involved, it is not obvious that a straightforward application of the Schumann–Gardner correction factor algorithm is appropriate for metal films. Opposite to SG, it may actually be more appropriate to consider the beveled film as being constituted of a series of vertical homogeneous resistivity channels, one for each measurement point. As such, a constant resistivity profile needs to be assumed at each calculation point.

Fig. 69 illustrates some of the resistivity depth profiles, which could be extracted up to now. It is clear that in that case, one needs to establish appropriate calibration curves and extract the contact radii and barrier resistance. Regardless of the uncertainties in calibration and correction procedures, the results do indicate an apparent increase in resistivity of the Cu film with decreasing thickness. The latter is in line with theoretical calculations, which predict a resistivity increase for thinner Cu films, based on the mean free path length of Cu being 39 nm. It should, however, be emphasized that these

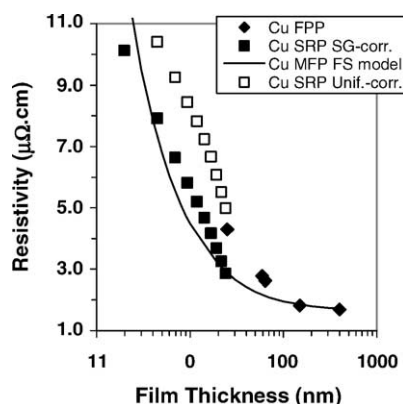


Fig. 69. Resistivity profiles extracted from SRP measurements on a 25 nm Cu film (on a 20 nm Ta/TaN barrier on oxide) with, respectively, the Schumann–Gardner and uniform correction factor model and compared to the MFP model predictions.

are initial results, and much more work is needed in the areas of reproducibility, calibration and contact modeling to obtain reliable quantitative resistivity depth profiles independent from FPP data.

### 5.11. Implantations in germanium

For future deep sub-micrometer CMOS devices, germanium is an important candidate material to replace silicon for many reasons (higher low field mobility, dopant activation at lower temperatures, integration with III/V components, etc.). Consequently, also the application of SRP to Ge-related materials has recently gained more interest [113,114].

In order to be able to quantify germanium measurements correctly, first of all appropriate calibration curves are required as shown in Fig. 70a. For n-type, there is little difference with silicon, except for the smaller germanium slope (0.8). This can probably be attributed to the fact that the conditioning of the probes is not yet optimized for the softer germanium material. For p-type, the germanium calibration curves are much more linear than for silicon, and located significantly lower. The linearity of the germanium calibration curves seems to indicate fewer problems with the Schottky contact between the probes and the material. As a significantly larger contact size on p-type than on

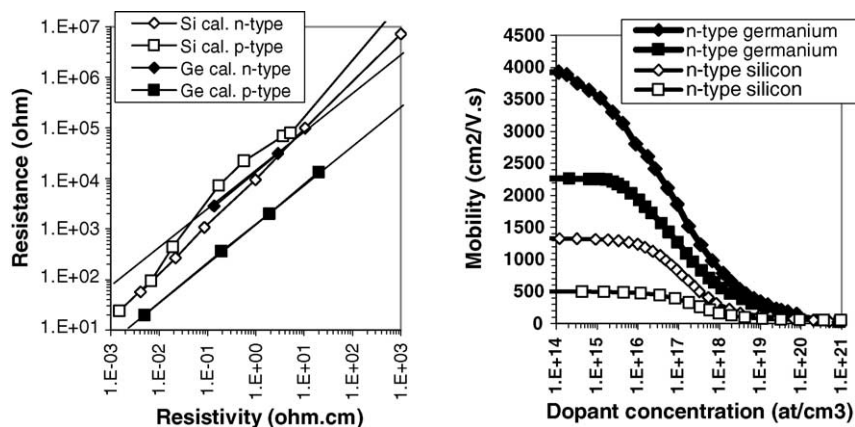


Fig. 70. (a) Comparison of calibration curves for Si and Ge. (b) Comparison of mobility curves for Si and Ge.



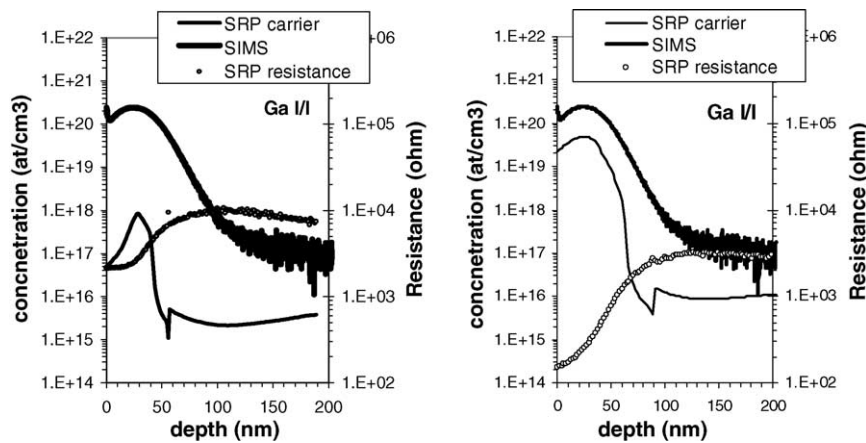


Fig. 71. Illustration of 50 keV Ga (p-type) implant with dose of  $10^{15}/\text{cm}^2$  in n-type Ge substrate: (left) as-implanted; (right) after anneal. Note the almost absent junction cusp on the raw data, opposite to normal silicon operation.

n-type germanium is rather unlikely, the lower level of the p-type curve (relative to n-type) must probably be sought in an electrical surface phenomenon not yet identified. Topographic AFM analysis of the probe imprints of a qualified SRP system indicates an average probe penetration of 15–25 nm, i.e. a factor of two deeper than for silicon.

Second, in order to convert the obtained resistivities towards carrier concentrations, the germanium mobilities as a function of dopant concentrations must be entered in the calculation software. Fig. 70b shows the curves, which were used for the germanium profiles, discussed hereafter.

Fig. 71 shows that SRP on Ge is feasible and illustrates an activation study of junction-isolated Ga I/I profiles for different anneal conditions. The band gap of Ge is smaller, a higher intrinsic carrier level is present and, as such, more rounded and lower resistance junction cusps are observed than for silicon. Eventually, also the impact of surface states on the shape of the junction cusp may not be negligible (as for SSRM in the silicon case). Consequently, it may prove necessary to modify the present deconvolution software for the fact that these junctions under the pressure of the probes may have a more leaky behavior than silicon ones. Notwithstanding the fact that these effects need to be studied in detail, the results in Fig. 71 and the work by Voss et al. [115] indicate that SRP is a valuable tool in the development of a Ge technology.

### 5.12. Summary

As illustrated, SRP can be widely applied to extract useful carrier profile information for all kinds of structures, ranging over depths as deep as tens of nanometers to several micrometers. For the daily interpretation of such profiles one needs, however, the necessary expertise regarding the impact of the carrier spilling phenomenon, as the latter is typically not yet corrected for in routine SRP analysis. And even if a zero-field correction is applied, there will still be discrepancies with fully activated SIMS profiles, as the issues of pressure and surface states also play a role.

For carrier levels above  $10^{18}$  atoms/ $\text{cm}^3$ , the impact of carrier spilling is sufficiently small (for profiles deeper than 100 nm), that correct integrated dose and sheet resistance values can be extracted by SRP. But, as lower concentrations levels or shallower profiles are involved, carrier spilling may also impact the dose and sheet values. Although it can be envisaged that for certain types of structures (such as source/drain implants) in the future, a fully quantitative and automatic carrier

spilling deconvolution may become available, there will always remain certain types of structures (such as the one shown in Fig. 32, left) for which it will never be possible to deconvolute the underlying real dopant profile from SRP raw data.

## 6. Future trends

From the wide range of applications discussed earlier, it is clear that SRP is a versatile and widely applicable tool for electrical depth profiling. On the other hand, some limitations have become apparent over the last decade, and serious questions may be raised towards the future of SRP as a characterization tool [116] for deep sub-micrometer technologies.

### 6.1. Critical assessment of SRP

In order to better understand the fundamental limitations of conventional SRP as it is used today, let us take a closer look at the spreading resistance roadmap as shown in Table 4.

As discussed earlier, the multi-layer Schumann–Gardner correction factor corrects for the dependence of the measured resistance on the shape (steepness) of the underlying dopant profile. Its dependence on the contact radius and tip separation for an abrupt 10 nm junction-isolated epi-layer is illustrated in Figs. 12 and 10. Over the years, the steepness of the dopant profiles has systematically increased at a faster rate than the corresponding decrease in contact radius and separation. Consequently, we will need to apply excessively high SG correction factors of more than a factor of 1000 in

Table 4  
Spreading resistance roadmap

Profile depth	100 $\mu\text{m}$	10 $\mu\text{m}$	1 $\mu\text{m}$	100 nm	10 nm
Year	1965	1975	1985	1995	2005
Load (g)	20–45	10	5	<b>2.5</b>	<b>1</b>
Contact size ( $\mu\text{m}$ )	10–15	7	4	<b>2</b>	<b>1</b>
Probe separation ( $\mu\text{m}$ )	100–500	50	25	<b>10</b>	<b>5</b>
Correction factor	1–2	3	30	<b>300<sup>a</sup></b>	<b>3000<sup>a</sup></b>
Bevel angle	4–5°	1°	16'	3–4'	<1'
Magnification	10	50	250	<i>1000</i>	<b>4000</b>
On bevel step size ( $\mu\text{m}$ )	10	5	2.5	<i>1</i>	<b>0.4</b>
Depth resolution (nm)	1000	100	10	<i>1</i>	<b>0.1</b>
Probe penetration (nm)	1000	100	<i>10</i>	<b>1</b>	<b>0.1</b>
Bevel roughness peak (nm)	1000	100	<i>10</i>	<b>1</b>	<b>0.1</b>
Electrical resolution (nm/decade)	2000	200	20	<b>2</b>	<b>0.2</b>
Calibration curves	REQ	REQ	REQ	REQ	REQ
Multi-layer Laplace		REQ	REQ	REQ	REQ
Radius/barrier calibration			REQ	REQ	REQ
Carrier spilling Poisson			REQ	REQ	REQ
Surface damage correction				REQ	REQ
Micro-contact modeling				REQ	REQ
Sub-30 nm corrections					REQ

Values in bold type exceed the capabilities of conventional SRP. Values in italic type require state-of-the-art SRP operation. Data treatment: REQ = required data correction.

<sup>a</sup> Used parameters: contact size = 4  $\mu\text{m}$ ; tip separation = 25  $\mu\text{m}$ .

the near future. The latter corresponds to a reduced dynamic range of the raw spreading resistance data, which will be as low as one decade for a typical sub-100 nm technology source/drain implant on top of a well structure (involving four dopant decades). Such low dynamic ranges will inevitably make the accurate reconstruction of the original carrier profile extending over five to six decades of magnitude very tedious as noise will be excessively amplified. Ideally, one would like to limit the correction factor to a value of 10.

For the accurate quantification of a shallow 100 nm SRP profile, one needs preferably 50–100 data points, i.e. a geometrical depth resolution of 1–2 nm per point. This requires a state-of-the-art SRP setup with bevel angles as small as a few minutes in combination with 1  $\mu\text{m}$  step sizes. These settings are very close to the attainable limits since such small angles (minutes) are quite difficult to achieve reproducibly and such small step sizes (1  $\mu\text{m}$ ) inevitably result in an unwanted overlap of the probe imprints. Consequently, it is not obvious how the conventional SRP setup can be further extended reliably towards sub-30 nm profiling, which requires a sub-nm depth resolution.

The electrical depth resolution (capability to resolve a given profile steepness) is besides the geometrical resolution, critically dependent on the roughness of the beveled surface and the tip penetration. Today, qualified SRP systems are able to achieve a peak roughness of 10 nm (rms 2 nm) and a tip penetration of 5–10 nm resulting in a 10–20 nm/decade electrical resolution. For future process development, however, resolutions of 2–3 nm/decade will be required. Reducing the bevel roughness further while maintaining a sharp enough bevel edge and/or achieving a lower penetration and, hence, lower weight while maintaining a reproducible contact are virtually impossible to achieve with present SRP equipment.

As discussed earlier, in spreading resistance the data treatment software, which implements the contact models needed for the extraction of the underlying carrier profile, plays an important role. The bottom part of Table 4 lists the main issues involved. The shallower the profiles get, the more elaborate the corrections become. For a sub-100 nm profile, for example, one needs to combine a multi-layer Schumann–Gardner Laplace model with: (a) appropriate radius and barrier resistance calibration procedures; (b) appropriate carrier spilling (diffusion) correction; (c) surface damage correction for junction-isolated structures; and (d) correction for the micro-contacts distribution. For sub-30 nm profiles, an improved insight in existing and the development of new physical models and the calibration of the precise values of the involved physical parameters will be necessary in order to maintain a sufficient quantitative accuracy (e.g. impact of surface charge on the current flow around very small contacts).

The International Technology Roadmap for Semiconductors (ITRS) requires depth profiling of 20–30 nm source extensions by the year 2005. It follows that with respect to these needs, conventional SRP equipment has reached (or even surpassed) its limits with respect to the size of the correction factor, the geometrical and electrical depth resolution, and the complexity of the data correction factor schemes. On the other hand, the basic principle of gaining insight in the local carrier distribution through local resistance measurements remains very attractive, provided it is possible to develop new tools better adapted to the future needs of the semiconductor industry.

## 6.2. Scanning spreading resistance microscopy

SSRM (formerly also referred to as Nano-SRP) was developed jointly by IMEC and the KU Leuven during the period 1991–1994 [117,118]. Recently, this tool has become commercially available [119] illustrating that it takes about 5 years before an envisaged concept can be commercialized. SSRM is an atomic force microscope equipped with a hard, conductive tip [120] (e.g. doped

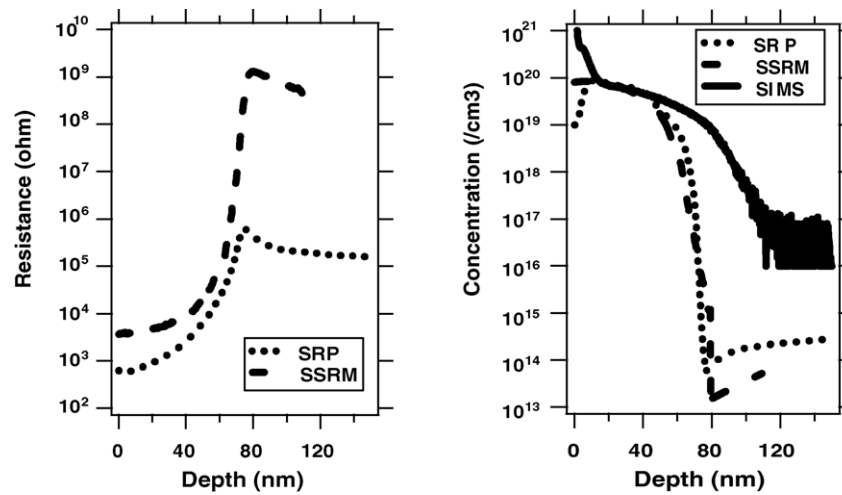


Fig. 72. (Left) SRP and SSRM raw data; (right) SRP and SSRM carrier profile vs. SIMS dopant profile for p-type source/drain implant in n-type substrate.

diamond-coated silicon) in contact with the sample. It probes the local resistivity of the material through a (spreading) resistance measurement between the tip and a large side or back-contact.

Although initially developed for 2D characterization, SSRM can also be applied on 1D-beveled structures (see Fig. 72) [121] (formerly also referred to as Micro-SRP). As such, it represents a breakthrough with respect to two important issues of the spreading resistance roadmap (Table 5). First, for sub-30 nm profiles the correction factors can be reduced substantially from 3000 down to a factor of 70 (Fig. 12), since the SSRM contact size is typically a factor 100 smaller than in conventional SRP (20 nm versus 2  $\mu\text{m}$ ). Second, a geometrical depth resolution of a few Angstrom is easily achievable by combining the small lateral displacements available on an AFM system (1–10 nm) with bevel angles, which are easy to make (i.e.  $16^\circ$ ). Furthermore, typically the diamond based tips can be used out of the box and no longer need any expertise in probe conditioning.

Table 5

Comparison spreading resistance-based tools for 10-nm deep isolated source/drain profile

	SRP	SSRM on bevel (status today)	NanoProfiler <sup>TM</sup> or SSRM on bevel (target values)
Force control ( $\mu\text{N}$ )	<b>50000</b>	50	50
Contact size (nm)	<b>2000</b>	20	20
Probe separation ( $\mu\text{m}$ )	<b>25</b>	<b>5000</b>	0.25 (NanoProfiler <sup>TM</sup> )
Correction factor	<b>3000</b>	70	15
Bevel step size (nm)	<b>1000</b>	1	1
Bevel angle	$<1^\circ$	$16^\circ$	$8^\circ$
Magnification	<b>4000</b>	250	500
Probe penetration (nm)	<b>10</b>	<b>5</b>	0.5
Peak roughness (nm)	<b>10</b>	<b>10</b>	0.5
Probe conditioning	Expertise	Out of box	Out of box
Physical modeling	Needs work	Needs work	Needs work
Probe resistance ( $\Omega$ )	1	<b>200–1000</b>	$<10$

Values in bold type need improvements.

On the other hand, there are still some critical issues that need further work (Table 5). First, a main issue, which is left, is the presence of a back (or side) contact far away (mm range) from the measurement location. This leads inevitably to a large contact separation in the calculation schemes and hence larger than ideal correction factors as discussed before (Section 3.2.1). Furthermore, the bevel roughness and rounding (not yet SSRM fully optimized procedures available) are still of the same magnitude as in SRP. Due to the smaller size of the contact it is to be expected that improved contact models will be necessary to account for local surface charge related effects [80]. Furthermore, the need to use hard enough diamond-based tips (need to withstand 10 GPa pressure and shear stresses during scanning) presently leads to a limitation involving the intrinsic resistance of the tip itself. The intrinsic tip resistance has been reported to vary from more than 1000 down to 200  $\Omega$ , respectively, for diamond-coated silicon and full diamond tips [120,122]. The latter is a serious problem (not present in SRP) since it limits the dynamic range of the technique on highly doped source/drain structures. Ideally the tip resistance should be less than 1  $\Omega$ . Summarizing it follows there is a need for further work on the tip configuration and beveling procedures.

### 6.3. The NanoProfiler<sup>TM</sup>

In order to improve the dynamic range there is a need to lower the intrinsic resistance of the SSRM tips significantly while maintaining a sufficient hardness. Although some further improvement related to doped diamond tips may be feasible, the ultimate solution for low resistivity tips may be metal-based tips provided these can be made hard enough [123,124]. Recent work has shown that it is indeed possible to fabricate (through a batch process) pyramidal Ni-based metal tips, integrated into silicon or metal cantilevers, that are hard enough to display reproducible, Ohmic-like current–voltage characteristics. This breakthrough opens a promising perspective on using metal tips in stepping mode (to minimize shear stresses) for ultra-shallow carrier profiling provided further optimizations can be made with respect to the hardness of the metals applied (e.g. Cr), the shape of the tips (tip-on-tip [123]) and their penetration (less than 1 nm).

A qualified conventional SRP system uses two tips (2–4  $\mu\text{m}$  size) positioned at close separation, typically 25  $\mu\text{m}$ . A perfect AFM-based downscaling of this concept, named the NanoProfiler<sup>TM</sup>, would imply the usage of 20–40 nm size contacts positioned at a separation of 250 nm (Fig. 73). On the other hand, in SSRM the separation between the single tip and the side/back-contact is typically 5–10 mm, i.e. five orders of magnitude larger than the NanoProfiler<sup>TM</sup> concept. Introducing a much smaller separation in the envisaged dual-tip NanoProfiler<sup>TM</sup> concept will significantly improve the results over SSRM on a bevel [116]:

First, there is the pure geometrical effect as characterized by the correction factor. As Fig. 10 illustrates a reduction of the separation from 10 mm down to 250 nm decreases the correction factor significantly by a factor of 4 (from 70 to 15), hence, leading to an improved sensitivity. Second, one must take into account that when measuring on, for example, a 10 nm junction-isolated layer there is

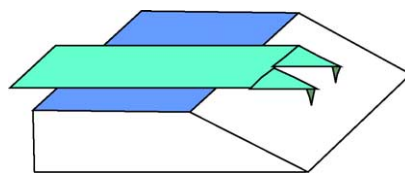


Fig. 73. Principle of the NanoProfiler<sup>TM</sup>: two electrically separated small (20–40 nm contact) tips are positioned at 200–300 nm separation on the same cantilever to be mounted on an SPM system.

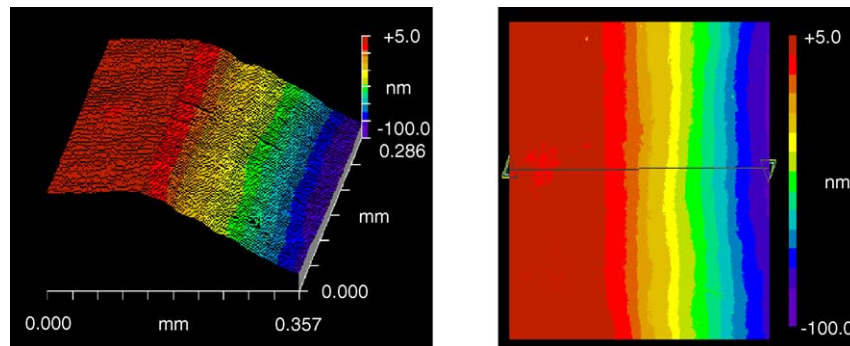


Fig. 74. Etched bevel with an angle of  $1'1''$ , a magnification of a factor of 5000 and an rms roughness of 1.3–1.5 nm [129].

quite a significant lateral current spreading involved as discussed elsewhere [116]. Only reducing the tip separation can minimize this three-dimensional current spreading effect. Third, there is the presence of an additional series resistance when measuring ultra-shallow junction-isolated layers. This originates from a pinch-off effect of the current flowing between the two contacts due to the presence of surface damage (surface states, reduced mobility) induced by the beveling process. This series resistance is roughly proportional to the separation and hence requires a minimization of the latter.

It is clear that the fabrication of these closely spaced but electrically isolated tips on a single cantilever is far from obvious. At present, work is ongoing [125–127] to produce such a structure, based on the techniques for single diamond tips.

Finally, in order to obtain a 2–3 nm/decade electrical depth resolution with spreading resistance-based techniques it is mandatory to reduce the present bevel surface roughness considerably below the present state-of-the-art values of 2 nm rms roughness. The main limitation on using smoother surfaces in conventional SRP has always been the need for a sharp enough bevel edge (starting point determination). Since AFM-based equipment (SSRM and NanoProfilier<sup>TM</sup>) can collect simultaneously detailed topographic and electrical (resistance) information, the bevel edge sharpness is no longer a limiting factor. Hence, a further significant reduction of the bevel roughness (down to 0.5 nm rms), as needed for sub-30 nm depth profiling, can be carried out by replacing the presently used mechanical polishing techniques (0.05  $\mu\text{m}$  high grade diamond paste in oil suspension on a rotating frosted glass plate) by more chemically based approaches (such as colloidal silica, etching). Fig. 74 shows an illustration of an etched bevel with a magnification as large as 5000 and an improved rms roughness of 1.3–1.5 nm [129].

## 7. Conclusion

Since its introduction in 1966, SRP has come a long way. Continued efforts in improving all aspects of the technique (raw data collection, data analysis, etc.) have lead to a reliable and fast technique, which is capable of extracting quantitative carrier concentration depth information on sub-micrometer depth scale with a 1 nm geometrical depth resolution and a 10% accuracy (30% reproducibility), provided a qualified system is being used. The vast area of different applications illustrates the present success of SRP as an important electrical characterization tool.

It should, however, be emphasized that routinely generated SRP carrier profiles are not (or in the best case only partially) corrected for carrier spilling (diffusion) effects, and that the latter phenomenon can make the correct interpretation (junction/interface depth, and eventually dose, sheet) of the



profiles exceedingly difficult. As such, the electrical resolution and precision can be far less than the quoted 1 nm geometrical resolution.

Furthermore, as more and more ultra-shallow (sub-30 nm) profiles need to be characterized, SRP is unfortunately running out of steam, for several other reasons. Primarily, its relatively large radius (micrometer size) and probe separation require extremely large correction factors ( $>5000$ ), and as such form a fundamental limit to the applicability of the technique. Additionally, more and more physical phenomena need to be accounted for in order to still obtain semi-quantitative information. Some of these, such as the surface states distribution along a beveled surface or the permittivity behavior under pressure above 1 GPa, are not yet fully understood or easily tractable.

Nevertheless, the basic principle itself of using spreading resistance related information for the electrical characterization of depth profiles remains as timely as ever. Already today a new tool, named SSRM, based on the usage of an AFM-based system with a single, small (5–10 nm) conductive tip (and a back-contact) is rapidly (within the next 2 years) approaching a level where it will become industrially applicable to replace SRP for one-dimensional, quantitative depth profiling of ultra-shallow (sub-30 nm) junctions (depth resolutions of 1 nm on a cross-section have already been demonstrated).

Further developments towards the usage of two small (5–10 nm) tips in close proximity of each other (200–300 nm separation) are expected to lead within 3–5 years to the ultimate spreading resistance profiling tool for the future, named the NanoProfiler<sup>TM</sup>. As the latter tool will inevitably also suffer from carrier spilling phenomena further research in definitely resolving all aspects related with this phenomenon should be pursued further with the necessary urgency.

## Acknowledgments

P. Eyben (IWT) for supplying the SSRM data, V. Raineri and V. Privitera (CNR-Catania) for supplying some of the SIMS and SRP-2D data. The EEC through projects ESPRIT 519, BCR 3410/1/0/181/91/3 and MAT 940069 have sponsored initial work on SRP.

## References

- [1] R.G. Mazur, D.H. Dickey, *J. Electrochem. Soc.* 113 (1966) 255.
- [2] ASTM Standard No. F672-88: standard test method for measuring resistivity profiles perpendicular to the surface of a silicon wafer using the spreading resistance probe, American Society for Testing and Materials, Philadelphia, 1995.
- [3] W. Vandervorst, T. Clarysse, H.J. Herzog, H. Jorke, M. Pawlik, P. Eichinger, E. Frenzel, M. Baur, Esprit project 519, Dopant profiling for submicron structures, Final report, July 1990.
- [4] W. Vandervorst, T. Clarysse, L. Hellemans, J. Snauwaert, M. Pawlik, BCR project no. 3410/1/0/181/91/3-BCR-B(30), Quantitative measurements of electrical junction depths, lateral outdiffusion lengths and carrier concentrations with sub-micron resolution, Final report, November 1994.
- [5] M. Pawlik, *J. Vac. Sci. Technol. B* 10 (1992) 388.
- [6] T. Clarysse, W. Vandervorst, *J. Vac. Sci. Technol. B* 16 (1998) 260.
- [7] T. Clarysse, W. Vandervorst, *J. Vac. Sci. Technol. B* 18 (2000) 369.
- [8] T. Clarysse, W. Vandervorst, *J. Vac. Sci. Technol. B* 18 (2000) 381.
- [9] J.R. Ehrstein, Spreading resistance measurements—an overview, in: D.C. Gupta, P.H. Langer (Eds.), *Emerging Semiconductor Technology*, ASTM STP 960, American Society for Testing and Materials, 1986.
- [10] J. Albers, Some aspects of spreading resistance profile analysis, in: D.C. Gupta, P.H. Langer (Eds.), *Emerging Semiconductor Technology*, ASTM STP 960, American Society for Testing and Materials, 1986.
- [11] M. Pawlik, M. Grasserbauer, H.W. Werner (Eds.), *Analysis of Microelectronic Materials and Devices* (Section 4.8), Wiley, Chichester, 1991.

- [12] R.G. Mazur, G.A. Gruber, in: M.I. Current, C.B. Yarling (Eds.), *Materials and Process Characterization of Ion Implantation*, Ion Beam Press, Austin, Texas, 1997p. 100.
- [13] H.K. Henisch, *Rectifying Semiconductor Contacts*, Clarendon Press, Oxford, 1957.
- [14] F. Llewellyn Jones, *The Physics of Electrical Contacts*, Oxford University Press, 1957.
- [15] G.A. Lee, in: J.R. Ehrstein (Ed.), *Spreading Resistance Symposium*, Special Publication 400-10, National Bureau of Standards (NBS), 1974, p. 75.
- [16] ASTM Standard No. F723-88: standard practice for conversion between resistivity and dopant density for boron-doped and phosphorus-doped silicon, American Society for Testing and Materials, Philadelphia, 1995.
- [17] D.C. D'Avanzo, R.D. Rung, A. Gat, R.W. Dutton, *J. Electrochem. Soc.* 125 (1978) 1170.
- [18] M. Pawlik, private communication.
- [19] J.R. Ehrstein, Effect of specimen preparation on the calibration and interpretation of spreading resistance measurements, in: *Electrochemical Society Spring Meeting*, 1977, 462–463.
- [20] M. Pawlik, private communication.
- [21] D.C. D'Avanzo, C. Clare, C. Dell'Oca, *J. Electrochem. Soc.* 127 (1980) 2704.
- [22] T. Clarysse, P. De Wolf, H. Bender, W. Vandervorst, *J. Vac. Sci. Technol. B* 14 (1996) 358.
- [23] M. Pawlik, private communication.
- [24] M. Pawlik, A. Casel, H.E. Maes, W. Vandervorst, T. Clarysse, D. Wouters, D. Avau, P. Mertens, Esprit project 519, Second consolidated interim report, IMEC, Leuven, Belgium.
- [25] T. Clarysse, W. Vandervorst, E.J.H. Collart, A.J. Murell, in: B.O. Kolbesen, et al. (Eds.), *Electrochemical Society Proceedings*, vol. 99-16, ALTECH99, 1999, p. 76.
- [26] SSM 150, Program Instruction Manual, Spreading Resistance System, Pittsburgh, USA.
- [27] T. Clarysse, W. Vandervorst, *Solid-State Electron.* 31 (1988) 53.
- [28] Solid State Measurements Inc., Pittsburgh, USA, <http://www.ssm-inc.com/>.
- [29] T. Clarysse, M. Caymax, P. De Wolf, T. Trenkler, W. Vandervorst, J.S. McMurray, J. Kim, C.C. Williams, J.G. Clarck, G. Neubauer, *J. Vac. Sci. Technol. B* 16 (1998) 394.
- [30] P.A. Schumann, E.E. Gardner, *Solid-State Electron.* 12 (1969) 371.
- [31] S.C. Choo, M.S. Leong, K.L. Kuan, *Solid-State Electron.* 19 (1976) 561.
- [32] W.B. Vandervorst, H.E. Maes, *Solid-State Electron.* 24 (1981) 851.
- [33] H.L. Berkowitz, R.A. Lux, *J. Electrochem. Soc.* 128 (1981) 1137.
- [34] S.C. Choo, M.S. Leong, L.S. Tan, *Solid-State Electron.* 24 (1981) 557.
- [35] S.C. Choo, M.S. Leong, J.H. Sim, *Solid-State Electron.* 26 (1983) 723.
- [36] H.L. Berkowitz, *J. Electrochem. Soc.* 137 (1990) 2581.
- [37] T. Clarysse, W. Vandervorst, *J. Vac. Sci. Technol. B* 10 (1992) 432.
- [38] T. Clarysse, W. Vandervorst, *J. Vac. Sci. Technol. B* 18 (2000) 393.
- [39] S.M. Sze, *Physics of Semiconductor Devices*, second ed. Wiley, New York, 1981.
- [40] E.J. Hartford, S.M. Ramey, C.W. Ye, C.L. Hartford, *J. Vac. Sci. Technol. B* 18 (2000) 401.
- [41] J. Albers, H.L. Berkowitz, *J. Electrochem. Soc.* 131 (1984) 392.
- [42] T. Clarysse, W. Vandervorst, *Solid-State Electron.* 33 (1990) 1587.
- [43] T. Clarysse, D. Vanhaeren, W. Vandervorst, *J. Vac. Sci. Technol. B* 20 (2002) 459.
- [44] M. Pawlik, Profiling of ultra-shallow layers using spreading resistance, in: M. Current, M. Kump, G. McGuire (Eds.), in: *Proceedings of the Fourth International Workshop on the Measurement, Characterization and Modeling of Ultra-Shallow Doping Profiles in Semiconductors*, American Vacuum Society, 6–9 April 1997, p. 26.1.
- [45] D.H. Dickey, Developments in ultra-shallow spreading resistance analysis, in: M. Foad, V. Ukraintsev, S. Biesemans (Eds.), in: *Proceedings of Sixth International Workshop on the Measurement Characterization and Modeling of Ultra-Shallow Doping Profiles in Semiconductors*, American Vacuum Society, 22–26 April 2001, p. 176.
- [46] C.M. Osburn, H.L. Berkowitz, J.M. Heddleson, R.J. Hillard, R.G. Mazur, P. Rai-Choudhury, *J. Vac. Sci. Technol. B* 10 (1992) 533.
- [47] D.H. Dickey, *J. Vac. Sci. Technol. B* 20 (2002) 467.
- [48] T. Clarysse, W. Vandervorst, M. Pawlik, *J. Vac. Sci. Technol. B* 14 (1996) 390.
- [49] R.J. Hillard, J.C. Sherbondy, C.L. Hartford, S.R. Weinzierl, R.G. Mazur, *J. Vac. Sci. Technol. B* 16 (1998) 411.
- [50] T. Clarysse, M. Caymax, W. Vandervorst, *Appl. Phys. Lett.* 80 (2002) 2407.
- [51] ISO 5725, Accuracy (trueness and precision) of measurement methods and results, International Organization for Standardization, Geneva, 1994.
- [52] T. Clarysse, D. Vanhaeren, W. Vandervorst, Qualification of SRP operations, Final report, Project no. MAT1-CT 940069, October 1998.

- [53] S.M. Hu, J. Appl. Phys. 53 (1982) 1499.
- [54] H. Jorke, H.-J. Herzog, J. Appl. Phys. 60 (1986) 1735.
- [55] A. Casel, H. Jorke, Appl. Phys. Lett. 50 (1987) 989.
- [56] W. Vandervorst, T. Clarysse, J. Electrochem. Soc. 137 (1990) 679.
- [57] R.G. Mazur, J. Vac. Sci. Technol. B 10 (1992) 397.
- [58] T. Clarysse, W. Vandervorst, A. Casel, Appl. Phys. Lett. 57 (1990) 2856.
- [59] S.R. Weinzierl, R.J. Hillard, J.M. Heddleson, P. Rai-Choudhury, R.G. Mazur, C.M. Osburn, J. Vac. Sci. Technol. B 12 (1994) 322.
- [60] W.A. Keenan, P.A. Schumann, A.H. Tong, R.P. Phillips, A model for the metal–semiconductor contact in the spreading resistance probe, in: B. Schwartz (Ed.), in: Proceedings of Ohmic Contacts to Semiconductors, Electrochemical Society, Electronics Division, 1968, p. 263.
- [61] P.J. Severin, Solid State Electron. 14 (1971) 247.
- [62] P. Kramer, L.J. Van Ruyven, Solid State Electron. 15 (1972) 757.
- [63] J.J. Marchand, T. Van Khiem, J. Appl. Phys. 54 (1983) 7034.
- [64] R.J. Hillard, S.M. Ramey, C. Win Ye, J. Vac. Sci. Technol. B 18 (2000) 389.
- [65] T. Clarysse, W. Vandervorst, J. Vac. Sci. Technol. B 10 (1992) 413.
- [66] K.L. Johnson, Contact Mechanics, Cambridge University Press, Cambridge, 1987.
- [67] P.S. Follansbee, G.B. Sinclair, Int. J. Solids Struct. 20 (1984) 81.
- [68] G.B. Sinclair, P.S. Follansbee, K.L. Johnson, Int. J. Solids Struct. 21 (1985) 865.
- [69] J.Z. Hu, L.D. Merkle, C.S. Menoni, I.L. Spain, Phys. Rev. B 34 (1986) 4679.
- [70] S. Minomura, H.G. Drickamer, J. Phys. Chem. Solids 23 (1962) 451.
- [71] J.S. Williams, et al. J. Mater. Res. 14 (1999) 2338.
- [72] J.E. Bradby, J.S. Williams, J. Wong-Leung, M.V. Swain, P. Munroe, J. Mater. Res. 16 (2001) 1500.
- [73] E.R. Weppelmann, J.S. Field, M.V. Swain, J. Mater. Res. 8 (1993) 830.
- [74] J.E. Bradby, J.S. Williams, J. Wong-Leung, M.V. Swain, P. Munroe, Appl. Phys. Lett. 80 (2002) 2651.
- [75] G.M. Pharr, W.C. Oliver, R.F. Cook, P.D. Kirchner, M.C. Kroll, T.R. Dinger, D.R. Clarke, J. Mater. Res. 7 (1992) 961.
- [76] J.E. Bradby, J.S. Williams, M.V. Swain, Mater. Res. Soc. Symp. Proc. 750 (2003) Y8.24.
- [77] P. Gaworzewski, B. Roos, K. Höppner, W. Höppner, J. Appl. Phys. 79 (1996) 129.
- [78] J. Snauwaert, L. Hellemans, I. Czech, T. Clarysse, W. Vandervorst, M. Pawlik, J. Vac. Sci. Technol. B 12 (1994) 304.
- [79] P. De Wolf, Two-dimensional carrier profiling of semiconductor structures with nanometer resolution, Ph.D. thesis, KU Leuven, Faculty of Applied Science, Electrical Department, Division INSYS, 1998.
- [80] P. Eyben, S. Denis, T. Clarysse, W. Vandervorst, in: Proceedings of the European Materials Research Society (EMRS), Paper reference E-V.2, Strasbourg, 2002.
- [81] S.J. Fonash, NBS Special Publ. 400-10 (1974) 17.
- [82] K. Yamada, M. Nishira, S. Shimada, M. Tanabe, M. Shimazoe, Y. Matsuoka, IEEE Trans. Electron. Devices 29 (1982) 71.
- [83] C.S. Smith, Phys. Rev. 94 (1954) 42.
- [84] Y. Kanda, IEEE Trans. Electron. Devices 29 (1982) 64.
- [85] R.J. Hillard, J.C. Sherbondy, C.L. Hartford, S.R. Weinzierl, R.G. Mazur, J. Vac. Sci. Technol. B 16 (1998) 411.
- [86] T. Clarysse, P. Eyben, N. Duhayon, M.W. Xu, J. Vac. Sci. Technol. B 21 (2003) 729.
- [87] P. Eyben, N. Duhayon, T. Clarysse, W. Vandervorst, J. Vac. Sci. Technol. B 21 (2003) 737.
- [88] M. Xu, Ph.D. thesis, KU Leuven, 2005.
- [89] T. Clarysse, et al., Appl. Phys. Lett., submitted for publication.
- [90] M.S. Leong, S.C. Choo, Y.T. Lee, H.L. Ong, K.P. Ng, J. Vac. Sci. Technol. B 10 (1992) 426.
- [91] T. Clarysse, W. Vandervorst, J. Vac. Sci. Technol. B 12 (1994) 290.
- [92] J. Albers, H.L. Berkowitz, J. Electrochem. Soc. 131 (1984) 392.
- [93] C. Defranoux, S. Bourtaut, J. Venturini, T. Emeraud, M. Hernandez, Infrared spectroscopic ellipsometry applied to the characterization of ultra shallow junction on SOI and silicon, in: NEMatC Conference, Session II, Grenoble, France, March 2004.
- [94] V.N. Faifer, M.I. Current, W. Walecki, V. Souchkov, G. Mikhaylov, P. Van, T. Wong, T. Nguyen, J. Lu, S.H. Lau, A. Koo, Non-contact electrical measurements of sheet resistance and leakage current density for ultra-shallow (and other) junctions, in: Materials Research Society Spring Meeting, Symposium C, San Francisco, 2004.
- [95] J.J. Kopanski, J. Albers, G.P. Carver, J.R. Ehrstein, J. Electrochem. Soc. 137 (1990) 3935.
- [96] D.H. Dickey, J.R. Ehrstein, NBS Special Publ. 400-48 (1979).

- [97] T. Clarysse, F. Dortu, D. Vanhaeren, I. Hofliijk, L. Geenen, T. Janssens, R. Loo, W. Vandervorst, B.J. Pawlak, V. Ouzeaud, C. Defranoux, V.N. Faifer, M.I. Current, Accurate electrical characterization of CMOS ultra-shallow profiles, in: European Materials Research Society Spring Meeting, Symposium B, Strasbourg, France, May 2004.
- [98] Imecprof for W2K, version 3, A professional package for spreading resistance profiling, IMEC, Belgium.
- [99] S.B. Felch, R. Brennan, S.F. Corcoran, G. Webster, Solid State Technol. (1993) 45.
- [100] A. Casel, H. Jorke, M. Pawlik, R. Groves, E. Frenzel, J. Appl. Phys. 67 (1990) 1740.
- [101] Research Training Network IHP-RTN-99-1 (HERCULAS), Contract HPRN-CT-2000-00031.
- [102] B.J. Pawlak, R. Lindsay, R. Surdeanu, B. Dieu, L. Geenen, I. Hofliijk, O. Richard, R. Duffy, T. Clarysse, B. Brijs, W. Vandervorst, C.J.J. Dachs, J. Vac. Sci. Technol. B 22 (2004) 11.
- [103] R. Lindsay, B.J. Pawlak, P. Stolk, K. Maex, Optimisation of junctions formed by solid phase epitaxial regrowth for sub-70 nm CMOS, in: MRS 2002 Proceedings, 2002.
- [104] C.L. Hartford, R.J. Hillard, R.G. Mazur, M.A. Foad, J. Vac. Sci. Technol. B 16 (1998) 316.
- [105] S. Coffa, V. Privitera, F. Priolo, S. Libertino, G. Mannino, J. Appl. Phys. 81 (1997) 1639.
- [106] W. Vandervorst, T. Clarysse, J. Vanhellemont, A. Romano-Rodriguez, J. Vac. Sci. Technol. B 10 (1992) 449.
- [107] V. Privitera, W. Vandervorst, T. Clarysse, J. Electrochem. Soc. 140 (1993) 262.
- [108] W. Vandervorst, V. Privitera, V. Raineri, T. Clarysse, M. Pawlik, J. Vac. Sci. Technol. B 12 (1994) 276.
- [109] W. Vandervorst, T. Clarysse, P. De Wolf, L. Hellemans, J. Snauwaert, V. Privitera, V. Raineri, Nucl. Instrum. Methods Phys. Res. B 96 (1995) 123.
- [110] E. Bussmann, L.J. Klein, C.C. Williams, A study of device amplification for SCM imaging by double-angle beveling, in: P. Ronsheim, J. Kopanski, E. Collart (Eds.), in: Proceedings of the Seventh International Workshop on the Measurement Characterization and Modeling of Ultra-Shallow Doping Profiles in Semiconductors, American Vacuum Society, 27 April–1 May 2003, p. 350.
- [111] T. Clarysse, I. Hofliijk, W. Zhang, K. Maex, W. Vandervorst, J. Vac. Sci. Technol. B22 (2004) 444.
- [112] W. Zhang, S.H. Brongersma, T. Clarysse, W. Wu, I. Vervoort, R. Palmans, I. Hofliijk, H. Bender, W. Hui, L. Carbonell, E. Rosseel, W. vandervorst, K. Maex, Thickness and temperature dependent resistivity of thin copper films, in: Proceedings of the AMC Conference, Montreal, Canada, 21–23 October 2003.
- [113] C.O. Chui, K. Gopalakrishnan, P.B. Griffin, J.D. Plummer, K.C. Saraswat, Appl. Phys. Lett. 83 (2003) 3275.
- [114] Proceedings of the International Electron Devices Meeting (IEDM), 2003.
- [115] S. Voss, N.A. Stolwijk, H. Bracht, J. Appl. Phys. 92 (2002) 4809.
- [116] T. Clarysse, P. Eyben, T. Hantschel, W. Vandervorst, Mater. Sci. Semicond. Proc. 4 (2001) 61.
- [117] P. De Wolf, T. Clarysse, W. Vandervorst, J. Snauwaert, L. Hellemans, J. Vac. Sci. Technol. B 14 (1996) 380.
- [118] P. De Wolf, T. Clarysse, W. Vandervorst, L. Hellemans, Ph. Niedermann, W. Hänni, J. Vac. Sci. Technol. B 16 (1998) 355.
- [119] Veeco Metrology Group, Digital Instruments SPM's, Santa Barbara, CA, USA.
- [120] T. Trenkler, et al. J. Vac. Sci. Technol. B 18 (2000) 418.
- [121] P. De Wolf, T. Clarysse, W. Vandervorst, L. Hellemans, J. Vac. Sci. Technol. B 16 (1998) 401.
- [122] T. Hantschel, P. Niedermann, T. Trenkler, W. Vandervorst, Appl. Phys. Lett. 76 (2000) 1603.
- [123] T. Hantschel, P. De Wolf, T. Trenkler, R. Stephenson, W. Vandervorst, Proc. SPIE 3512 (1998) 92.
- [124] T. Hantschel, T. Trenkler, M. Xu, W. Vandervorst, Proc. SPIE 3875 (1999) 20.
- [125] D. Álvarez, M. Fouchier, J. Kretz, J. Hartwich, S. Schoemann, W. Vandervorst, Fabrication and characterization of full diamond tips for scanning spreading-resistance microscopy, in: 29th International Conference on Micro- and Nano-Engineering, Cambridge, UK, September 2003, Microelectron. Eng. 73–74 2004, 910–915.
- [126] M. Fouchier, P. Eyben, D. Álvarez, N. Duhayon, M. Xu, S. Brongersma, J. Lisoni, W. Vandervorst, Fabrication of conductive atomic force microscope probes and their evaluation for carrier mapping, in: Conference on Smart Sensors, Actuators, and MEMS, Maspalomas, Gran Canaria, Spain, May 2003, Proc. SPIE 5116 2003, 607–616.
- [127] D. Álvarez, J. Hartwich, M. Fouchier, P. Eyben, W. Vandervorst, Appl. Phys. Lett. 82 (2003) 1724.
- [128] National Institute of Standards and Technology (NIST), <http://www.nist.gov/>.
- [129] S. Fearn, Ph.D. thesis, Department of Materials, Imperial College, London, January 2000.